

your title

ACADEMISCH PROEFSCHRIFT

ter verkrijging van de graad van doctor
aan de Universiteit van Amsterdam
op gezag van de Rector Magnificus
prof. dr. K. I. J. Maex

ten overstaan van een door het College voor Promoties ingestelde
commissie, in het openbaar te verdedigen in de Universiteit van
Amsterdam Agnietenkapel
op date,te 11:00 uur

door

Claire Julie Baxter

geboren te Melrose

Promotiecommissie:

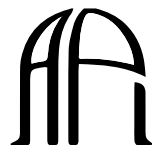
Promotor: prof. dr. Universiteit van Amsterdam

Overige leden:

Faculteit der Natuurwetenschappen, Wiskunde en Informatica



UNIVERSITY OF AMSTERDAM



ANTON PANNEKOEK
INSTITUTE

The research reported in this thesis was carried out at the Anton Pannekoek Institute for Astronomy (API), University of Amsterdam. It was supported by fundings from the National Science Foundation under Grant No. NSF PHY11-25915. The Leids Kerkhoven-Bosscha Fonds (LKBF) provided occasional travel fundings.

quote

S. omeone

CONTENTS

1	Introduction	1
1.1	Section	1
1.1.1	subsection	1
2	Paper 1	3
2.1	Introduction	5
2.2	Observations	7
2.3	Analysis	10
2.3.1	Transit lightcurve analysis	10
2.3.1.1	Extracting Spitzer photometric lightcurves	10
2.3.1.2	Instrumental Systematic Modelling	12
2.3.1.3	Fitting lightcurves to obtain transit parameters	14
2.3.2	Interpreting Transmission Spectrophotometry with 1-D Atmospheric Modeling	16
2.3.2.1	Stellar Irradiation and T-P profiles	16
2.3.2.2	Grid of stellar spectra	19
2.3.2.3	Modeling the photo-chemical kinetics with VULCAN	20
2.3.2.4	Creating the transmission spectra with PLATON	20
2.3.2.5	Calculating the model Spitzer/IRAC transit depths	20
2.4	Results	23
2.4.1	Measured transit depths and their ratios	23
2.4.1.1	Results of measured transit depths	23
2.4.1.2	Comparison to literature	26
2.4.1.3	Transit depth ratio	26
2.4.1.4	Searching for trends in the difference of transit depths	27
2.4.1.5	Transit depth versus equilibrium temperature	28
2.4.2	Results from the 1-D grid of model transmission spectra	28
2.4.2.1	General trends observed in the grids of models	28
2.4.2.2	Statistical comparison of planet atmospheres with model grid	32
2.5	Discussion	34
2.5.1	Expected opacities at 3.6 and 4.5 μm	34
2.5.2	Discussion on Transit Survey	36

2.5.2.1	Comparing transit depths to fiducial model grid	36
2.5.2.2	Effect of metallicity in hot Jupiter atmospheric spectra	37
2.5.2.3	Vertical mixing and non-equilibrium effects	38
2.5.2.4	Effects of clouds on the cool and hot Jupiter atmospheric spectra	39
2.5.2.5	Outliers and the effect of nightsides	40
2.5.2.6	Radius Anomaly	41
2.5.2.7	Stellar Variability	41
2.5.3	Comparing Transmission and Emission with warm Spitzer/IRAC	42
2.5.3.1	Probing different pressures with emission and transmission	42
2.5.3.2	Comparing to brown dwarfs with a Color-Magnitude diagram	44
2.6	Conclusion	46
Appendix 2.A	Pipeline results Figures and Tables	47
Appendix 2.B	VULCAN validation on HD 209458b	66
Appendix 2.C	Radius Anomaly	66
3	Paper 2	75
3.1	Introduction	76
3.2	Observations	77
3.3	Data analysis	78
3.3.1	Calculating the planetary brightness temperatures	78
3.3.2	Extracting the planetary flux deviation from a blackbody	79
3.3.3	Irradiation, equilibrium, effective, and max dayside temperatures definitions	79
3.3.4	Grid of forward emission models to interpret observations	80
3.4	Results	81
3.4.1	Deviation between equilibrium and brightness temperatures	81
3.4.2	Increasing trend in brightness temperature ratio versus equilibrium temperature	84
3.4.3	Increasing trend in planetary deviation from a blackbody	85
3.5	Discussion	86
3.5.1	Summary of our main results	86
3.5.2	Expected opacities at $3.6\ \mu\text{m}$ and $4.5\ \mu\text{m}$	86
3.5.3	Grid of forward models	87
3.5.4	Interpretation of the transition from hot Jupiters to ultra-hot Jupiters	88
3.5.4.1	Assumptions on albedo, redistribution, clouds, and thermal structure	88
3.5.4.2	Transition in thermal inversions	90
3.6	Clues from HST/WFC3	91
3.7	Conclusions	94
Appendix 3.A	Details of the data analysis	95

3.A.1	Fitting correlations with x and y errors	95
Appendix 3.B	Importance of using stellar models	96
3.B.1	Effect of different stellar models on measured temperature	96
Appendix 3.C	Comparing effective temperatures with Schwartz & Cowan (2015)	97
Appendix 3.D	KELT-9b Eclipse: the hottest of the UHJs	98
4	Paper 2	105
4.1	Introduction	106
4.2	Observations	107
4.3	Data Analysis	107
4.3.1	Spitzer/IRAC photometric lightcurve reduction	107
4.3.2	Spitzer/IRAC secondary eclipse fitting	108
4.4	Results	109
4.4.1	Spitzer/IRAC secondary eclipse lightcurves	109
4.4.2	Brightness variability of WASP-18b in time	112
4.4.3	Testing the method to measure variability	112
4.4.4	Variability of WASP-18b at various wavelengths	115
4.5	Discussion & Conclusion	115
Appendix 4.A	Supplementary plots	117
	Bibliography	121
	Contribution from co-authors	129
	Other publications	131
	Nederlandse Samenvatting	133
	Acknowledgements	135

1

INTRODUCTION

1.1 Section

1.1.1 subsection

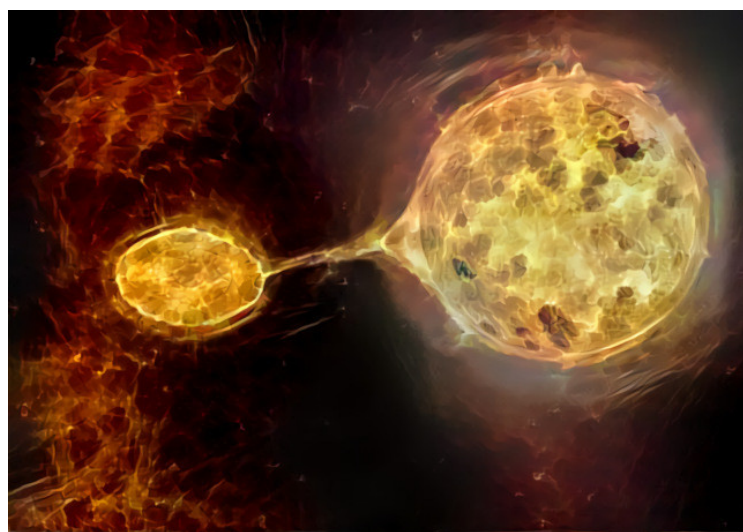


Fig. 1.1: A figure

EVIDENCE FOR DISEQUILIBRIUM CHEMISTRY FROM VERTICAL MIXING IN HOT JUPITER ATMOSPHERES: A COMPREHENSIVE SURVEY OF TRANSITING CLOSE-IN GAS GIANT EXOPLANETS WITH WARM-SPITZER/IRAC



Claire Baxter, Jean-Michel Désert, Shang-Min Tsai, Kamen O. Todorov, Jacob L. Bean, Drake Deming, Vivien Parmentier, Jonathan J. Fortney, Michael Line, Daniel Thorngren, Raymond T. Pierrehumbert, Adam Burrows, Adam P. Showman

Astronomy & Astrophysics, 2000, 001, 01

Abstract

Aims We present a large atmospheric study of 49 gas giant exoplanets using infra-red transmission photometry with Spitzer/IRAC at 3.6 and 4.5 μm .

Methods We uniformly analyse 70 photometric lightcurves of 33 transiting planets using our custom pipeline, which implements pixel level decorrelation. Augmenting our sample with 16 previously published exoplanets leads to a total of 49. We use this survey to understand how infra-red photometry traces changes in atmospheric chemical properties as a function of planetary temperature. We compare our measurements to a grid of 1-D radiative-convective equilibrium forward atmospheric models which include disequilibrium chemistry. We explore various strengths of vertical mixing ($K_{zz} = 0 - 10^{12}$) as well as two chemical compositions (1x and 30x solar).

Results We find that on average, Spitzer probes a difference of 0.5 atmospheric scale heights between 3.6 and 4.5 μm , which is measured at 7.5σ level of significance. Changes in the opacities in the two Spitzer bandpasses are expected with increasing temperature due to the transition from methane dominated to carbon monoxide dominated atmospheres at chemical equilibrium. Comparing the data with our model grids, we find that the coolest planets show a lack of methane compared to expectations, which has also been reported by previous studies of individual objects. We show that the sample of coolest planets rule out 1x solar composition with $>3\sigma$ confidence while supporting low vertical mixing ($K_{zz} = 10^8$). On the other hand, we find that the hot planets are best explained by 1x solar metallicity and high vertical mixing models ($K_{zz} = 10^{12}$). We interpret this as the lofting of CH₄ to the upper atmospheric layers. Changing the interior temperature changes the expectation for equilibrium chemistry in deep layers, hence the expectation from disequilibrium chemistry higher up. We also find a significant scatter in the transmission signatures of the mid-temperate and ultra-hot planets, likely due to increased atmospheric diversity, without the need to invoke higher metallicities. Additionally, we compare Spitzer transmission with emission in

the same bandpasses for the same planets and find no evidence for any correlation. Although more advanced modelling would test our conclusions further, our simple generic model grid points towards different amounts of vertical mixing occurring across the temperature range of hot Jupiters. This finding also agrees with the observed scatter with increasing planetary magnitude seen in Spitzer/IRAC color-magnitude diagrams for planets and brown dwarfs.

2.1 Introduction

Studying exoplanets is critical for gaining insights into the dominant composition and physical atmospheric processes and for understanding the theory of planet formation and evolution (Seager & Deming 2010; Crossfield 2015; Deming & Seager 2017). Hot Jupiters with large scale heights are ideal targets for detecting molecular signatures in their atmospheres via transmission spectroscopy (Seager & Sasselov 2000; Brown 2001). The atmospheres of such planets have been studied across a large range of wavelengths with a myriad of different instruments. Given the number of exoplanet atmospheres already observed, we now enter the era of statistical study of exoplanet atmospheres (e.g., Beatty et al. 2014; Gao et al. 2020; Keating et al. 2019; Garhart et al. 2020; Baxter et al. 2020; Fu et al. 2017; Tsiaras et al. 2018; Wallack et al. 2019).

Wavelength dependent transit depths are in principle primarily sensitive to the atmospheric composition (Seager & Sasselov 2000), in practice these observations have often been plagued by the presence of clouds/hazes dampening the expected molecular signals (e.g., Fortney 2005; Sing et al. 2016; Barstow et al. 2017). Nevertheless, Cloud-free hot Jupiter atmospheres in chemical equilibrium are predicted to exhibit traces of water, carbon monoxide and methane (Seager & Sasselov 2000; Fortney 2005; Fortney et al. 2010). Studies are conducted to demonstrate whether such elements are statistically and systematically observed in exoplanets (Tsai et al. 2018). However, non-equilibrium chemistry and clouds are predicted to be present in close-in giant exoplanet atmospheres, and will impact their observations (e.g., Agúndez et al. 2012; Drummond et al. 2016; Steinrueck et al. 2019). Sing et al. (2016) performed a mini-survey of the transmission spectra of ten hot Jupiters. They characterize them in terms of a cloud index and find a transition between cloudy and cloud-free atmospheres. They note that a temperature-pressure profile crossing a condensation curve is not solely responsible for the resulting damped spectra, rather it is likely that non-equilibrium effects such as atmospheric circulation and vertical mixing play a role.

There are several important atmospheric processes to consider that can drive atmospheres away from cloud-free chemical equilibrium. ? showed that atmospheric transport can move atmospheric abundances away from chemical equilibrium and greatly alter the expected spectroscopic observations. They develop a 1D framework to capture these complex atmospheric processes and parameterize it with an eddy diffusion co-efficient (K_{zz}). For hot Jupiters, K_{zz} ranges from 10^8 to 10^{12} , based on the estimation of the mean vertical wind in global circulation models (GCM) (Moses et al. 2011; Parmentier et al. 2013). Additionally, Komacek et al. (2019) estimated that the strength of vertical mixing will increase for hotter planets. Particularly relevant to this work is the recent advances made in the field of brown dwarf atmospheres: Miles et al. (2020) study the strength of vertical mixing in cool brown dwarf atmospheres with temperatures 250–750 K, and find that the cooler objects support mixing close to the theoretical maximum yet the warmer objects show weaker than predicted mixing.

Additionally, the atmospheres of warm giant close-in exoplanets seem to be deficient in methane. According to equilibrium chemistry, methane is predicted to be abundant in the

atmospheres of exoplanets with equilibrium temperatures cooler than 1100 K (Madhusudhan 2012). In this context, (Stevenson et al. 2010) showed that the atmosphere of GJ436b is substantially methane deficient relative to chemical equilibrium models, suggesting the presence of non-equilibrium processes such as those induced by vertical mixing, which has been tested by follow-up studies (Knutson et al. 2011; Lanotte et al. 2014). Several other studies have attempted to model the methane depletion of GJ 436b: using non-equilibrium photochemical models (Line et al. 2011), high metallicity (230-1000x solar) models (Moses et al. 2013), models with hydrogen depletion (Hu et al. 2015), and invoking tidal heating due to high eccentricity (Agúndez et al. 2014). Morley et al. (2017) provide new data along with a reanalysis and new modeling, they confirm the methane depletion and find the best fitting models have high metallicity, disequilibrium chemistry and tidal heating resulting in an intrinsic temperature (T_{int}) of 300-350 K. T_{int} characterizes the heat flux escaping from the planetary interior, which is written as σT_{int}^4 . Recently, Fortney et al. (2020) suggested that the ongoing eccentricity damping of three warm Neptunes, including GJ 436b, heats their atmospheres and drives strong convective mixing resulting in a decreased CH₄/CO ratio.

Furthermore, methane depletion has been observed in a slew of other warm giant planets. HST/WFC3 observations of the transmission spectra of both WASP-107b and WASP-117 b reveal no detection of methane expected from chemical equilibrium, only upper limits, suggesting a methane depletion in these atmospheres (Kreidberg et al. 2018b; Spake et al. 2018; ?). Additionally, combined HST/WFC3 and Spitzer/IRAC transmission spectra observations of GJ3470 b (Benneke et al. 2019), HAT-P-11 b (Chachan et al. 2019), HAT-P-26 b (Wakeford et al. 2017) and WASP-39 b (Wakeford et al. 2018) all have lower than expected abundances of methane given their temperatures. All in all, methane has only been sparsely detected in the atmospheres of a few exoplanets (Swain et al. 2008; Tinetti et al. 2010; Guilluy et al. 2019).

In this paper, we aim to statistically characterize a large sample of hot Jupiters using the two remaining active detectors on Spitzer/IRAC at 3.6 μm . and 4.5 μm . (Fazio et al. 2004; Werner et al. 2004). At these two wavelengths we expect to see the absorption of methane (CH₄) and carbon monoxide or carbon dioxide (CO or CO₂) respectively. We uniformly analyze Spitzer/IRAC photometric transit lightcurves of a survey of 34 gas giant planets. This survey represents the largest analysis of Spitzer/IRAC observations of gas giants in transmission to date, and it spans equilibrium temperatures from 500 K to 2700 K.

This paper is organized as follows: In Section 2.2 we describe the observations and the survey of planets. In Section 2.3 we describe the data reduction, photometric extraction, lightcurve fitting, and the creation of our grid of 1-D atmospheric models. Section 2.4 describes the results for the transit survey and the statistical survey comparison to the grid of models. In Section 2.5 we discuss the context and implications for the different trends and statistics that we observe. Additionally, in Section 2.5 we describe the collection and combination of the secondary eclipse data with GAIA distances and discuss and comparison between transits and eclipses.

2.2 Observations

As part of the survey programs 90092 (PI Desert) and 13044 (PI Deming) we present the transit depth analysis 70 transit lightcurves of 33 planets in the Post Cryogenic Warm *Spitzer*/IRAC bandpasses of $3.6\text{ }\mu\text{m}$ and $4.5\text{ }\mu\text{m}$. With the goal of gaining a stronger understanding of the origins and nature of the exoplanets already discovered, we designed the survey to probe a wide range of masses, radii and equilibrium temperatures: ranging from cooler long-period gas giants ($\sim 200\text{K}$) from the *Kepler* mission to close-in hot Jupiters (up to 2300 K). Table 2.1 presents the observational information for the 33 planets in the survey. These exoplanets were selected due to their high expected signal-to-noise ratio and, in the case of the Kepler planets, their multiplicity. Additionally, we augment this sample with two extra planets to probe the coolest and the hottest regions of parameter space, these are WASP-121b from program 13044 (PI Deming) and WASP-107b from program 13052 (PI Werner). A full list of the observations is displayed in Table 2.1.

All observations from our survey were taken in "peak-up" mode. Meaning the main observation was preceded by a 30 minute peak-up observation allowing for accurate pointing and thus obtaining precise positioning of the target to within 0.1 pixels throughout the observations. This significantly reduces the ramp effect caused by the intrapixel sensitivity (discussed in Section 2.3.1.2).

We expand our survey to other transiting planets for which the transit depths in the Spitzer bandpasses are taken from the literature. First, we perform a search on exoplanets.org (Wright et al. 2011) which yielded $3.6\text{ }\mu\text{m}$ and $4.5\text{ }\mu\text{m}$ transits for 16 additional planets. Combining these with our survey allows us to gain insights into the current state of infrared exoplanet transmission spectra in a statistical manner. These additional planets and their transit depths are listed in Table 2.2. Figure 2.1 presents a visualization of the parameter space covered by all planets in our survey (analyzed and literature).

WASP-6b and WASP-34b are part of the original survey program 90092, however, we exclude them from our analysis because the transits were missed. In the case of WASP-6b, the predicted mid-transit times had a large degree of uncertainty on the ephemeris, and the observed transits in both channels did not have sufficient baseline to gain accurate constraints on the atmosphere. In the case of WASP-34b, both transits were missed due to an error in the ephemeris.

Table 2.1: Details of the Spitzer Observations used in our survey analysis showing the UT date of observation, the duration of observation in hours, and the program ID of each transit.

Target	λ $\mu\text{ m}$	UT Start Date	Duration	Program ID
			Hours	
GJ3470 b	4.5	2013 Jan 01	4.4	90092
GJ3470 b	3.6	2012 Dec 22	4.4	90092
HAT-P-12 b	4.5	2013 Mar 11	4.5	90092
HAT-P-12 b	3.6	2013 Mar 08	4.5	90092

Table 2.1: continued.

Target	λ μ m	UT Start Date	Duration Hours	Program ID
HAT-P-18 b	3.6	2013 Jun 17	5.0	90092
HAT-P-18 b	4.5	2013 Jul 09	5.0	90092
HAT-P-1 b	4.5	2013 Sep 20	5.2	90092
HAT-P-1 b	3.6	2013 Sep 11	5.2	90092
HAT-P-26 b	3.6	2013 Sep 09	4.5	90092
HAT-P-26 b	4.5	2013 Apr 23	4.5	90092
HAT-P-32 b	3.6	2012 Nov 18	5.4	90092
HAT-P-32 b	4.5	2013 Mar 18	5.4	90092
HAT-P-41 b	3.6	2017 Jan 18	12.1	13044
HAT-P-41 b	4.5	2017 Feb 03	12.1	13044
HATS-7 b	4.5	2016 Nov 04	5.2	13044
HATS-7 b	3.6	2016 Nov 01	5.2	13044
KELT-7 b	4.5	2017 Jan 04	10.3	13044
KELT-7 b	3.6	2016 Dec 27	10.3	13044
Kepler-45 b	4.5	2013 Sep 29	4.5	90092
Kepler-45 b	3.6	2013 Sep 22	4.5	90092
Kepler-45 b	4.5	2013 Sep 12	4.5	90092
Kepler-45 b	3.6	2013 Sep 07	4.5	90092
Kepler-45 b	3.6	2013 Oct 16	4.5	90092
Kepler-45 b	4.5	2013 Nov 15	4.5	90092
Kepler-45 b	4.5	2013 Aug 21	4.5	90092
Kepler-45 b	3.6	2013 Aug 06	4.5	90092
TrES-2 b	4.5	2012 Nov 26	4.3	90092
TrES-2 b	3.6	2012 Nov 21	4.3	90092
WASP-101 b	4.5	2017 Jan 17	8.0	13044
WASP-101 b	3.6	2017 Jan 06	8.0	13044
WASP-107 b	3.6	2017 May 02	8.7	13052
WASP-107 b	4.5	2017 Apr 26	8.7	13052
WASP-121 b	4.5	2017 Jun 05	8.5	13044
WASP-121 b	3.6	2017 Jun 02	8.5	13044
WASP-131 b	4.5	2017 Jun 04	11.3	13044
WASP-131 b	3.6	2016 Nov 04	11.3	13044
WASP-13 b	3.6	2013 Jul 07	7.5	90092
WASP-13 b	4.5	2013 Jan 22	7.5	90092
WASP-17 b	4.5	2013 May 14	8.2	90092
WASP-17 b	3.6	2013 May 10	8.2	90092
WASP-1 b	4.5	2013 Mar 20	6.8	90092

Table 2.1: continued.

Target	λ $\mu\text{ m}$	UT Start Date	Duration Hours	Program ID
WASP-1 b	3.6	2013 Mar 10	6.8	90092
WASP-21 b	4.5	2013 Sep 01	6.1	90092
WASP-21 b	3.6	2013 Aug 27	6.1	90092
WASP-29 b	4.5	2017 Mar 14	7.8	13044
WASP-29 b	3.6	2017 Feb 22	7.8	13044
WASP-31 b	4.5	2013 Mar 19	4.6	90092
WASP-31 b	3.6	2013 Mar 09	4.6	90092
WASP-34 b	4.5	2013 Mar 25	4.5	90092
WASP-34 b	3.6	2013 Mar 17	4.5	90092
WASP-36 b	3.6	2017 Feb 20	7.3	13044
WASP-36 b	4.5	2017 Aug 10	7.3	13044
WASP-39 b	4.5	2013 Oct 10	5.0	90092
WASP-39 b	3.6	2013 Apr 18	5.0	90092
WASP-4 b	4.5	2012 Dec 31	4.3	90092
WASP-4 b	3.6	2012 Dec 27	4.3	90092
WASP-62 b	3.6	2016 Nov 24	11.3	13044
WASP-62 b	4.5	2016 Dec 07	11.3	13044
WASP-63 b	4.5	2017 Jun 17	15.8	13044
WASP-63 b	3.6	2017 Apr 21	15.8	13044
WASP-67 b	3.6	2017 Jan 22	5.6	13044
WASP-67 b	4.5	2017 Aug 13	5.6	13044
WASP-69 b	4.5	2017 Aug 30	6.5	13044
WASP-69 b	3.6	2017 Aug 26	6.5	13044
WASP-6 b	3.6	2013 Jan 21	4.6	90092
WASP-6 b	4.5	2013 Jan 14	4.6	90092
WASP-74 b	4.5	2017 Jan 16	6.7	13044
WASP-74 b	3.6	2017 Jan 14	6.7	13044
WASP-79 b	4.5	2016 Nov 27	11.1	13044
WASP-79 b	3.6	2016 Nov 20	11.1	13044
WASP-94 Ab	3.6	2017 Feb 10	13.3	13044
WASP-94 Ab	4.5	2017 Aug 06	13.3	13044
XO-1 b	4.5	2013 May 25	5.4	90092
XO-1 b	3.6	2013 May 13	5.4	90092
XO-2 b	3.6	2013 Jan 02	4.9	90092
XO-2 b	4.5	2012 Dec 31	4.9	90092

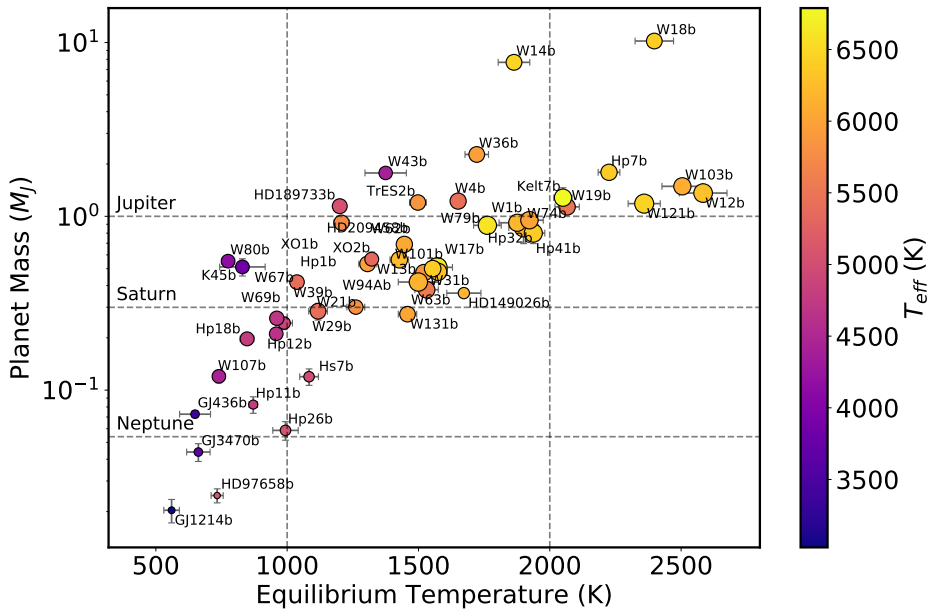


Fig. 2.1: Planet mass (M_{Jup}) versus equilibrium temperature in Kelvin (assuming zero albedo and full redistribution) for all the planets presented in the current survey. The color of the points shows the stellar temperature (T_{eff}) in Kelvin and the size of the points is scaled proportionately to the planetary radius. The gray dashed horizontal lines mark the masses of Jupiter, Saturn and Neptune. The gray dashed vertical lines mark the temperature regions discussed in Section 2.4.1.5.

2.3 Analysis

2.3.1 Transit lightcurve analysis

2.3.1.1 Extracting Spitzer photometric lightcurves

We designed a custom pipeline to produce a photometric lightcurve from the Basic Calibrated Data frames produced by the Spitzer level 1 pipeline. As is standard for these data, our pipeline corrects dark current, flat fields, corrects for pixel non-linearity, and converts to flux units.

We first calculate the mid-exposure timing of each data point in our transit lightcurves using the UTC-based MJD values from the headers of each fits file. Our custom pipeline then corrects transient bad pixels in the image timeseries by comparing each pixel intensity to a median of the 30 preceding and 30 following frames. We replace the pixel intensity with the median value if it is $\geq 4\sigma$ from this value. The fraction of transient bad pixels that are corrected is displayed in Table 2.10, this varies around 0.5% and 0.06% for channel 1 and channel 2, respectively. Our pipeline also consists of several different functions for three

Table 2.2: Spitzer measurements at $3.6\ \mu\text{m}$ and $4.5\ \mu\text{m}$ for planets that have already been published. We include these measurements to our survey.

Planet	T_{eq} (K)	$\delta_{3.6}$ (%)	$\delta_{4.5}$ (%)	Reference
GJ 1214 b	560 ± 30	1.354 ± 0.009	1.367 ± 0.004	1
GJ 436 b	649 ± 59	0.695 ± 0.011	0.705 ± 0.012	2, 16
HAT-P-11 b	871 ± 16	0.338 ± 0.002	0.336 ± 0.003	3
HAT-P-7 b	2225 ± 41	0.629 ± 0.024	0.604 ± 0.012	4
HD 149026 b	1673 ± 65	0.269 ± 0.004	0.253 ± 0.004	5
HD 189733 b	1200 ± 22	2.405 ± 0.008	2.416 ± 0.011	6
HD 209458 b	1446 ± 19	1.481 ± 0.012	1.466 ± 0.007	7
WASP-103 b	2505 ± 78	1.401 ± 0.033	1.433 ± 0.026	8
WASP-12 b	2584 ± 91	1.341 ± 0.02	1.306 ± 0.031	9
WASP-14 b	1864 ± 60	0.887 ± 0.013	0.888 ± 0.013	10
WASP-18 b	2398 ± 73	0.959 ± 0.057	0.972 ± 0.049	11
WASP-19 b	2066 ± 46	1.957 ± 0.05	2.036 ± 0.051	4
WASP-33 b	2694 ± 53	1.166 ± 0.022	1.061 ± 0.023	5
WASP-43 b	1375 ± 79	2.496 ± 0.009	2.525 ± 0.016	12
WASP-80 b	775 ± 25	2.937 ± 0.013	2.969 ± 0.014	13
K2-25b	482 ± 20	1.143 ± 0.16	1.158 ± 0.18	14
HD97658b	733 ± 23	074 ± 002	08 ± 002	15
HAT-P-2 b	1540 ± 30	0.465 ± 01	0.496 ± 008	17

(1) Fraine et al. (2013); (2) Knutson et al. (2011); (3) Chachan et al. (2019); (4) Wong et al. (2016); (5) ?; (6) Pont et al. (2013); (7) Sing et al. (2016); (8) Kreidberg et al. (2018a); (9) Stevenson et al. (2014c); (10) Wong et al. (2015); (11) Maxted et al. (2013); (12) ?; (13) Triaud et al. (2015); (14) Thao et al. (2020); (15) Guo et al. (2020); (16) Morley et al. (2017); (17) Lewis et al. (2013);

important steps in the data reduction: background sky subtraction, finding the centroid of the object, and performing aperture photometry. Additionally, in between these steps, a sliding σ -clipping on any outliers is performed on the centroiding and on the resulting photometry.

Previous studies have demonstrated that the data reduction method chosen to produce the lightcurves can have significant effects on the resulting measured transit depths (Ingalls et al. 2016). We thus optimized the background subtraction, centroiding and aperture photometry methods by running the pipeline over a 3 dimensional grid of different methods for each step, we call these methods the pipeline parameters. We tested three methods of background subtraction:

1. The "Box" method: Median value from a 2×2 or 4×4 pixel box in all four corners of the frame.
2. The "Annulus" method: The mean of an annulus centred on the star of radii 6 or 8

pixels and size 2 or 4 pixels (using photutils).

3. The "Histogram" method: Fit a Gaussian to a histogram of all the pixels in the frame, excluding the star.

We also tested three methods of centroiding:

1. The "Barycenter" method: Center of light of a 3x3, 5x5 or 7x7 pixel box centered on the approximate position of the star.
2. The "Gaussian" method: Fit a two dimensional Gaussian function to the entire image using Astropy (Astropy Collaboration et al. 2018). All of the parameters of the 2D Gaussian were let free ($A, x_0, y_0, \sigma_x, \sigma_y, \theta$) for each frame. The centroid position was the x_0, y_0 from the Levenberg Marquardt Least Squares fit. (Agol et al. 2010)
3. The "Moffat" method: Same as above but instead a 2D Moffat function was fit to the entire image.

Finally, we varied the aperture radius from 2.5 to 5.0 pixels in increments of 0.25 pixels.

For each instance of the grid and thus each iteration of the data reduction pipeline, we performed a least-squares fit to our model (transit + systematic) and calculated the reduced χ^2 . The parameters yielding the lowest reduced χ^2 were used to create the lightcurve used for further analysis. There are a few exceptions to this, for example, some of the cooler planets have a lower signal-to-noise ratio (SNR) meaning the systematics dominate and there is thus a larger scatter in the measured parameters at each pipeline iteration. These planets were examined manually and pipeline parameters were chosen by hand looking for both repeatable measurements and close to the minimum reduced χ^2 . The optimum pipeline parameters including centroiding method, aperture size, background subtraction method and data reduction information for each planet are detailed in Table 2.9. Although the observations were made in "peak-up" mode, it is common that there is still some persistence at the beginning of the lightcurves. To correct for this, we devised a similar χ^2 test for cutting out the ramp at the beginning of the observations. We performed a series of cuts at the beginning of the lightcurve and refitted the model. Similarly, we chose the time to trim off the beginning of the lightcurve to be the one that gave the lowest reduced χ^2 and root mean square (RMS) of the residuals.

Prior to any further data analysis, the lightcurve intensities are converted to electron counts following the method described in the Spitzer handbook (multiply by EXPTIME*GAIN/FLUXCONV). This allows us to calculate the photometric errors using Poisson statistics.

2.3.1.2 Instrumental Systematic Modelling

Spitzer lightcurves exhibit significant amounts of correlated noise, which has been extensively studied and documented in the literature (Charbonneau et al. 2005; Agol et al. 2010;

Seager & Deming 2010; ?). The dominant source of this red noise at 3.6 and 4.5 μm is caused by an intrapixel sensitivity. Variations in the telescope pointing combined with undersampling of the stellar PSF results in variations in the centroiding with time $\sim 10\%$ of a pixel. When combined with the intrapixel sensitivity, this results in variations in the photometric lightcurve of order 1%, which is problematic since the atmospheric signal we are trying to extract is on the order of 0.01%. There have been many different methods developed for dealing with these systematics (e.g., Reach et al. 2005; Charbonneau et al. 2008; Ballard et al. 2010; Stevenson et al. 2012; Gibson et al. 2012; Morello et al. 2015; Deming et al. 2015). Ingalls et al. (2016) presented the results of a data challenge on synthetic and real eclipse data of XO-3b, in which several systematic correction methods were tested against each other. They found that BLISS (Stevenson et al. 2012), Pixel Level Decorrelation (PLD) (Deming et al. 2015), and ICA techniques (Morello et al. 2015) were the most precise for correcting the systematics of data of similar quality to XO-3b. PLD achieved the highest accuracy to the synthetic input data (Deming et al. 2015). Thus, we present the results of the pixel level decorrelation function for correcting our systematics and, for comparison, we also test the polynomial function presented in Knutson et al. (2008).

Pixel Level Decorrelation Unlike most methods of systematic correction, PLD does not use the centroid position of the stellar PSF on the pixel as an input (Deming et al. 2015). PLD relates the intensities of the individual pixels directly to the photometry in one numerical step, whereas the other methods used two numerical steps: first finding the centroid position of the star and then relating that to the measured photometry with a different numerical process. To bypass this secondary measurement, PLD assumes that the measured brightness of the star is a smooth function of position. One can Taylor expand this continuous and differentiable function such that the flux of the star can be expressed as a linear sum of the individual pixel fluxes (described fully in Deming et al. (2015)).

$$\Delta S^t = \sum_{i=1}^N c_i \hat{P}_i^t + DT(t) + ft + h \quad (2.1)$$

Where S^t is the flux measured over time and Δ represents the total fluctuations from all sources. $\hat{P}_i^t = \frac{P_i^t}{\sum_{i=1}^N P_i^t}$ represents the normalized flux from pixel i at time t . Here, i is an integer pixel number, where a 2D grid of pixels centered on the PSF is chosen, each pixel being indexed with a single number. The number of pixels included can be selected depending on the size of the PSF and the brightness of the star. In our survey, we uniformly take a 2-dimensional grid of 3x3 pixels containing the PSF of the star on the middle pixel. $DT(t)$ is the transit shape, and $ft + h$ is a temporal ramp which is a typical behavior of warm Spitzer lightcurves due to the residual telescope pointing.

Polynomial We also corrected the intrapixel variations using the polynomial function of the position presented in Knutson et al. (2008). $F_{corr} = F(K_0 + K_1(x - x_0) + K_2(x - x_0)^2 +$

$K_3(y - y_0) + K_4(y - y_0)^2$, where x_0 and y_0 are the integer pixel numbers plus 0.5, such that the polynomial is a function of the distance from the center of the pixel, where it is understood to be the most sensitive (Stevenson et al. 2012). Similarly to the PLD, we opted to use a linear function of time to correct the ramp over the entire lightcurve.

2.3.1.3 Fitting lightcurves to obtain transit parameters

Transit Model The transit shape ($DT(t)$) was calculated using Batman (Kreidberg 2015). Batman produces a transit lightcurve with 9 tunable parameters: time of inferior conjunction (days), orbital period (days), planet radius (in units of R_s), semi-major axis (in units of R_s), orbital inclination (deg), eccentricity, angle of periastron (deg), limb darkening model and limb darkening coefficients.

We fixed the orbital period for all of our planets to the values from the literature (Table 2.7). Several planets in our sample have reported values of the eccentricity and angle of periastron passage, as a test for these planets we ran a fit of both a circular and an eccentric orbit and found that the eccentricity did not affect the measured transit depth. We thus fixed the eccentricity and angle of periastron to zero for the remainder of the analysis.

Limb Darkening Southworth (2008) demonstrated that the choice of limb darkening can affect the measured planetary radius. This is particularly important in the optical wavelengths where the limb darkening effects are stronger, however we investigated the effects for each of our planets as a standard output of our pipeline. We started by using linear coefficients for the limb-darkening law, which were calculated using the 1D Atlas code from Sing (2010) for the $3.6\ \mu\text{m}$ and $4.5\ \mu\text{m}$ Spitzer channels. We translated the interpolation routine from IDL to Python and interpolated the linear limb-darkening values and their 1σ errors using the effective temperature, surface gravity, and metallicity of every star in our sample (Table 2.7). We were then able to vary the limb darkening coefficients within the uncertainties and confirm that the limb-darkening does not have significant impact on the resulting measured transit depth at these wavelengths. For this reason, we fixed the limb-darkening to the linear coefficients for the remainder of the analysis.

This leaves 4 tunable parameters: the time of inferior conjunction (t_0), planet radius (R_p/R_s), semi-major axis (a/R_s) and the orbital inclination (i). The fixing and varying of these parameters is discussed in Section 2.3.1.3.

Estimating Uncertainties using MCMC After the optimum pipeline parameters and the cutting time at the beginning and end of the lightcurve were determined we performed a full statistical analysis on the photometric transit lightcurves to estimate the uncertainties and study the co-variances of the parameters.

Before performing any fitting, we normalized the lightcurves, which allowed us to directly compare the PLD values and the photon flux timeseries in each pixel with each other. An initial normalization was done by taking the median of the first 100 data points in the

lightcurve. We then performed an initial Levenberg-Marquardt least-squares fit to get the preliminary transit parameters, which were then used to cut out the transit and so that the normalisation scale was recalculated such that the median of the out-of-transit flux was 1.

A second least squares fit was performed before performing a 4σ clip of the residuals to remove any outlying photometric points not captured in the centroiding clipping. We performed a final least squares on the normalized σ clipped data to determine the initial guess for the parameters as an input for our Markov Chain Monte Carlo analysis. We first calculated the errors on the photometric points using Poisson statistics assuming photon noise (\sqrt{N}). Then, after the first initial least squares fit, we determine how close we are to photon noise for each fit and scale up the uncertainties. These results are shown in Table 2.10. As is commonly found for Spitzer timeseries transit observations our uncertainties are around 20-50% above the photon noise limit for the whole survey. Scaling up the uncertainties on the photometric points by this factor before running the final fit results in a reduced χ^2 of ~ 1 , which prevents us from underestimating the uncertainties on the physical transit parameters.

We estimated the uncertainties on the best-fit parameters using emcee, the open source Affine-Invariant Metropolis-Hastings algorithm for Markov Chain Monte Carlo analysis developed by Foreman-Mackey et al. (2013). We initialized the MCMC chains with 100 walkers, 1000 burn-in steps, and 2000 production steps. We also performed a prayer-bead analysis of the uncertainties as a sanity check, but here we adopt the results from the MCMC analysis, since the sampling can be much larger. For each MCMC run, we checked for convergence with the emcee recommended acceptance fraction (0.2-0.5) and the Gelman-Rubin statistic (≤ 1.1) (Gelman & Rubin 1992). If the signal to noise of the data was low, sometimes the MCMC had an extremely low acceptance fraction. When this happened, we doubled the number of walkers until proper convergence was achieved. We derived the 1σ error bars asymmetrically as 34% above and below the median.

Our combined astrophysical and instrumental (PLD) noise model has 14 free parameters in total for the first fit. We treated the two distinct groups of planets slightly differently in our data reduction. The planets were split into two groups, lower SNR planets (generally cooler with longer periods) and higher SNR planets (short-period hot Jupiters). For the higher SNR planets, we let t_0 , R_p/R_s , a/R_s and i free in the initial fit with uniform priors on all parameters, then we performed a second MCMC fit where we used a 1σ Gaussian prior on a/R_s and i based on the results from the first fit. For the lower SNR planets, where it is difficult to detect the transit in each individual lightcurve, we need to fix a/R_s and i to the literature values for the fitting. For both of these methods, the walkers are initialized in a tight cluster around the best fit Levenberg-Marquardt minimization. These lower SNR planets also had multiple transits in each band-pass, these were each analyzed, and the average transit depth was calculated using the weighted sum, where the weight is the inverse variance multiplied by an "over dispersion" factor as done in Ingalls et al. (2016). The over dispersion factor allows for underestimation of the individual uncertainties, see Lyons (1992) for further information.

Special Cases The systematics of WASP-13b were not properly captured by our pipeline, such that a bump at the end of the transit remained in the reduced light curve at $3.6\text{ }\mu\text{m}$. This had the consequence of making our fitted transit depth shallower than it would be. We thus removed this data from our fit and ran the pipeline again to get the optimal parameters and transit depths. In total we removed 36 minutes from the last quarter of the in-transit flux, however, the egress remained intact allowing us to still characterize the system.

Similarly, the $3.6\text{ }\mu\text{m}$ transit of WASP-131b showed a bump in the baseline before transit, likely a starspot occultation. Therefore, we also removed 50 minutes of flux in our MCMC fit.

Furthermore, our approach was slightly modified for HAT-P-26b due to its low signal-to-noise ratio, we set Gaussian priors on the semi-major axis and inclination in the initial fits based on the literature values.

2.3.2 Interpreting Transmission Spectrophotometry with 1-D Atmospheric Modeling

To interpret the results from our survey of transiting hot Jupiters, we compare the IRAC transit depths with a grid of simulated atmospheric spectra. First, double-gray analytical formulae are applied to construct the cloud-free temperature-pressure (T-P) profiles for a wide range of stellar irradiation Heng et al. (2014). Second, we use a photochemical kinetics model (VULCAN, Tsai et al. (2017) see Section 2.3.2.3) to compute the composition under the effects of photo-dissociation and vertical mixing. The T-P profiles and the chemical composition are not self-consistently computed, here, we focus on how the stellar flux impacts the disequilibrium chemistry. Last, a radiative transfer code (PLATON Zhang et al. (2019), see Section 2.3.2.4) is used to create transmission spectra to compare with the observational data. Our fiducial model grid spans a range of equilibrium temperatures (T_{eq}) from around 400 K to around 2400 K in ~ 100 K steps, planetary surface gravities (g_p) 500, 1500, 5000 , planet radius (R_p) 0.5, 1, 1.5, 2 R_{jup} and stellar radius (R_s) 0.5, 1, 1.5, 2 R_{\odot} with 1x solar composition and equilibrium chemistry (no vertical mixing, no photo-chemistry, no boundary fluxes). We then expand our modeling in two dimensions. First, we incorporate non-equilibrium processes and capture vertical mixing in the form of an eddy diffusion coefficient (K_{zz}). Second, we test the effects of higher metallicity by creating the full set of grids with 30x solar metallicity. We describe the creation of these grids in full detail below.

2.3.2.1 Stellar Irradiation and T-P profiles

In our survey, most hot Jupiters populate a small range of close-in orbits, $a_{\text{mean}} = 0.037 \pm 0.013$ AU, while the parent stars span several spectral types, from early M stars to F stars. In fact, the stellar temperature varies from about 3000 K to 7000 K, while the radius also increases with earlier stellar types. Since for a planet at orbital distance (a) around a star with radius (R_s) and effective temperature (T_{eff}), the equilibrium temperature of the planet

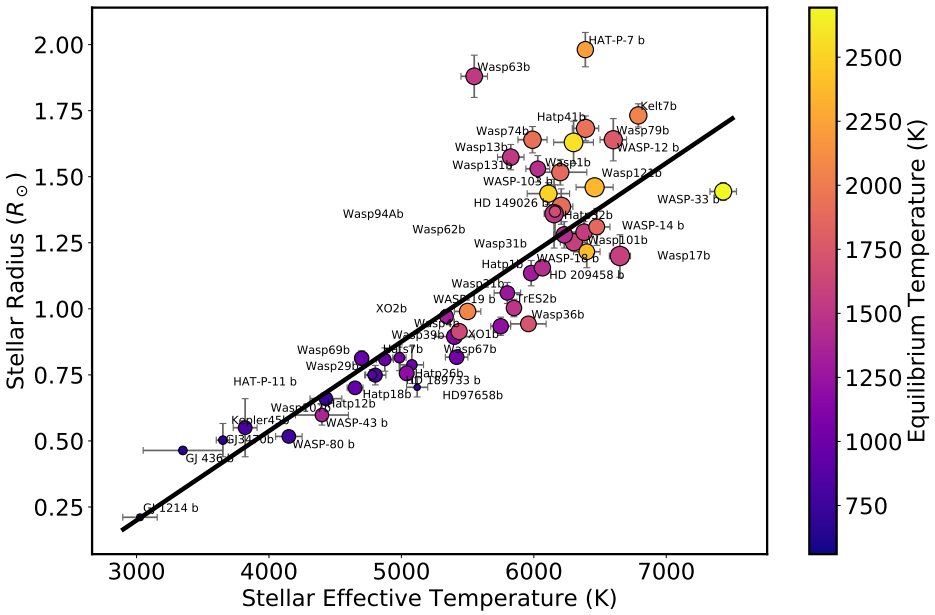


Fig. 2.2: Stellar Radius as a function of stellar effective temperature. Black line shows first order polynomial best fit used for creation of T-P grid (see Section 2.3.2.1). Color of points shows the equilibrium temperature of the planets, size of points is scaled to the planet radius.

(T_{eq}) is proportional to $T_{\text{eff}}(R_s/a)^{1/2}$. The stellar flux plays a bigger factor in determining the irradiation the planet received and its effective temperature. In this regard, we assume a fixed orbital distance for our model grid to isolate the effects of stellar irradiation. The mean value of the samples, 0.035 AU, is taken across the grid. In this setting, the effective temperature of the model planet is entirely determined by the stellar luminosity, and not by the orbital distance. We also note that the intrinsic temperature (T_{int}) is negligible and thus the effective temperature ($T_{\text{eff}}^4 = T_{\text{eq}}^4 + T_{\text{int}}^4$) is the same as the equilibrium temperature. Additionally, our assumed value of $T_{\text{int}}=150$ K has little effect on our model temperature pressure profiles of the hot Jupiters.

The next step is to determine the size, hence the energy flux of the stars. For main-sequence stars which follow the mass–luminosity and mass-radius relations, we fit a power law relation between the radius and effective temperature, see Figure 2.2. The power law fitting to our sample yields the following expression for the stellar radius: $R_S = m * T_{\text{eff}} + b$ where m and b are 0.0003381 and -0.81495, respectively. Once the effective temperature and the radius of the star are known, there is enough information to specify the incident irradiation of the model atmospheres.

We then compute the T-P profiles for the given stellar irradiation using the analytical double-gray radiative equilibrium solutions in Heng et al. (2014) (Equation 126.).

The parameters used in this calculation are chosen to match numerical radiative transfer results, listed in Table 2.3. Similar to the prescriptions in Guillot (2010) and Parmentier & Guillot (2014), the opacities do not have a pressure dependence. We reiterate that this relation allows us to uniquely express the equilibrium temperature of a planet at a given orbital distance as a function of stellar temperature. Our stellar grid, with effective temperatures from 3250 to 7000 K, produces irradiated atmospheres of temperature from 446 to 2248 K, at 0.035 AU. To reach the temperatures of the ultra-hot Jupiters we also run additional models with an orbital distance at 0.02 AU. The resulting temperature pressure profiles are shown in Figure 2.4.

The simple prescription allows us to explore the parameter space in a basic way and to focus on the correlation with stellar irradiation. Although the intrinsic temperature is held constant in our T-P profiles, the realistic interior can be potentially hotter. Tremblin et al. (2017) and Sainsbury-Martinez et al. (2019) have shown that circulation can transport entropy downward and leads to a hotter deep interior over time. Thorngren et al. (2019) suggested much higher T_{int} for observed hot Jupiters (with $T_{\text{eq}} \gtrsim 1300$ K) than the 100K commonly assumed in GCMs. Fortney et al. (2020) also investigated the effects of heating from tidal dissipation for warm Jupiters (with $T_{\text{eq}} \gtrsim 1300$ K) with simplified chemical timescale analysis. The upshot of the hotter interior is lowering the quenched [CH4]/[CO] ratio. In short, a hot deep interior changes the expectation for equilibrium chemistry in deep layers, hence the expectation from disequilibrium chemistry higher up. Since the equilibrium abundance of CH4 generally increases with depth (at least in our solar and 30x solar models), lowering vertical mixing also results in a lower [CH4]/[CO] ratio and can effectively be degenerate with a hotter interior. However, we find high vertical mixing matches the hot Jupiters better, even with the lower T_{int} of 150 K. Increasing the interior temperature will reduce CH4, so even higher vertical mixing would be required to recover the same CH4 abundance for these planets. As for the cooler planets, the signature leading to our inference of low vertical mixing can also be explained by a hot interior if there is actually no CH4 in the deep hot atmosphere. However, the sources of internal heating and their exact interior temperature for these cool planets are rather uncertain (see Fortney et al. (2020) for a detailed discussion).

In addition to this, our prescription for PT profiles is simplified compared to 1D radiative/convective models. Nevertheless, in this study, we are interested in the relative difference between two broad bandpasses (3.6 and 4.5 μm), and thus the prescription used for the TP profiles is less critical than for absolute measurements. The relative difference between 3.6 and 4.5 μm is globally similar for our prescription as compared to the 1D RC models. We acknowledge that the vertical mixing is likely to be affected by the choice of TPs, however testing this difference is beyond the scope of our current study.

Our simple model emphasizes the importance of the degeneracies between vertical mixing, interior temperature, and equilibrium chemistry, but is also a limit to the interpretation. A more detailed approach than the simple model we used is required to study the impact of the various processes on the observations with greater accuracy. However, such detailed study will also be limited by the unknown interior temperature. Therefore, we limit ourselves

Table 2.3: Fixed parameters used in the double-grey radiative equilibrium solution for creating temperature pressure profiles. For each TP profile we show the fixed irradiation temperature (T_{irr}), intrinsic temperature (T_{int}), longwave opacity (κ_L), shortwave opacity (κ_S), longwave scattering parameter (β_L) and the shortwave scattering parameter (β_S).

T_{irr}	T_{int}	κ_L	κ_S	β_L	β_S
631	150	0.02	0.00035	1	1
775	150	0.02	0.00068	1	1
919	150	0.02	0.001	1	1
1069	150	0.02	0.0014	1	1
1222	150	0.02	0.0017	1	1
1379	150	0.02	0.0019	1	1
1540	150	0.02	0.0022	1	1
1706	150	0.02	0.0035	1	1
1875	150	0.02	0.0038	1	1
2049	150	0.02	0.004	1	1
2227	150	0.02	0.0043	1	1
2410	150	0.02	0.006	1	1
2595	150	0.02	0.006	1	1
2786	150	0.02	0.006	1	1
2980	150	0.02	0.0061	1	1
3179	150	0.02	0.0062	1	1

to a simple approach as a sophisticated analysis with more advanced temperature pressure profiles is beyond the scope of this paper.

2.3.2.2 Grid of stellar spectra

As the effective temperature of the star rises, the spectral energy distribution shifts to shorter wavelengths. We therefore adopted the stellar spectral grid from (Rugheimer et al. 2013), which ranges from 4250 to 7000 K and covers F0 to K7 spectral types. The models start with the synthetic ATLAS spectra (Kurucz 1979) and then we co-add the observed spectra from International Ultraviolet Explorer for UV ($<= 300$ nm). See (Rugheimer et al. 2013) for the detailed stellar grid setup. Additionally, for late K and M stars ($T_{\text{eff}} < 4250$ K), we picked GJ 436 ($T_{\text{eff}} = 3350$ K) as our fiducial star. The high resolution spectrum of GJ436 is taken from the MUSCLES survey (France et al. 2016)¹ and scaled for the stellar fluxes with effective temperatures of 3250 K, 3500 K, 3750 K, and 4000 K.

¹<http://cos.colorado.edu/kevinf/muscles.html>

2.3.2.3 Modeling the photo-chemical kinetics with VULCAN

We explore the effects of photolysis, atmospheric mixing, and metallicity by using a photochemical kinetics model, VULCAN (Tsai et al. 2017)². The code solves the steady-state chemical compositions for a given temperature-pressure profile and has been benchmarked for hot Jupiters. In this work, we use the updated version that includes nitrogen chemistry and photochemistry (Tsai et al. in preparation). The chemical model with updated nitrogen chemistry and photochemistry has been tested on nitrogen dominated atmospheres for super-Earths (Zilinskas et al. 2020). The N-C-H-O network consists of about 600 thermal reactions (including forward and reverse) and 40 photodissociation reactions. We validate our updated model against the one-dimensional photochemical and thermochemical kinetics and diffusion model presented in Moses et al. (2011) for HD209458b, see Figure 2.16.

Vertical mixing is simulated through means of an eddy diffusion co-efficient (K_{zz}), which assumes that atmospheric motion resembles diffusion when convection and turbulence occur on much smaller scales than the magnitude of the pressure scale height. We vary the eddy diffusion coefficient to explore various strengths of vertical mixing, with constant values of 10^8 , 10^{10} , and 10^{12} . The choice of the values is consistent with those extracted from GCM simulations (Moses et al. 2011; Parmentier et al. 2013; Zhang & Showman 2018; Komacek et al. 2019). Furthermore, the elemental abundance of the atmosphere is assigned to two different metallicities: 1x solar and 30x solar (Lodders et al. 2009).

2.3.2.4 Creating the transmission spectra with PLATON

Finally, transmission spectra are then simulated using the open-source, transit-depth calculator and retrieval tool, PLATON (Zhang et al. 2019)³. The code has been modified to take non-equilibrium compositions from our calculation, including CH₄, CO, CO₂, C₂H₂, H₂O, O₂, OH, C₂H₄, C₂H₆, H₂CO, HCN, NH₃, NO. The main opacities relevant for the wavelengths of Spitzer/IRAC are displayed in Figure 2.3. We assume chemical equilibrium for the rest of the species in PLATON. The details of the forward model can be found in Zhang et al. (2019). We neglect stellar limb darkening in these models and the synthetic transit depth is expressed as $(R_p/R_s)^2$.

2.3.2.5 Calculating the model Spitzer/IRAC transit depths

We integrate the simulated transmission spectra with Spitzer/IRAC spectral response functions and weight with the stellar flux using the following equation:

$$\bar{\delta}_\lambda = \frac{\int_0^\infty \delta(\lambda) \lambda R(\lambda) F_s(\lambda) d\lambda}{\int_0^\infty \lambda R(\lambda) F_s(\lambda) d\lambda} \quad (2.2)$$

²<https://github.com/exoclime/VULCAN>

³<https://platon.readthedocs.io/en/latest/intro.html>

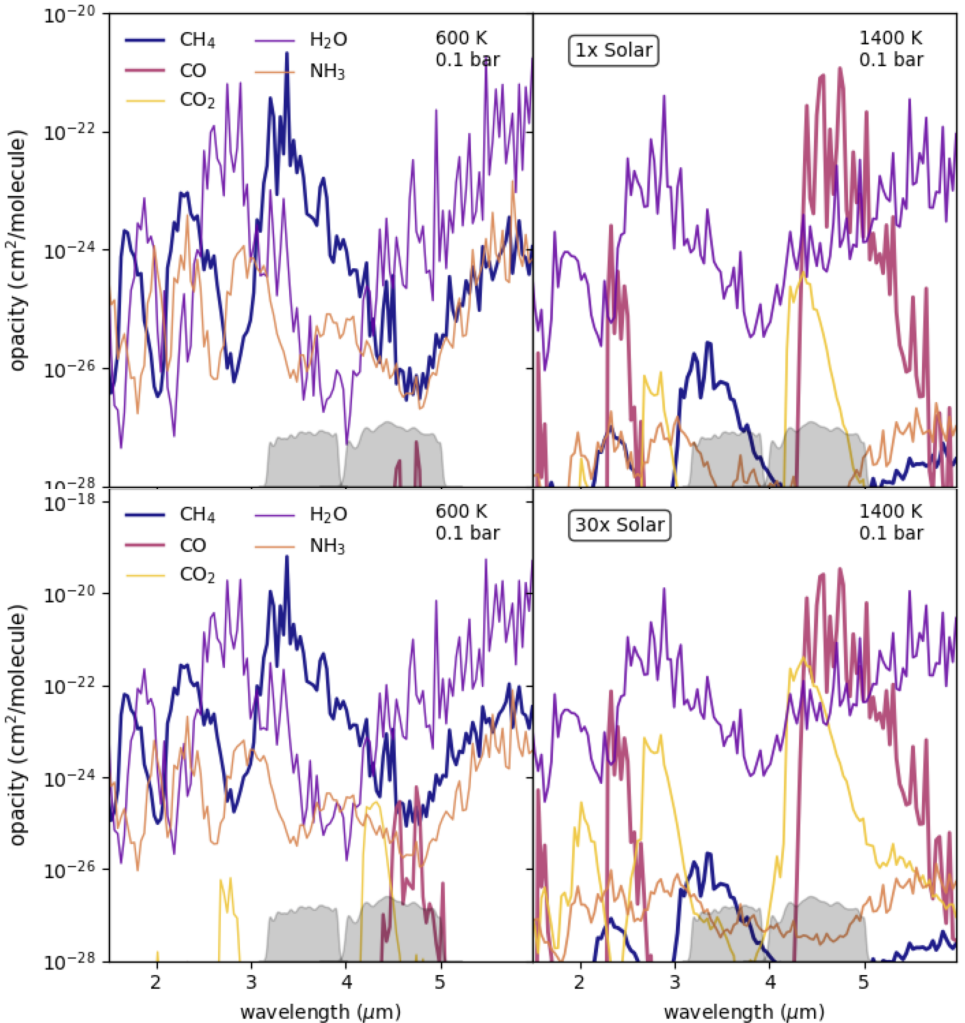


Fig. 2.3: Opacities for a chemical equilibrium atmosphere at 600 K (left) and 1400 K (right) at 0.1 bar. Top panels show the abundance weighted opacities for a solar composition atmosphere and the bottom panels show the abundance weighted opacities for a 30x solar composition atmosphere. Carbon monoxide, water, methane and carbon dioxide (for 30x solar) are the dominant absorbing species at the two IRAC channels (3.6 and 4.5 μm).

where $R(\lambda)$ is the spectral response function at either $3.6\ \mu\text{m}$ or $4.5\ \mu\text{m}$ [e-/photon] (Quijada et al. 2004) and $\delta(\lambda)$ is the transmission spectrum from PLATON and $F_s(\lambda)$ is the stellar flux. The output, $\bar{\delta}_\lambda$, is the weighted average transit depth that would be observed with Spitzer/IRAC in either of the two bandpasses.

Figure 2.6 shows the interpolated grid of fiducial models (solar composition, cloud-free with equilibrium chemistry), we plot the normalized IRAC transit depth difference against the equilibrium temperature, and overplot the results from our transit survey. Figure 2.7 shows the different tracks of the model grid that made up the shaded regions and Figure 2.8 shows the different vertical mixing and metallicity interpolated grids with the data. For the cloudy grid, we simply assume a gray cloud opacity such that the spectra are flat and thus the transit depth difference would be zero, which is shown as a vertical line on Figures 2.6 and 2.8.

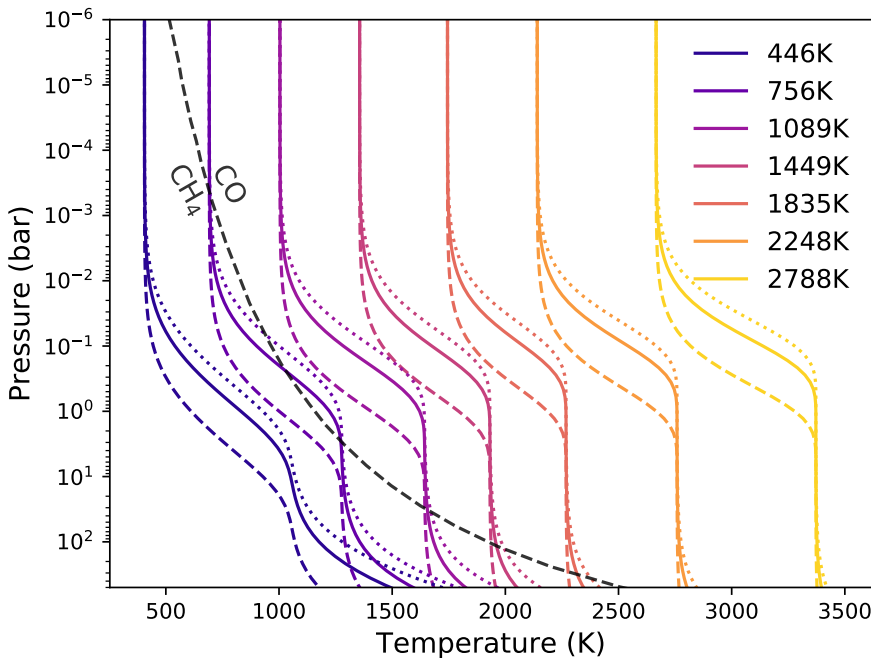


Fig. 2.4: Analytical Temperature-Pressure profiles for grid of models spanning equilibrium temperatures ~ 400 - 2800 K, showing every ~ 400 K. For each temperature we show three profiles where the surface gravity is varied: dotted, solid and dashed lines represent 500, 1000 and 5000 respectively. Grey dashed line represents the gas transition between CH4 and CO dominated atmospheres when chemical equilibrium is assumed.

2.4 Results

2.4.1 Measured transit depths and their ratios

2.4.1.1 Results of measured transit depths

Table 2.4: Results from the MCMC analysis, we show the semi-major axis (a/R^*), the inclination (degrees), the percentage transit depth (R_p/R_s)², the corresponding impact parameter (b) and the mid-transit time in BJD_UTC. Values for the semi-major axis and the inclination are from the initial MCMC fits and then these are fixed with gaussian priors for a second MCMC run where the final values for the transit depths are determined.

Planet	λ (μm)	a/R^*	inc degrees	depth $(R_p/R_s)^2$	b	T0 BJD_UTC
HAT-P-32 b	3.6	$6.13^{+0.02}_{-0.02}$	$89.5^{+0.3}_{-0.5}$	$2.15^{+0.01}_{-0.01}$	$0.05^{+2.06}_{-2.90}$	$2456250.103520^{+0.000112}_{-0.000120}$
HAT-P-32 b	4.5	$6.13^{+0.02}_{-0.04}$	$89.4^{+0.4}_{-0.6}$	$2.21^{+0.02}_{-0.02}$	$0.06^{+2.62}_{-3.95}$	$2456370.504208^{+0.000154}_{-0.000152}$
XO-1 b	3.6	$11.46^{+0.05}_{-0.11}$	$89.5^{+0.3}_{-0.4}$	$1.67^{+0.01}_{-0.01}$	$0.09^{+3.56}_{-4.43}$	$2456426.076095^{+0.000115}_{-0.000120}$
XO-1 b	4.5	$11.24^{+0.20}_{-0.23}$	$88.8^{+0.5}_{-0.4}$	$1.72^{+0.01}_{-0.01}$	$0.24^{+5.40}_{-4.49}$	$2456437.900819^{+0.000158}_{-0.000157}$
HAT-P-1 b	3.6	$9.91^{+0.13}_{-0.13}$	$85.7^{+0.1}_{-0.1}$	$1.40^{+0.01}_{-0.01}$	$0.74^{+0.99}_{-0.99}$	$2456547.478364^{+0.000156}_{-0.000150}$
HAT-P-1 b	4.5	$10.07^{+0.16}_{-0.15}$	$85.8^{+0.1}_{-0.1}$	$1.39^{+0.01}_{-0.01}$	$0.73^{+1.25}_{-1.17}$	$2456556.409109^{+0.000187}_{-0.000190}$
WASP-17 b	3.6	$7.16^{+0.14}_{-0.16}$	$88.1^{+0.8}_{-0.7}$	$1.52^{+0.01}_{-0.01}$	$0.24^{+6.05}_{-4.97}$	$2456423.188874^{+0.000233}_{-0.000221}$
WASP-17 b	4.5	$7.24^{+0.09}_{-0.15}$	$88.6^{+0.8}_{-0.8}$	$1.57^{+0.02}_{-0.02}$	$0.17^{+6.13}_{-5.89}$	$2456426.923243^{+0.000288}_{-0.000285}$
WASP-39 b	3.6	$10.47^{+0.19}_{-0.17}$	$87.0^{+0.2}_{-0.2}$	$2.15^{+0.02}_{-0.02}$	$0.56^{+1.83}_{-1.68}$	$2456401.396438^{+0.000159}_{-0.000176}$
WASP-39 b	4.5	$11.38^{+0.28}_{-0.25}$	$87.7^{+0.3}_{-0.2}$	$2.16^{+0.02}_{-0.02}$	$0.45^{+3.14}_{-2.66}$	$2456575.774315^{+0.000200}_{-0.000194}$
HAT-P-12 b	3.6	$11.23^{+0.26}_{-0.26}$	$88.0^{+0.3}_{-0.3}$	$1.89^{+0.01}_{-0.01}$	$0.39^{+3.64}_{-3.30}$	$2456359.882148^{+0.000131}_{-0.000138}$
HAT-P-12 b	4.5	$10.90^{+0.35}_{-0.30}$	$87.8^{+0.4}_{-0.3}$	$1.93^{+0.03}_{-0.03}$	$0.41^{+4.47}_{-3.60}$	$2456363.095398^{+0.000197}_{-0.000187}$
HAT-P-18 b	3.6	$15.28^{+0.47}_{-0.41}$	$88.5^{+0.3}_{-0.3}$	$1.77^{+0.02}_{-0.02}$	$0.41^{+5.19}_{-4.07}$	$2456461.067141^{+0.000195}_{-0.000197}$
HAT-P-18 b	4.5	$15.48^{+0.45}_{-0.44}$	$88.5^{+0.3}_{-0.3}$	$1.93^{+0.02}_{-0.02}$	$0.41^{+5.07}_{-4.47}$	$2456483.099518^{+0.000215}_{-0.000215}$
TrES-2 b	3.6	$7.96^{+0.16}_{-0.15}$	$83.9^{+0.2}_{-0.2}$	$1.37^{+0.02}_{-0.02}$	$0.84^{+1.33}_{-1.34}$	$2456252.834601^{+0.000203}_{-0.000196}$
TrES-2 b	4.5	$8.20^{+0.25}_{-0.23}$	$84.2^{+0.3}_{-0.2}$	$1.40^{+0.02}_{-0.02}$	$0.83^{+2.09}_{-1.92}$	$2456257.775215^{+0.000268}_{-0.000267}$
WASP-4 b	3.6	$5.58^{+0.03}_{-0.04}$	$89.3^{+0.5}_{-0.7}$	$2.28^{+0.02}_{-0.02}$	$0.07^{+2.71}_{-4.14}$	$2456288.955465^{+0.000137}_{-0.000142}$
WASP-4 b	4.5	$5.46^{+0.05}_{-0.11}$	$88.7^{+0.9}_{-1.3}$	$2.34^{+0.03}_{-0.03}$	$0.12^{+4.80}_{-7.20}$	$2456292.969500^{+0.000208}_{-0.000212}$
XO-2 b	3.6	$8.17^{+0.09}_{-0.17}$	$88.9^{+0.7}_{-0.8}$	$1.07^{+0.01}_{-0.01}$	$0.15^{+5.81}_{-6.13}$	$2456295.370617^{+0.000139}_{-0.000140}$
XO-2 b	4.5	$7.77^{+0.22}_{-0.22}$	$87.6^{+0.7}_{-0.6}$	$1.07^{+0.01}_{-0.01}$	$0.33^{+5.43}_{-4.50}$	$2456292.754728^{+0.000198}_{-0.000191}$
GJ3470 b	3.6	$14.63^{+0.52}_{-0.50}$	$88.4^{+0.3}_{-0.3}$	$0.57^{+0.01}_{-0.01}$	$0.42^{+4.13}_{-3.73}$	$2456284.001794^{+0.000118}_{-0.000115}$
GJ3470 b	4.5	$14.41^{+0.65}_{-0.54}$	$88.4^{+0.4}_{-0.3}$	$0.61^{+0.01}_{-0.01}$	$0.41^{+5.23}_{-4.09}$	$2456294.011801^{+0.000151}_{-0.000150}$
WASP-21 b	3.6	$9.55^{+0.30}_{-0.28}$	$87.1^{+0.4}_{-0.4}$	$1.08^{+0.01}_{-0.01}$	$0.49^{+3.75}_{-3.34}$	$2456532.561048^{+0.000261}_{-0.000260}$
WASP-21 b	4.5	$9.61^{+0.40}_{-0.34}$	$87.1^{+0.5}_{-0.4}$	$1.14^{+0.02}_{-0.02}$	$0.48^{+5.28}_{-4.23}$	$2456536.882998^{+0.000308}_{-0.000322}$
WASP-31 b	3.6	$8.06^{+0.20}_{-0.18}$	$84.5^{+0.2}_{-0.2}$	$1.54^{+0.02}_{-0.02}$	$0.77^{+1.81}_{-1.66}$	$2456360.907660^{+0.000317}_{-0.000328}$
WASP-31 b	4.5	$8.86^{+0.34}_{-0.32}$	$85.2^{+0.3}_{-0.3}$	$1.50^{+0.03}_{-0.03}$	$0.74^{+2.86}_{-2.77}$	$2456371.125690^{+0.000407}_{-0.000412}$
WASP-1 b	3.6	$5.72^{+0.03}_{-0.05}$	$89.3^{+0.5}_{-0.8}$	$1.07^{+0.01}_{-0.01}$	$0.07^{+2.91}_{-4.60}$	$2456361.902274^{+0.000263}_{-0.000250}$
WASP-1 b	4.5	$5.41^{+0.17}_{-0.20}$	$86.5^{+1.2}_{-1.1}$	$1.09^{+0.02}_{-0.02}$	$0.33^{+6.58}_{-6.12}$	$2456371.982150^{+0.000354}_{-0.000364}$

Table 2.4: continued.

Planet	λ (μm)	a/R*	inc degrees	depth $(R_p/R_s)^2$	b (%)	T0 BJD_UTC
HAT-P-26 b	3.6	13.22 ^{+0.75} _{-0.94}	88.3 ^{+0.8} _{-0.7}	0.53 ^{+0.01} _{-0.01}	0.39 ^{+10.08} _{-9.85}	2456545.361384 ^{+0.000296} _{-0.000288}
HAT-P-26 b	4.5	13.92 ^{+0.16} _{-0.32}	89.5 ^{+0.3} _{-0.6}	0.55 ^{+0.01} _{-0.01}	0.11 ^{+4.33} _{-8.72}	2456405.622835 ^{+0.000356} _{-0.000364}
WASP-107 b	3.6	18.19 ^{+0.03} _{-0.04}	89.9 ^{+0.1} _{-0.1}	1.96 ^{+0.01} _{-0.01}	0.04 ^{+1.45} _{-2.26}	2457876.124941 ^{+0.000060} _{-0.000064}
WASP-107 b	4.5	18.09 ^{+0.05} _{-0.09}	89.8 ^{+0.1} _{-0.2}	2.06 ^{+0.01} _{-0.01}	0.06 ^{+2.54} _{-3.09}	2457870.403743 ^{+0.000081} _{-0.000077}
WASP-13 b	3.6	7.64 ^{+0.20} _{-0.19}	85.6 ^{+0.4} _{-0.3}	0.86 ^{+0.01} _{-0.01}	0.58 ^{+2.70} _{-2.50}	2456480.940869 ^{+0.000231} _{-0.000246}
WASP-13 b	4.5	7.78 ^{+0.27} _{-0.23}	85.7 ^{+0.4} _{-0.4}	0.87 ^{+0.01} _{-0.01}	0.59 ^{+3.43} _{-2.85}	2456315.526437 ^{+0.000293} _{-0.000303}
WASP-121 b	3.6	3.84 ^{+0.02} _{-0.03}	88.9 ^{+0.8} _{-1.1}	1.47 ^{+0.01} _{-0.01}	0.07 ^{+2.95} _{-4.10}	2457906.807311 ^{+0.000148} _{-0.000144}
WASP-121 b	4.5	3.82 ^{+0.02} _{-0.03}	89.0 ^{+0.8} _{-1.3}	1.49 ^{+0.01} _{-0.01}	0.07 ^{+3.02} _{-4.80}	2457910.632374 ^{+0.000183} _{-0.000171}
WASP-69 b	3.6	12.26 ^{+0.09} _{-0.08}	86.8 ^{+0.0} _{-0.0}	1.60 ^{+0.00} _{-0.00}	0.68 ^{+0.60} _{-0.58}	2457992.354188 ^{+0.000053} _{-0.000054}
WASP-69 b	4.5	12.30 ^{+0.11} _{-0.10}	86.8 ^{+0.1} _{-0.1}	1.67 ^{+0.01} _{-0.01}	0.68 ^{+0.77} _{-0.71}	2457996.222243 ^{+0.000066} _{-0.000069}
WASP-67 b	3.6	13.50 ^{+0.39} _{-0.33}	86.2 ^{+0.2} _{-0.2}	1.97 ^{+0.03} _{-0.03}	0.91 ^{+2.28} _{-2.72}	2457776.271136 ^{+0.000219} _{-0.000220}
WASP-67 b	4.5	13.90 ^{+0.31} _{-0.39}	86.3 ^{+0.1} _{-0.1}	1.92 ^{+0.03} _{-0.03}	0.89 ^{+1.84} _{-1.93}	2457979.305753 ^{+0.000282} _{-0.000276}
HATS-7 b	3.6	11.09 ^{+0.62} _{-1.07}	88.2 ^{+1.0} _{-1.3}	0.38 ^{+0.02} _{-0.02}	0.35 ^{+11.03} _{-14.14}	2457694.120917 ^{+0.000590} _{-0.000538}
HATS-7 b	4.5	10.80 ^{+0.48} _{-0.91}	88.4 ^{+1.1} _{-1.2}	0.40 ^{+0.03} _{-0.03}	0.30 ^{+12.05} _{-13.12}	2457697.305788 ^{+0.000797} _{-0.000795}
WASP-29 b	3.6	12.58 ^{+0.05} _{-0.11}	89.7 ^{+0.2} _{-0.4}	0.95 ^{+0.01} _{-0.01}	0.07 ^{+2.95} _{-4.91}	2457807.234478 ^{+0.000115} _{-0.000120}
WASP-29 b	4.5	12.53 ^{+0.05} _{-0.08}	89.7 ^{+0.2} _{-0.3}	0.93 ^{+0.01} _{-0.01}	0.06 ^{+2.59} _{-4.13}	2457826.848225 ^{+0.000150} _{-0.000149}
HAT-P-41 b	3.6	5.53 ^{+0.03} _{-0.06}	89.0 ^{+0.7} _{-0.9}	1.00 ^{+0.01} _{-0.01}	0.10 ^{+3.76} _{-4.92}	2457772.203860 ^{+0.000220} _{-0.000217}
HAT-P-41 b	4.5	5.55 ^{+0.03} _{-0.04}	89.3 ^{+0.5} _{-0.8}	1.09 ^{+0.01} _{-0.01}	0.07 ^{+2.78} _{-4.43}	2457788.367795 ^{+0.000274} _{-0.000263}
WASP-101 b	3.6	8.60 ^{+0.17} _{-0.16}	85.2 ^{+0.2} _{-0.2}	1.18 ^{+0.01} _{-0.01}	0.73 ^{+1.55} _{-1.54}	2457760.332526 ^{+0.000170} _{-0.000175}
WASP-101 b	4.5	8.51 ^{+0.19} _{-0.18}	85.0 ^{+0.2} _{-0.2}	1.14 ^{+0.01} _{-0.01}	0.74 ^{+1.72} _{-1.64}	2457771.089626 ^{+0.000225} _{-0.000227}
WASP-131 b	3.6	8.34 ^{+0.20} _{-0.19}	85.0 ^{+0.2} _{-0.2}	0.61 ^{+0.01} _{-0.01}	0.73 ^{+1.88} _{-1.80}	2457696.837080 ^{+0.000253} _{-0.000256}
WASP-131 b	4.5	8.41 ^{+0.28} _{-0.26}	85.0 ^{+0.3} _{-0.3}	0.61 ^{+0.01} _{-0.01}	0.73 ^{+2.63} _{-2.53}	2457909.718452 ^{+0.000336} _{-0.000332}
WASP-36 b	3.6	6.06 ^{+0.25} _{-0.22}	83.7 ^{+0.6} _{-0.5}	1.78 ^{+0.03} _{-0.03}	0.67 ^{+3.75} _{-3.19}	2457805.166629 ^{+0.000262} _{-0.000262}
WASP-36 b	4.5	6.19 ^{+0.44} _{-0.39}	84.4 ^{+1.1} _{-1.0}	1.82 ^{+0.03} _{-0.03}	0.60 ^{+6.70} _{-6.13}	2457975.813843 ^{+0.000346} _{-0.000353}
WASP-63 b	3.6	6.26 ^{+0.23} _{-0.21}	86.6 ^{+1.0} _{-0.8}	0.61 ^{+0.01} _{-0.01}	0.37 ^{+6.38} _{-5.07}	2457865.520635 ^{+0.000353} _{-0.000330}
WASP-63 b	4.5	6.52 ^{+0.16} _{-0.21}	87.7 ^{+1.1} _{-1.0}	0.55 ^{+0.01} _{-0.01}	0.26 ^{+7.01} _{-6.45}	2457922.436423 ^{+0.000470} _{-0.000461}
WASP-79 b	3.6	7.31 ^{+0.15} _{-0.14}	85.9 ^{+0.3} _{-0.3}	1.20 ^{+0.01} _{-0.01}	0.52 ^{+2.36} _{-2.05}	2457713.374126 ^{+0.000167} _{-0.000167}
WASP-79 b	4.5	7.12 ^{+0.15} _{-0.14}	85.6 ^{+0.3} _{-0.3}	1.17 ^{+0.01} _{-0.01}	0.55 ^{+2.29} _{-2.02}	2457720.699409 ^{+0.000215} _{-0.000213}
WASP-94 Ab	3.6	7.34 ^{+0.02} _{-0.04}	89.5 ^{+0.3} _{-0.5}	1.12 ^{+0.01} _{-0.01}	0.06 ^{+2.43} _{-3.56}	2457795.021530 ^{+0.000147} _{-0.000147}
WASP-94 Ab	4.5	7.34 ^{+0.02} _{-0.04}	89.5 ^{+0.4} _{-0.5}	1.13 ^{+0.01} _{-0.01}	0.07 ^{+2.62} _{-3.61}	2457972.780291 ^{+0.000187} _{-0.000180}
WASP-74 b	3.6	4.75 ^{+0.08} _{-0.07}	79.7 ^{+0.3} _{-0.2}	0.87 ^{+0.01} _{-0.01}	0.85 ^{+1.17} _{-1.01}	2457768.164558 ^{+0.000178} _{-0.000176}
WASP-74 b	4.5	5.13 ^{+0.11} _{-0.10}	80.8 ^{+0.3} _{-0.3}	0.86 ^{+0.01} _{-0.01}	0.82 ^{+1.44} _{-1.42}	2457770.304101 ^{+0.000228} _{-0.000230}
WASP-62 b	3.6	9.47 ^{+0.16} _{-0.16}	88.2 ^{+0.4} _{-0.3}	1.29 ^{+0.01} _{-0.01}	0.30 ^{+3.57} _{-3.02}	2457717.229937 ^{+0.000138} _{-0.000138}
WASP-62 b	4.5	9.32 ^{+0.20} _{-0.18}	87.9 ^{+0.4} _{-0.3}	1.20 ^{+0.01} _{-0.01}	0.35 ^{+3.88} _{-3.05}	2457730.466206 ^{+0.000165} _{-0.000167}
Kepler-45 b	3.6	-	-	3.37 ^{+0.13} _{-0.13}	-	-
Kepler-45 b	4.5	-	-	3.50 ^{+0.14} _{-0.14}	-	-

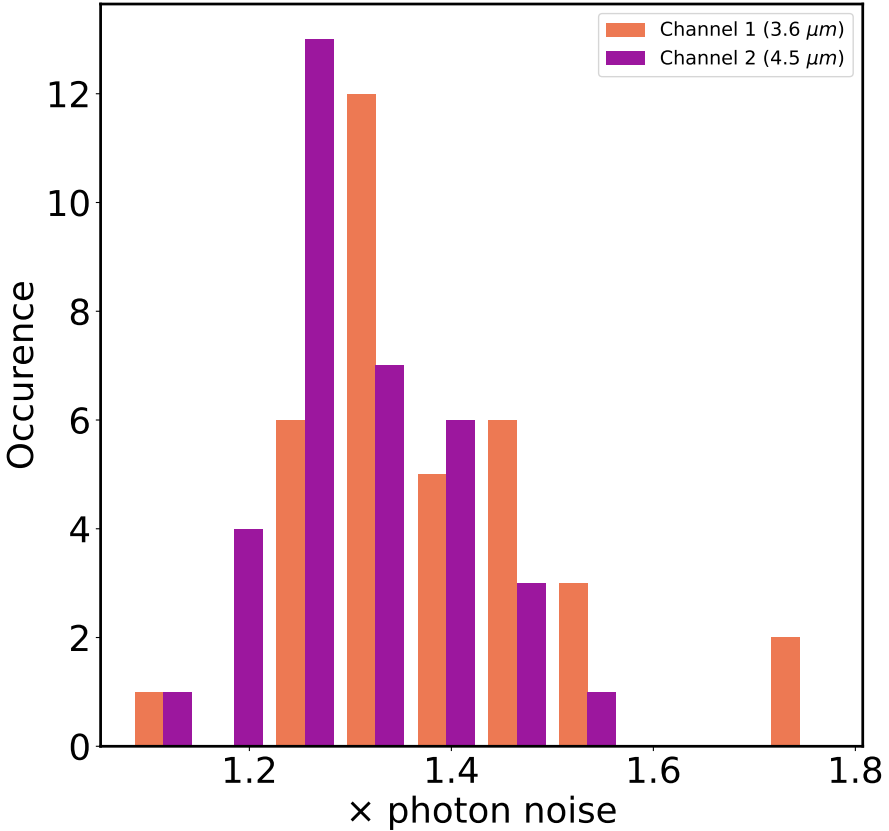


Fig. 2.5: Histogram showing the percentage above photon noise for each of the individual lightcurves. Channel 1 ($3.6 \mu\text{m}$) is displayed in orange and channel 2 ($4.5 \mu\text{m}$) in purple.

Table 2.4 summarizes the results of the MCMC analysis of the lightcurves, and it lists the final values and uncertainties for the transit depths, mid transit times and impact parameters from the final fits as well as the inclination and semi-major axis obtained from the first fits. We checked that the initial fits of the semi-major axis and the inclination are in agreement with the literature values before fixing them with Gaussian priors for the second fit. The survey as a whole was in statistical agreement with the literature values within $< 1\sigma$.

We also show the raw photometry with the best fit model for each visit in Appendix 2.A, and we show the corresponding RMS vs binsize plots in Appendix 2.A. Figure 2.13 shows the reduced, normalized and systematic corrected transit lightcurves for all planets in our

sample for both channel 1 and channel 2 with the best fit model resulting from the MCMC. We calculate the residuals, the χ^2 and the RMS of the residuals as sanity checks for each lightcurve (Table 2.10).

As mentioned in Section 2.3.1.3, before performing a complete MCMC analysis, we first check the fraction above photon noise and scale up the errors accordingly. Figure 2.5 displays a histogram of the fraction above photon noise for all analyzed lightcurves. The histograms have a median of 1.36 and 1.27 times photon noise for $3.6\text{ }\mu\text{m}$ and $4.5\text{ }\mu\text{m}$ respectively, which is typical for what has been achieved with Spitzer in the past (Ingalls et al. 2016).

2.4.1.2 Comparison to literature

Several of the planets from our survey have had their Spitzer lightcurves previously analyzed Sing et al. (e.g., 2016); Garhart et al. (e.g., 2020). We compare our results with those from Sing et al. (2016) and Garhart et al. (2020). Our measured transits are consistent within 3σ with those from the literature apart from a couple of outliers described below. Two of the largest outliers are the channel 2 transit depth of KELT-7b and the channel 1 transit depth of WASP-62b, both analyzed in Garhart et al. (2020) with PLD. We interpret the differences as due to the brightness of the host stars, and more specifically as due to the number of pixels selected for the pixel level decorrelation. These stars are bright and therefore 12 pixels are selected to model the systematics in Garhart et al. (2020) whereas we use 9 pixels uniformly for the entire survey (e.g., see Figure ??). We emphasize that these differences do not affect the general conclusion of the paper.

2.4.1.3 Transit depth ratio

We combine our results with transit measurements from the literature, which results in a survey of transit depths at 3.6 and $4.5\text{ }\mu\text{m}$ for 49 planets spanning a large range of equilibrium temperatures. We now compare all targets in our survey in a statistical manner. To do this, we opt to use a metric that is as free as possible from any assumptions - the normalized difference of the transit depths:

$$\bar{\Delta}_{tr} = \frac{(\delta_{ch2} - \delta_{ch1})}{\delta_{ch1}} \quad (2.3)$$

With this calculation, we tested for correlations with a number of other parameters: stellar parameters (Teff , $\log g$, Fe/H , R_s), orbital parameters (semi-major axis (AU), eccentricity, inclination) and planetary parameters (T_{eq} , $\log g$, R_p , M_p , scale height). We looked for correlations between using two statistical methods. First, we calculated the Pearson correlation coefficient (r) and its associated chance probability (p). Then, we fit a straight line using an orthogonal distance regression (ODR) to account for the errors on both the abscissa and ordinate values ? and look at the resulting residual variance of the fits.

Table 2.5: Correlations between parameters and the transit depth ratio. We show the Pearson correlation coefficient (r), the associated chance probability (p) and the residual variance from an ODR linear fit to the data.

Parameter	r	p	Res Var
T_{eq} (a=0)	-0.35	0.01	7.23
T_{eff}	-0.34	0.02	7.14
Stellar log(g)	0.13	0.36	6.98
[Fe/H]	-0.21	0.15	4.48
R_p	-0.26	0.07	8.11
Inclination	0.20	0.18	7.03
a (AU)	0.07	0.63	8.46
Planetary log(g)	0.01	0.92	8.47
M_p (M_J)	0.09	0.56	8.78
H (km)	-0.17	0.25	8.50
R_s (R_\odot)	-0.40	0.00	7.06
Radius Anomaly	-0.25	0.14	6.86

2.4.1.4 Searching for trends in the difference of transit depths

We analyse our Spitzer survey by looking at the normalized difference in the transit depths. Our normalized transit depth difference metric has the benefit that it does not include any additional assumptions on the composition of the atmosphere. Several studies look at the number of scale heights crossed at different wavelengths, including the strength of the water feature in the HST/ WFC3 bandpass (e.g., Sing et al. 2016). Including the scale height requires assuming the mean molecular weight, which includes errors from the surface gravity and equilibrium temperature. Furthermore, our metric is also independent of the stellar radius - unlike the difference in transit depths ($\delta_{ch2} - \delta_{ch1}$). Ultimately, this metric is a proxy for the ratio of the optical depths at these two wavelengths. We expect that the strength and magnitude of this metric can be used to test how the dominant expected atmospheric opacities change with the equilibrium temperature of the planets, see Section 2.5.1.

We search for any correlations that could be present between the calculated normalized transit depth difference and the physical parameters of the planetary systems that we are exploring. Table 2.5 summarizes the correlations for each of the parameters. The three parameters with the strongest Pearson correlation coefficients and the lowest chance probabilities are T_{eq} , T_{eff} and R_s . Both T_{eff} and R_s are incidentally included in the calculation of the equilibrium temperature, T_{eq} (in our case with zero albedo and full redistribution). We also observe that the weakest correlations are with the planetary mass, planetary radius, and semi-major axis. This is not surprising since our sample is highly biased towards hot Jupiters with a relatively small range of radii and masses, and with similarly close-in orbits. This means that the span of these parameters is small and therefore the uncertainties will be large and the correlations will not be obvious.

2.4.1.5 Transit depth versus equilibrium temperature

In Figure 2.6 (left panel), we plot the normalized transit depth difference ($(\delta_{ch2} - \delta_{ch1})/\delta_{ch1}$) against the equilibrium temperature for all planets in our sample. This plot contains 49 planets with masses 0.02 - 10.2 M_{Jup} , radii 0.24 - 1.9 R_{Jup} and equilibrium temperatures 550 - 2690 K. The color scale on the data points shows the scale height (H) of each planet, ($H = kT_{eq}/\mu g$) calculated assuming a hydrogen dominated atmosphere with mean molecular weight (μ) of 2.3, equilibrium temperature (T_{eq}) calculated with zero albedo and zero redistribution and planetary surface gravity (g) from the literature.

In Table 2.6 we show the weighted mean of the normalized transit depth difference and the corresponding number of scale heights for each temperature bin in Figure 2.6. We also calculate the weighted mean of the absolute value of the normalized transit depth difference and the number of scale heights.

We find that the weighted mean of the absolute value normalized transit depth difference and the number of scale heights to be significant to 8.0σ and 7.5σ respectively. This means that we are statistically detecting the atmosphere with a very high significance.

All 9 of the cool (<1000 K) planets lie on the positive side of the transit depth metric with a weighted mean transit depth of 0.029 ± 0.007 , 4.0σ from zero (gray assumption). We also find that the weighted mean transit depth difference and the number of scale heights of the 1000-2000 K planets and the >2000 K planets are not significant ($<3\sigma$). We therefore treat all planets >1000 K as one sample. These 36 hot planets have an absolute value weighted mean 0.3σ from zero (cloudy) assumption. In total, 14 of these planets are consistent with the cloudy models (zero) within 1σ . However, since these hot planets span both positive and negative values of the transit depth difference, it is unsurprising that their weighted mean transit depth is only marginally deviating from zero. The weighted mean of the absolute value of the difference in the transit depths for the hot planets is 0.025 ± 0.004 (5.9σ) and is more scattered than the cooler planets.

2.4.2 Results from the 1-D grid of model transmission spectra

2.4.2.1 General trends observed in the grids of models

In Figure 2.7 we show a selection of tracks from the complete grid of models and in Figure 2.8 we show each interpolated grid as a shaded region in comparison with the survey data. The fiducial model grid (1x solar and equilibrium chemistry, no vertical mixing $K_{zz} = 0$), plotted in Figure 2.7 shows the effect of increasing equilibrium temperatures on the transit depths, at ~ 900 K the model grid switches from a negative transit depth difference to a positive transit depth difference.

The interpolated grid shows a spread in the expected difference in the two transit depths. An important aspect of the model grid, which largely influences the spread is the surface gravity. Lower surface gravities result in larger scale heights and lead to a larger signal in the difference of the two Spitzer/IRAC transit depths. The surface gravity also changes the

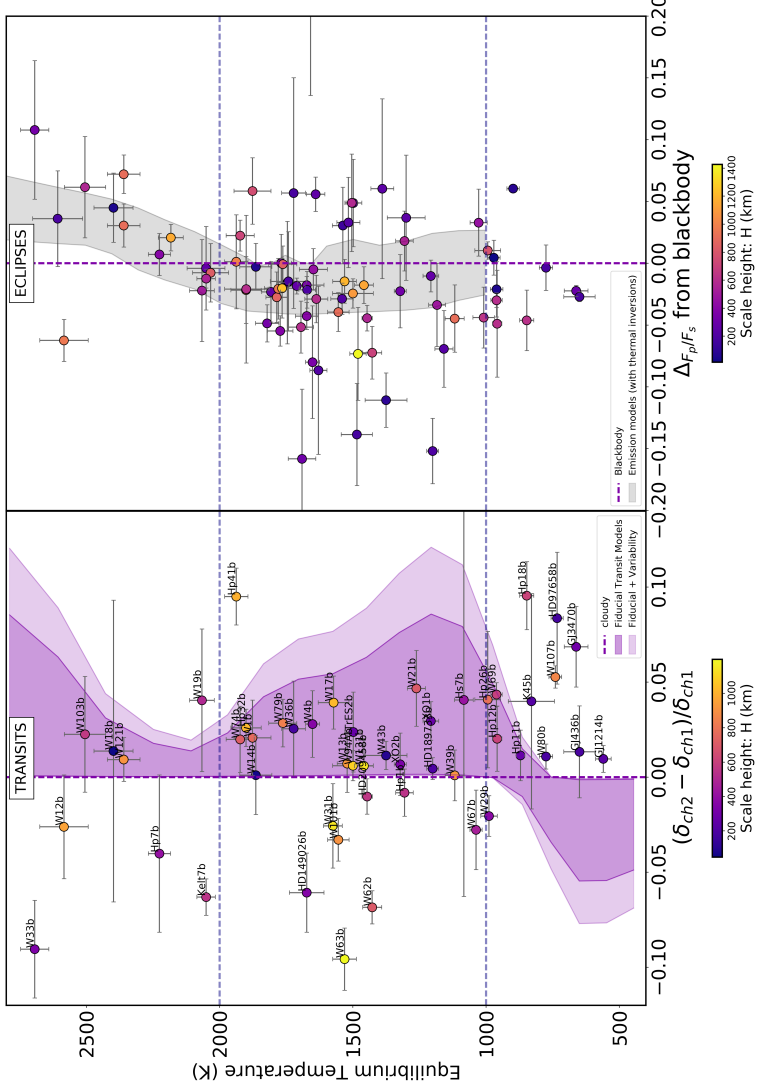


Fig. 2.6: Left panel: difference in transit depths between $4.5\ \mu\text{m}$ and $3.6\ \mu\text{m}$ normalized to the transit depth at $3.6\ \mu\text{m}$ plotted against equilibrium temperature, $1-\sigma$ uncertainties are shown in gray, color bar depicts the scale height in km. The shaded area on the left panel shows our grid of solar composition cloud-free equilibrium chemistry models, the extended lighter region is corrected for stellar variability. The dashed purple vertical line at zero is where planets with low pressure gray clouds would lie. Right panel: the deviation from the blackbody in emission against the equilibrium temperature, presented in Baxter et al. (2020). Color scale shows the scale height in km and the shaded region shows grid of models containing temperature inversions.

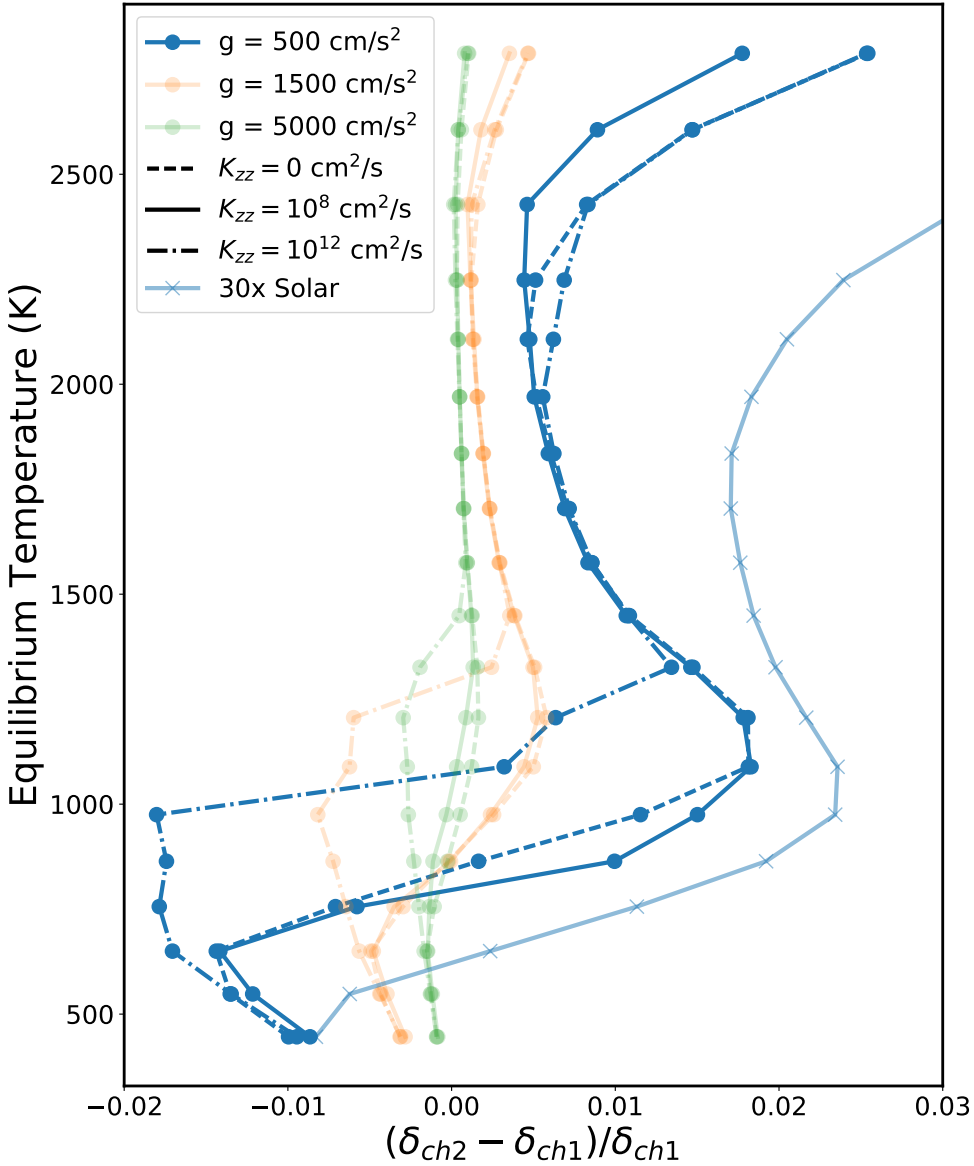


Fig. 2.7: Normalized Spitzer transit depth difference as a function of the equilibrium temperature for a selection of the grid tracks created with our atmospheric model framework described in Sections 2.3.2.3 and 2.3.2.4. We show a selection of grids with 1x solar composition and $R_p = 2R_J$. Different colors show different surface gravities: blue is $g = 500$, orange is $g = 1500$ and green is $g = 5000$. Different line styles show the effect of vertical mixing: solid line shows equilibrium chemistry, dashed is $K_{zz} = 10^8$ and dot-dashed is $K_{zz} = 10^{12}$. Lighter blue line with 'x' markers shows a 30x solar track with $R_p = 2R_J$, $g = 500$ and $K_{zz} = 0$.

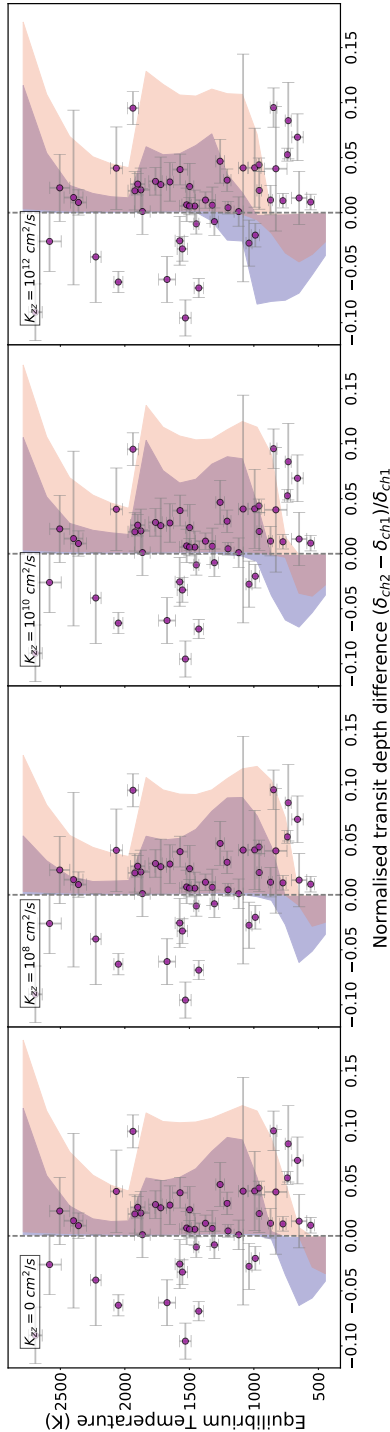


Fig. 2.8: Normalized Spitzer transit depth difference for the complete grids of transmission models created with our atmospheric model framework described in Sections 2.3.2.3 and 2.3.2.4. At each temperature we show the models where the surface gravity is representative of our survey, i.e. at $T_{\text{eq}} > 1800$ K we only plot $g = 1500$ and 5000 . Panels from left to right show equilibrium chemistry (no vertical mixing), $K_{zz} = 10^8$, $K_{zz} = 10^{10}$ and $K_{zz} = 10^{12}$. Blue translucent shaded region shows the 1x solar composition and orange translucent shaded region shows the 30x solar composition (overlap in purple). Gray dashed line represents a gray opacity source showing no spectral features. Planets from our sample are overplotted in purple circles with their 1σ errorbars.

Table 2.6: Weighted means of the normalized transit depth difference ($(\delta_{ch2} - \delta_{ch1})/\delta_{ch1}$), the absolute value of the normalized transit depth difference, the corresponding number of scale heights (NH), and its absolute value. This is shown for the different temperature ranges (<1000 K, 1000-2000 K, and >2000 K) presented in Figure 2.6. The intermediate columns labeled $N\sigma$ indicate the significance of the previous weighted mean and weighted error.

Planet Selection	$(\delta_{ch2} - \delta_{ch1})/\delta_{ch1}$	$N\sigma$	$ (\delta_{ch2} - \delta_{ch1})/\delta_{ch1} $	$N\sigma$
All planets	0.010 ± 0.005	1.9σ	0.028 ± 0.003	8.0σ
<1000 K	0.029 ± 0.007	4.0σ	0.032 ± 0.006	5.1σ
1000-2000 K	0.002 ± 0.006	0.3σ	0.023 ± 0.005	5.0σ
>2000 K	-0.032 ± 0.015	2.2σ	0.042 ± 0.010	4.1σ

Planet Selection	NH	$N\sigma$	$ NH $	$N\sigma$
All planets	0.2201 ± 0.0935	2.4σ	0.5032 ± 0.0669	7.5σ
<1000 K	0.4515 ± 0.1179	3.8σ	0.4900 ± 0.1043	4.7σ
1000-2000 K	0.0130 ± 0.1343	0.1σ	0.4840 ± 0.0968	5.0σ
>2000 K	-0.5907 ± 0.4271	1.4σ	0.9239 ± 0.3322	2.8σ

shape of the TP profile as seen in Figure 2.4. Figure 2.7 shows the effect of different surface gravities. We designed the model grid to span the parameters of the survey, notably with surface gravities of $g = 500, 1000, 1500$, and 5000 . However, the for ultra-hot model planets with low surface gravity of $g = 500$ the upper atmosphere exceeds the Hill radius. These models do not represent any planets in our survey since the hottest planets in our survey tend to have larger surface gravity ($g \sim 1000$), we therefore discard these model planets from Figure 2.8.

The effect of vertical mixing can be seen in Figure 2.7. A large amount of mixing results in the transition between CH4 to CO occurring at higher temperatures. Increasing the metallicity to 30x solar has the effect of lowering the temperature of the transition between negative and positive transit depth difference. Increased metallicity also results in a stronger positive signal for the hotter planets >1000 K.

2.4.2.2 Statistical comparison of planet atmospheres with model grid

We compare the data with the grids of models quantitatively by calculating the average number of standard deviations (based on the 1σ uncertainties) between each of the planets and their corresponding model grid point with the closest input parameters (T_{eq} , $\log(g_p)$, R_s and R_p). We then compute a weighted average for the whole grid, such that we can express the statistical significance of each grid with one number. We split this comparison into different temperature regimes based on the expected carbon chemistry. We compare the data to a transit depth difference of 0, representing a gray cloud opacity. Additionally, we also compare the data with the grids of models qualitatively by interpolating a shaded region between grid points, allowing us to visually compare the models with the Spitzer/IRAC transit depth difference e.g., see Figure 2.6.

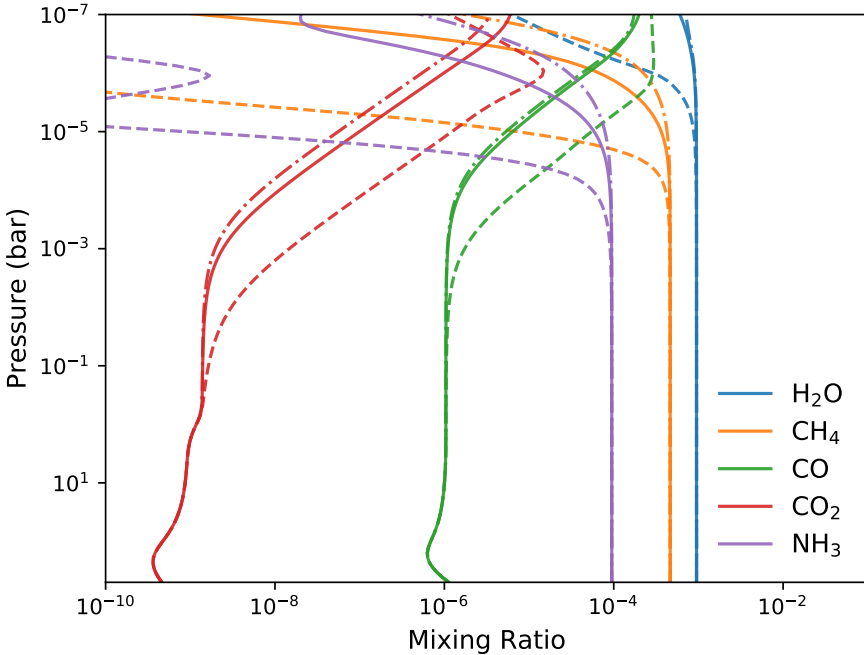


Fig. 2.9: Abundance mixing ratios at different pressures for the main species in the Spitzer bandpasses. The solid line shows the nominal situation ($a = 0.035$ AU, $T_{\text{eff}} = 3750\text{K}$) dashed line shows $a = 0.06$ AU, $T_{\text{eff}} = 4250\text{K}$, and the dashed-dotted line shows $a = 0.017$ AU, $T_{\text{eff}} = 4250\text{K}$.

In Section 2.3.2.1 we fix the orbital distance to 0.035 AU in our model grid creation. We do this because in our sample of planets the equilibrium temperature has a much larger correlation with the stellar effective temperature than with the semi-major axis. The range of semi-major axes in our sample spans ~ 0.017 to ~ 0.06 AU. We explore how much our choice of model parameterization (fixing the orbital distance to 0.035 AU) affects our results with the following two tests. We start by creating models with the minimum and maximum orbital distance of our sample, 0.017 and 0.06 AU.

In the first test, we match the equilibrium temperature by changing the effective temperature of the star. For a 650 K planet, an orbital distance of 0.017 AU corresponds to a stellar effective temperature of 3250 K and 0.06 AU corresponds to 4250 K. Figure 2.9 shows the effects on chemistry, where the star with higher T_{eff} provides greater flux even at larger orbit and leads to more photolysis. Nevertheless, it mainly impacts the main species at the lower pressures ($P < 1$ mbar). We find that the resulting difference in our transit depth metric for a planet placed at the minimum and maximum orbital distance is 0.0025. This is a factor of 10 smaller than the mean errorbar in our sample, so we do not expect this to change our results.

In the second test, we match the equilibrium temperature by changing the stellar radius. This time the resulting difference in our transit depth metric is 3.2e-6, which is three orders of magnitude smaller than the mean errorbar of our sample. Since the changes in the models are so small compared to the size of the uncertainties, we do not expect that the different orbital distances are the reason behind the scatter seen in Figure 2.6.

Figure 2.10 displays the results of the statistical comparison of each model grid with the planets in our survey. Each planet transit depth measurement is compared to the corresponding transmission model with the closest parameters (T_{eq} , $\log(g_p)$, R_s and R_p). We calculate the statistical significance for a set of planets, which is quantified by the average number of sigmas, for all eight grids of models. In the two panels of Figure 2.10 we show the results of the cool planets ($T_{\text{eq}} < 1000$ K), followed by the hot planets ($T_{\text{eq}} > 1000$ K). We find that the hot planets are best fit by 1x solar and high vertical mixing, $K_{zz} = 10^{12}$. We rule out high metallicity models for these planets to $\sim 3\sigma$ confidence.

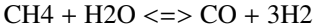
On the other hand, we find that the cool planets are best fit by 30x solar and a low amount of vertical mixing ($K_{zz} = 10^8$ or $K_{zz} = 0$). We find that the 1x solar composition and high amounts of vertical mixing ($K_{zz} = 10^{12}$) are ruled out with $> 3\sigma$ confidence for these cool planets.

We also find that the results of comparing the model grids to the full sample are that the full sample mimics the cool sample. This is because the different grids of models are divergent at the cool temperatures, so the results from the cool temperatures drive the statistical results for the full grid.

2.5 Discussion

2.5.1 Expected opacities at 3.6 and 4.5 μm

The features we see in the transmission spectra are a result of the underlying chemistry at the pressures probed by our observations. Figure 2.3 shows the abundance weighted opacities for the dominant opacity sources in the grid of models at the wavelengths of the Spitzer bandpasses. The dominating absorbing molecules in the Spitzer bandpasses are CH4 and H2O at 3.6 μm and CO, H2O and CO2 (for high metallicities) at 4.5 μm . Since H2O opacity is about equally present in both IRAC bandpasses, the two Spitzer transit depths can be used to understand the relative abundance of CO and CH4. The following summary chemical reaction plays an important role in determining the dominating carbon-bearing species in an atmosphere (e.g., Visscher et al. 2010; Moses et al. 2011; Visscher & Moses 2011; ?):



At temperatures higher than ~ 1100 K the forward reaction is favored (CO creation), for nominal pressures of ~ 1 bar, whereas at temperatures lower than ~ 1100 K the reverse reaction is favored (CH4 creation) (e.g. Madhusudhan 2012; Mollière et al. 2015; Molaverdikhani

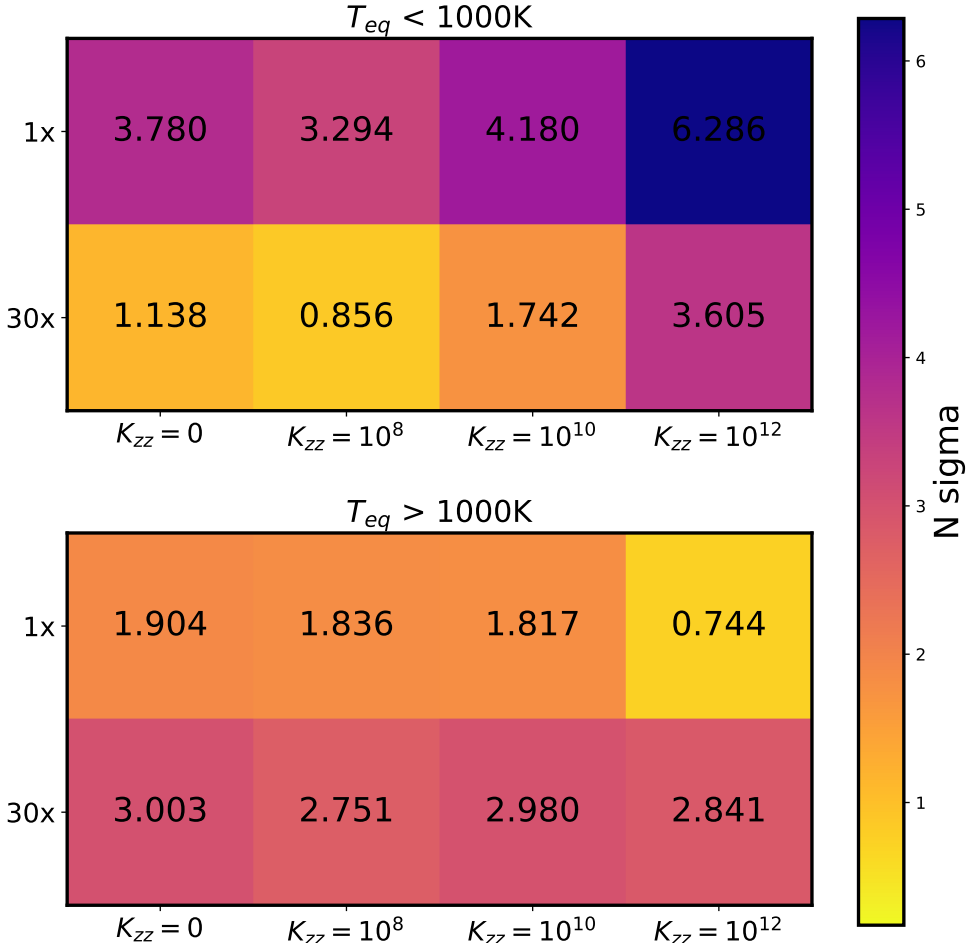


Fig. 2.10: Plot of the number of sigmas the data is from each model grid. We do this for eight grids and three sets/subsets of planets. The eight model grids are composed of two different metallicities (1x and 30x Solar) and four different vertical mixing scenarios ($K_{zz} = 0, 10^8, 10^{10}$ and 10^{12}). The color bar represents the average number of sigmas each model grid is from the set of data, a lower $N \sigma$ (blue) means a better fit. The top panel shows the results for the cool planets ($T_{eq} < 1000\text{ K}$) and the bottom panel shows the hot planets ($T_{eq} > 1000\text{ K}$). The number of sigmas are written on each cell.

et al. 2019). The gas transition between CH₄ and CO is plotted as a function of temperature on Figure 2.4, it shows where the abundance of CH₄ and CO are the same Visscher (2012). A temperature pressure profile crossing this line results in CO or CH₄ becoming the dominant absorber.

We thus expect that the atmospheres of planets in thermochemical equilibrium with temperatures above $\sim 1100\text{ K}$ have CO as the dominating carbon bearing species and the cooler atmospheres have CH₄. The result of this on the normalized difference of the transit depths

(Figure 2.6) is that the CH₄ planets would have a negative difference whereas CO planets have a positive difference. The transition from negative to positive transit depth differences seen in Figures 2.6, 2.7 and 2.8 shows the changing carbon chemistry (CH₄ to CO) with increasing equilibrium temperature. We find that the equilibrium temperature of the transition in the fiducial model grid (thermochemical equilibrium, 1x solar) is slightly lower than 1100 K presented in previous work (e.g., Madhusudhan 2012). We emphasize that the transition from CH₄ to CO depends on the temperature and pressure of the layer being probed with Spitzer/IRAC transmission photometry, and that this temperature is not necessarily at the planet's equilibrium temperature.

2.5.2 Discussion on Transit Survey

2.5.2.1 Comparing transit depths to fiducial model grid

Figure 2.6 shows the normalized difference of the two Spitzer transit depths with the fiducial grid of models. The fiducial models are calculated with opacities from thermochemical equilibrium and 1x solar composition. The sample of planets with temperatures hotter than 1000 K follow the fiducial models, however, we see that the cool planets appear to deviate from this model grid. Since we see that different chemical and physical processes are likely occurring at these different equilibrium temperatures we proceed by splitting Figure 2.6 into three temperature regimes based on the expected chemistry from our model grid: the cooler, methane planets (<1000 K), the hotter carbon monoxide hot planets (1000 K - 2000 K) and the few ultra-hot planets where molecular dissociation can occur ($T_{eq}>2000$ K).

There are 13 planets in our survey with $T_{eq} < 1000$ K. Our fiducial (1x solar and no vertical mixing) models demonstrate that the predicted carbon-bearing species for planets in this temperature regime is methane, which results in the models occupying the negative side of Figure 2.6. However, we find that the data show the opposite trend, all planets lie on the right side of Figure 2.6. We find that this equilibrium chemistry grid is ruled out at 3.8σ , which is statistically capturing the dearth of methane in the sample of coolest planets, see Section 2.4.2.2. This supports previous individual studies of cool gas giants with HST/WFC3 and it indicates that there are more complex physical processes happening not included in the fiducial models.

There are 28 planets in the mid-temperate/hot range (1000-2000 K) and 8 planets in the hot/ultra-hot range (>2000 K) of Figure 2.6. Of these 36 hot/ultra-hot planets, 14 of them are consistent to less than 1σ with the cloud-free solar composition model grid. In Section 2.4.2.2 we show that these planets are consistent with the fiducial model grid to 2σ . Additionally, we find that there is only 1 of these 36 hot/ultra-hot planets with a stronger positive signal than the fiducial model grid, meaning that a model grid with a higher CO abundance (e.g. 30x solar) is not required to explain our sample of observations. 30x solar is ruled out with 3σ confidence for the hotter planets.

There are several effects not included in the fiducial grid of models which contribute to

the statistical deviation. For example, we assume solar metallicity, no vertical mixing and cloud-free atmospheres. We compare the survey of planets to the model grids in a statistical manner and discuss the effects of each of these in detail below.

2.5.2.2 Effect of metallicity in hot Jupiter atmospheric spectra

The metallicity of a planet contributes to the atmospheric molecular abundances. Our fiducial model grid assumes 1x solar composition and solar metallicity. Increasing the metallicity would increase the amount of CO in the atmosphere (e.g., Venot et al. 2014). Figure 2.7 shows a 30x solar track and Figure 2.8 shows the whole interpolated grid (with no vertical mixing, see the first panel). Increasing the metallicity to 30x solar results in a lower temperature at which the model atmospheres transition between CH₄ and CO. This transition occurs at a temperature of around 600 K, much lower than the transition of 900 K for the fiducial grid.

In Section 2.4.2.2 we show that the cool planets lack the methane signature and are better fit with 30x solar composition models, with a significance of $>2.5\sigma$. This is the case for the lower values of vertical mixing ($K_{zz} = 0, 10^8$ and 10^{10}), discussed in more detail in Section 2.5.2.3. These cool planets are also generally lower mass planets because of the detection biases for these systems, see Figure 2.1. Lower mass planets typically have higher metallicities Fortney et al. (2013); Welbanks et al. (2019). Therefore, a higher average metallicity in the 13 planets with temperatures <1000 K likely explains the lack of methane. Our findings support the predicted high metal enrichment in cool gas giants presented in Espinoza et al. (2017). They predict C/O ratios for a sample of 50 gas giants with $T_{eq} < 1000$ K, 6 of our 13 planets in this temperature range are also in their sample. Furthermore, our finding of high metallicity for these coolest warm giant planets supports the individual high metallicity measurements of several planets in the literature: HAT-P-12b (Line et al. 2013), HAT-P-26b (Wakeford et al. 2017), GJ 436b (Morley et al. 2017) and HAT-P-11b (Mansfield et al. 2018). All of these exoplanet atmospheres are found to have super-solar metallicities, except for GJ 3470b which is suggested to have a relatively low atmospheric metallicity for its planet mass (Benneke et al. 2019).

On the other hand, the planets with equilibrium temperatures >1000 K are consistent with the 1x solar composition models to less than 2σ for all values of K_{zz} . The higher metallicity grid is less favored for these planets (2.6σ deviation). Similar to the high abundance of CO at cooler temperatures, the high metallicity model grid shows stronger CO features throughout the entire temperature range, which is not favored by the planets in our survey. We do not find it necessary to statistically invoke high metallicity to explain the near-infrared spectral features of hot Jupiters.

Figure 2.3 shows the opacities for the 1x and 30x metallicity used in the creation of our model grids. In practice, differences in the opacities for the two cases would also affect the temperature pressure profile, however, in our analysis we do not compute the temperature pressure profiles self consistently. Nevertheless, we can predict what effect this might have. Higher metallicities would result in hotter temperatures in our TP profiles, which would in

turn result in a larger CO/CH₄ ratio. This means that we could explain the dearth of methane with less extreme enhancements in the metallicity of the models.

2.5.2.3 Vertical mixing and non-equilibrium effects

Another aspect not included in our fiducial model grid is the presence of non-equilibrium effects such as photochemistry, advection, convection, and turbulence in the atmosphere. To capture some of these non-equilibrium atmospheric processes, we introduce an eddy diffusion coefficient, K_{zz} , into our modeling (see Section 2.3.2.3). Theory suggests that for hot Jupiters K_{zz} can range from 10^8 to 10^{12} based on the estimation from the mean vertical wind in GCMs (Moses et al. 2011). We create four different grids of models spanning the range of eddy diffusion coefficients: equilibrium chemistry, $K_{zz} = 10^8$, $K_{zz} = 10^{10}$ and $K_{zz} = 10^{12}$.

The model incorporating different K_{zz} show that the transition between CH₄ and CO being the dominating carbon bearer in these atmospheres occurs at higher temperatures for larger values of K_{zz} . This is because with larger values of K_{zz} , the mixing penetrates deeper into the atmosphere and can therefore dredge up methane to the observable pressures of hotter planets where methane is not expected. The models on Figure 2.8 (right panel) demonstrate that $K_{zz} = 10^{12}$ can dredge up CH₄ for planets up to 1300 K.

For the cool planet data ($T < 1000$ K), we find that the models containing low amounts of vertical mixing are significantly favored over high vertical mixing for both metallicities. For 30x solar metallicity, the low mixing $K_{zz} = 10^8$ fits marginally better than equilibrium chemistry ($K_{zz} = 0$) and is a 3σ better fit than the high vertical mixing ($K_{zz} = 10^{12}$). On the other hand, for the hot planets we find that $K_{zz} = 10^{12}$ is favored over the lower mixing or no mixing for both the 1x and 30x solar metallicities.

Komacek et al. (2019) showed that for tidally locked hot Jupiters, vertical mixing increases with increasing equilibrium temperature and rotation rates: starting at $K_{zz} = 10^7 - 10^8$ for the coolest (500 K) planets and going to $K_{zz} = 10^{11} - 10^{12}$ for the hottest (1500-3000 K). We find that the cool planets support these results, with a vertical mixing of $K_{zz} = 10^8$ favored by the data. However, the hotter planets seem to suggest a lower level of mixing than theory predicts, our models with $K_{zz} = 10^{10}$ are marginally supported over the equilibrium and $K_{zz} = 10^8$ grids, which is lower than the theoretical maximum of $K_{zz} = 10^{12}$. These findings are in line with the findings of Miles et al. (2020) for non-equilibrium processes in brown dwarfs. They found warmer brown dwarfs showed lower mixing than theory predicts, yet the cooler objects were close to the theoretical maximum.

Additionally, our non-equilibrium chemistry models include the effects of photochemical reactions. For hot planets ($T_{eq} > 1000$ K), CO is only dissociated in the upper atmosphere due to its strong bond, which has negligible influence on the Spitzer bandpasses. For cooler planets ($T_{eq} \leq 1000$ K), CH₄ is dissociated by atomic hydrogen produced by photolysis. This destruction of CH₄ can penetrate down to around 0.1 mbar with lower mixing ($K_{zz} = 10^8$). Yet the competing effects of mixing can overtake and efficiently transport methane to the upper atmosphere. HCN is also produced by photochemistry and can reach abundances close

to CH₄ in some cases. Nevertheless, HCN absorbs similarly at the two IRAC wavelengths, so we do not expect that it would have significant effects on the normalized transit depth difference.

Since vertical mixing is responsible for dredging CH₄ to the hotter planets, and not CO in the cooler planets, we conclude that the dearth of methane is not due to strong atmospheric mixing, it is likely due to the higher metallicity of these atmospheres. Another possible factor affecting the lack of methane signatures in the cool planets could be the amount of interior heating, see Fortney et al. (e.g., 2020). We find that several of the coolest planets are eccentric (see Table 2.7, which could cause some tidal heating. Our temperature pressure profile calculation assumes an interior heating of $T_{\text{int}} = 150$ K. However, substantial interior heating, $T_{\text{int}} > 300$ K, could result in pushing the deeper layers of these atmospheric TP profiles towards the CO regime (Morley et al. 2017; Benneke et al. 2019; Thorngren et al. 2019, 2020). If the interior is more CO dominated, then vertical mixing could dredge up CO in the cooler planets, resulting in a dearth of methane (e.g., Moses et al. 2013). We did not test this as it is beyond the scope of our paper.

2.5.2.4 Effects of clouds on the cool and hot Jupiter atmospheric spectra

Clouds are ubiquitous in transiting exoplanet atmospheres (Sing et al. 2016). There are several mechanisms responsible for producing homogeneous and inhomogeneous clouds on tidally locked planets (Parmentier et al. 2013, 2021; Helling et al. 2016; ?, 2019). An example can be found in Line & Parmentier (2016) in which HD 189733b and HAT-P-11b can be explained by patchy clouds without the need to invoke global clouds or high mean molecular weight atmospheres.

Hazes are expected to be prominent in the cooler atmospheres. Morley et al. (2015) predicted that a transition between haze-free and hazy atmospheres will occur at 800-1100 K, implying that any planet below this temperature might show no molecular features. Gao et al. (2020) showed that the amplitude of the HST/WFC3 water feature on planets with temperatures < 900 K is such that these atmospheres become dominated by haze formation. However, (Kawashima & Ikoma 2019) predict that molecular features such as CO and CH₄ are still detectable in the infrared for their sample of warm Jupiters (< 1000 K) with hazy atmospheres.

Furthermore, if all planets with temperatures < 1000 K in our survey were characterized by a gray cloud opacity, then we would expect the the transit depth difference to be evenly distributed around zero in Figure 2.6. However, these 13 planets have a mean transit depth of 0.026 ± 0.008 . This rules out a gray cloud (flat spectrum) at 4.0σ confidence for all planets. Suggesting that these planets cannot be characterized by a gray cloud opacity, and that there is a molecular feature.

Molaverdikhani et al. (2020) suggested that clouds could play a role in the heating of the atmosphere, resulting in a lack of CH₄. However, such clouds would also dampen the CO feature significantly. This effect could be the reason for the few planets consistent with zero,

but we do not expect that this effect explains the 4.0σ detection for the sample of cool planets (<1000 K).

There are 14 planets with equilibrium temperature >1000 K that have transit depth differences consistent with zero (flat spectrum). The weighted mean transit depth difference of all these planets is -0.002 ± 0.006 , only 0.3σ . However, the weighted mean of the absolute value of the transit depth difference is 0.025 ± 0.004 (5.9σ).

Based on the prediction by Morley et al. (2015) we would not expect to have hazes at these temperatures. However, Gao et al. (2020) show that the HST water feature is damped when compared to a cloud-free atmosphere, and they find the data is better fit by their models containing silicate clouds. Furthermore, (Line & Parmentier 2016) suggested that patchy cloud cover can mimic the spectral features of a high mean molecular weight atmosphere, resulting in a flatter transmission spectrum. Additionally, due to the varying temperature across the day and night sides of tidally locked highly irradiated hot Jupiters, clouds and hazes may behave differently at the east and west terminators of the planet (Kempton et al. 2017). Such that photochemically generated hazes formed on the day side can be blown over to the nightside and dampen the transmission features. We therefore expect that clouds do play a role in dampening the spectral features in some of our planets, namely, those in the temperature region predicted to be cloudy by Gao et al. (2020) (>1000 K).

However, since there is still a strong signal in the absolute value of the transit depths of these planets (5.9σ), there is indication that the population cannot be captured by a completely featureless model. Mie scattering theory results in a drop off in cloud opacity at $2\text{-}3 \mu\text{m}$ (e.g., Benneke et al. 2019), since we are detecting molecular features between $3\text{-}5 \mu\text{m}$ it may be that any possible cloud particles could exhibit Mie scattering in this regime. Including Mie scattering as a cloud prescription in our transmission spectrum forward modeling is beyond the scope of this paper. However, since the cloud opacity would be lower at $4.5 \mu\text{m}$ than it is at $3.6 \mu\text{m}$, it would result in a negative transit depth metric, similar to the expected methane signature. However, we do not find planets with a negative transit depth metric, and hence find no evidence for Mie scattering clouds.

2.5.2.5 Outliers and the effect of nightsides

According to our grids of models, we do not expect any of the planets above 1400 K to have CH₄ as the dominating carbon bearing species in any of the metallicity or mixing scenarios. However, there are two hot planets which are significantly on the left: HD149026b and WASP-33b (2.9σ and 3.5σ from zero respectively). HD 149026b has previously been discrepant from models, for example, ? found that they needed 30x solar metallicity to reproduce the Spitzer 3.6 and $4.5 \mu\text{m}$ phase curves. Furthermore, the biggest outlier, WASP-33 b, is a planet that is orbiting a δ Scuti star, with pulsating periods close to the transit duration (Herrero et al. 2011). Both of these planets indicate that there may be additional factors that could significantly affect the transit light curves, however, statistically it is not unexpected to have a couple of outliers. In Section 2.5.2.7 we discuss how we treat stellar variability for the

whole survey.

Additionally, three of the seven hottest planets above 2000 K (WASP-33b, WASP-121b, and WASP-18b) have evidence of a temperature inversion (von Essen et al. 2015; Haynes et al. 2015; Evans et al. 2017; Arcangeli et al. 2018). However, since transmission spectroscopy is not as sensitive to the temperature profile at low resolution (e.g., Brown 2001) so we do not expect to see the effect of temperature inversions in the transit depth difference of the two Spitzer/IRAC bandpasses. Additionally, the H- opacity seen at the WFC3 bandpass (e.g. Arcangeli et al. 2018) does not become important at the Spitzer/IRAC bandpasses until equilibrium temperatures as high as 3500 K.

2.5.2.6 Radius Anomaly

Our sample subsequently spans a very large range of scale heights, ranging from HAT-P-2b with a scale height of 26 km to WASP-31b with a scale height of 1150 km. Figure 2.6 demonstrates that there is no trend with the atmospheric scale height and the strength of the spectral features indicated by the magnitude of the transit depth metric. Furthermore, the radius anomaly is thought to correlate with incident flux, with hotter planets having a more inflated radius (Thorngren & Fortney 2018). However, we do not find a trend with the radius anomaly and the strength of the spectral features seen with Spitzer (see Figure 2.17).

2.5.2.7 Stellar Variability

Contamination of the transmission spectrum from starspots, faculae and flares generate brightness temperature differences between the disk-integrated spectra of the star and the region occulted by a transiting planet (Désert et al. 2011b; Pont et al. 2008; Sing et al. 2011). If a planet occults a star spot at a different temperature to the photospheric one, it can change the shape of the lightcurve by appearing as a change in the flux during transit. On the other hand, if the star spot is not occulted, then the disk integrated spectrum of the star is fainter or brighter, depending on the spot properties, which can cause the measured transit depth to be different than the nominal one. Stellar variability can occur when star spots rotate in and out of view of the integrated stellar disk, which depends on the rotation period of the star.

To estimate the possible effect of stellar variability on our results, we aim to provide a quantitative estimate of how this would affect the sample as a whole, by expanding the interpolated model grid. We do this by looking at a worst case scenario variable star, HD 189733, which has a peak-to-peak variability of $\sim 3\%$ in the visible (Henry & Winn 2008). We follow the method in Désert et al. (2011b); Sing et al. (2011) and Berta et al. (2012) to calculate the effect of this variability on the transit depth metric. We first translate this 3% in V-band to 0.8% at $3.6 \mu\text{m}$ using the ratio of blackbodies, we set 2.8% spot coverage with spots at 1000 K less than the stellar photosphere. We can propagate this to a relative error on the transit depth and assuming it will affect $4.5 \mu\text{m}$ as much as $3.6 \mu\text{m}$ (in reality it will be a smaller effect), we can then propagate this to an error on the transit depth metric ($\delta_{ch2} - \delta_{ch1}/\delta_{ch1}$). This leads to a 42% maximum error on the transit depth metric, we thus

extend the models positive and negative by this percentage, which is plotted on Figure 2.6.

Despite choosing the worst case scenario to expand our model grid, the features arising from the changing chemistry with equilibrium temperature can still be clearly distinguished in the grid of models in Figure 2.6, i.e. the transition regions at ~ 1000 K and ~ 2200 K remain clear. The relative size of the variability region is on average one-third of the size of the average uncertainty on the data points. Nevertheless, this is a conservative upper estimate and will not apply as strongly to all planets in our sample, since not all stars are as variable as HD 189733. If the temperature difference between spot and photosphere is less or if the spot covering fraction is smaller, then this would result in a lower variability amplitude and smaller effect on the transmission spectrum. Additionally, 3% is the maximum peak-to-peak variability, this would only apply if the observations were taken at the peak and trough of the variability period. Since we designed the observations to have as few orbital periods as possible to be within one variability period of the star, it is unlikely that we reach the maximum variability between our two Spitzer observations.

2.5.3 Comparing Transmission and Emission with warm Spitzer/IRAC

Several of the planets from our survey have published secondary eclipse measurements. We utilize the secondary eclipse literature survey from Baxter et al. (2020) (and references therein) which contains 3.6 μm and 4.5 μm eclipses for 78 planets in total. Several of the eclipse depths presented in Table 1 of Baxter et al. (2020) were taken from Garhart et al. (2020), and some of these planets had dilution corrections due to companions in the field of view. The dilution corrections were applied before any analysis in Baxter et al. (2020), but this was not reported in their Table 1. We have thus reported the eclipse depths with dilution corrections in Table 2.8 of this work using the dilution correction factors presented in Table 4 of Garhart et al. (2020). We use the eclipse depth, equilibrium temperature, brightness temperatures at 3.6 μm and 4.5 μm and the deviation from the blackbody presented in Baxter et al. (2020). The deviation from the blackbody probes the temperature pressure profile. A positive deviation is either methane in absorption at 3.6 μm with a nominal TP profile or CO in emission at 4.5 μm if the TP profile is inverted. Twenty-four of the planets in (Baxter et al. 2020) are also in our transmission survey, which allows us to statistically compare the two samples. To better understand the dearth of methane planets presented in Section 2.4.2.2, we compare the difference in brightness temperature from emission with the normalized difference in transit depths for planets with both emission and transmission observations. Additionally, we create a color-magnitude plot and compare the emission to the brown dwarf spectral sequence with a focus on the coolest planets.

2.5.3.1 Probing different pressures with emission and transmission

In Baxter et al. (2020), we demonstrate that the relative opacities in the two Spitzer/IRAC bandpasses can act as a probe of the atmospheric temperature structure when observing the

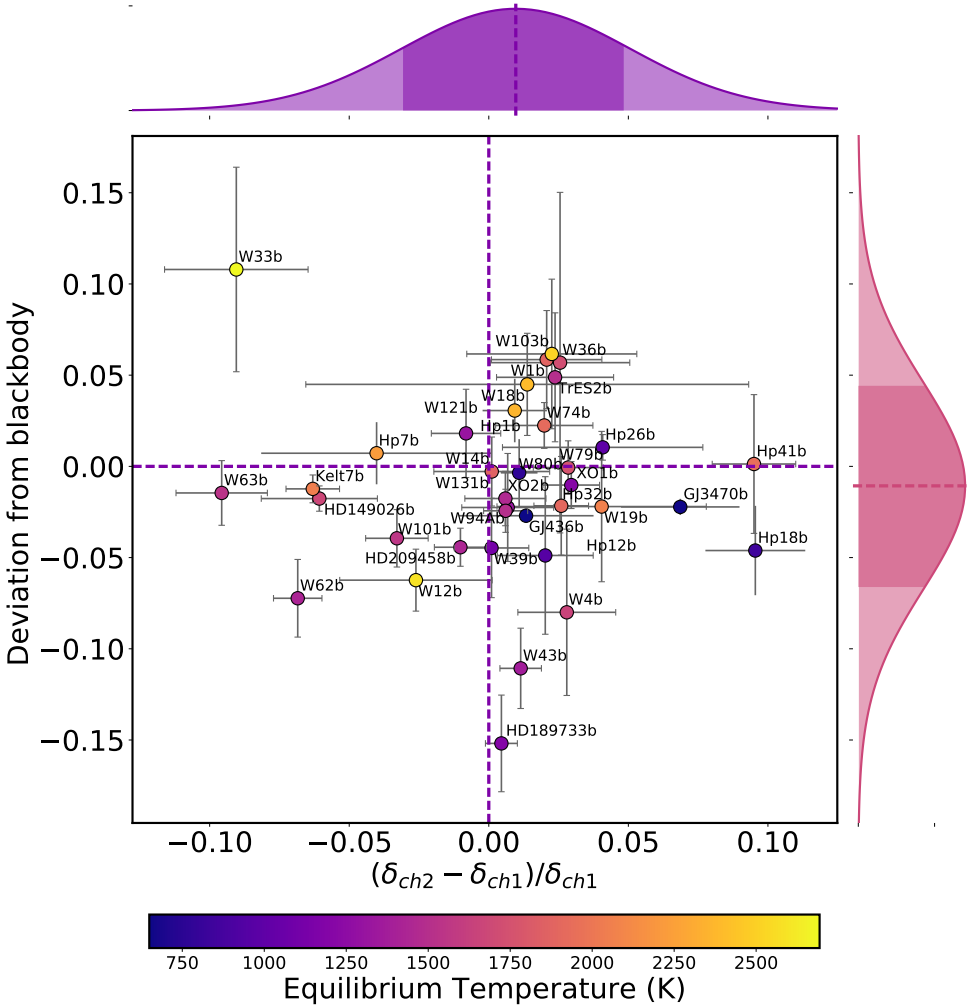


Fig. 2.11: Deviation from a blackbody calculated from emission against the normalized difference in the transit depth presented in Figure 2.6. Histograms on each axis show the mean and standard deviation of each axis. The equilibrium temperature of each planet is shown with the color scale.

dayside emission. The deviation from blackbody metric described in Baxter et al. (2020) plotted against the equilibrium temperature shows that ultra-hot Jupiters have statistical evidence for thermal inversion. In a non-inverted atmosphere, a positive deviation indicates that the $3.6\text{ }\mu\text{m}$ brightness temperature is lower than that at $4.5\text{ }\mu\text{m}$ due to methane absorption at $3.6\text{ }\mu\text{m}$ and a negative deviation indicates that the $4.5\text{ }\mu\text{m}$ T_b is lower due to CO absorption at $4.5\text{ }\mu\text{m}$. On the other hand, if the atmosphere is inverted, CO being the dominating carbon bearing species in the atmosphere would result in a positive deviation due to seeing CO in

emission at $4.5\ \mu\text{m}$. In this work we are focusing on the CH4 to CO transition temperature and thus we do not account for temperature inversions.

In Figure 2.11 we compare the difference of the two IRAC brightness temperatures against the normalized difference in the transit depth. There appear to be no trends in the emission and transmission of the planets in our survey with both eclipses and transits, and we also find that the top left quadrant is almost empty, with the main outlier being WASP-33b. Given that the deviation from the blackbody can be positive or negative for a CO dominated atmosphere depending on the TP profile, we test for trends in the planets with equilibrium temperatures below 1800 K, which are not expected to have thermally inversions in their atmospheres. We find that the top left quadrant, which indicates CH4 in transmission and CH4 in emission, is empty. Meaning that any planets which show signs of methane in either emission or transmission do not show it in the other. For example, HD 149026b lies in the bottom left quadrant, it has a negative deviation from a blackbody, which indicates a CO absorption feature in emission (assuming a non-inverted TP profile). The expected corresponding transmission spectrum would predict a positive transit depth difference. However, this is not what we see. Possible reasons for these differences include: longitudinal abundance differences, more complex atmospheric processes such as atmospheric mixing, different cloud composition/abundances at different layers in the atmosphere, or changes in the thermal structure between emission and transmission (e.g., Fortney 2005). Additionally, similar to the results for the planets in transmission, we do not find a correlation between the deviation of the blackbody and the radius anomaly.

2.5.3.2 Comparing to brown dwarfs with a Color-Magnitude diagram

We create also a color-magnitude plot using these Spitzer secondary eclipses. Our work expands on that presented in Triaud (2014) by extending their survey from 37 planets to the 78 planets presented in Baxter et al. (2020) and by using the newly released GAIA dr2 for more accurate distances (Gaia Collaboration et al. 2018). We calculate the planetary apparent magnitudes by using the apparent stellar magnitudes from the WISE spacecraft (Cutri & et al. 2012) in combination with the planet to star flux ratio from Spitzer. The two WISE channels W1 and W2 are known to overlap the two remaining Spitzer channels (Kirkpatrick et al. 2011). We then use the GAIA dr2 distances which were calculated using a Bayesian prior from Gaia Collaboration et al. (2018) and Bailer-Jones et al. (2018) to calculate the planetary absolute magnitudes. The equilibrium temperature, GAIA distances, and WISE magnitudes used are tabulated in Table 2.8. Errors are propagated fully throughout the calculation from the errors on all input properties.

Figure 2.12 shows the [3.6] - [4.5] color vs [3.6] magnitude diagram, we have over-plotted the survey of brown dwarfs spanning M, L, and T spectral classes from Dupuy & Liu (2012) for comparison. The planets plotted on Figure 2.12 show an increasing scatter with increasing $3.6\ \mu\text{m}$ magnitude. This is unlike the brown dwarf spectral sequence which follows the a very tight L/T transition. This increase in scatter confirms the one seen in Beatty et al. (2014);

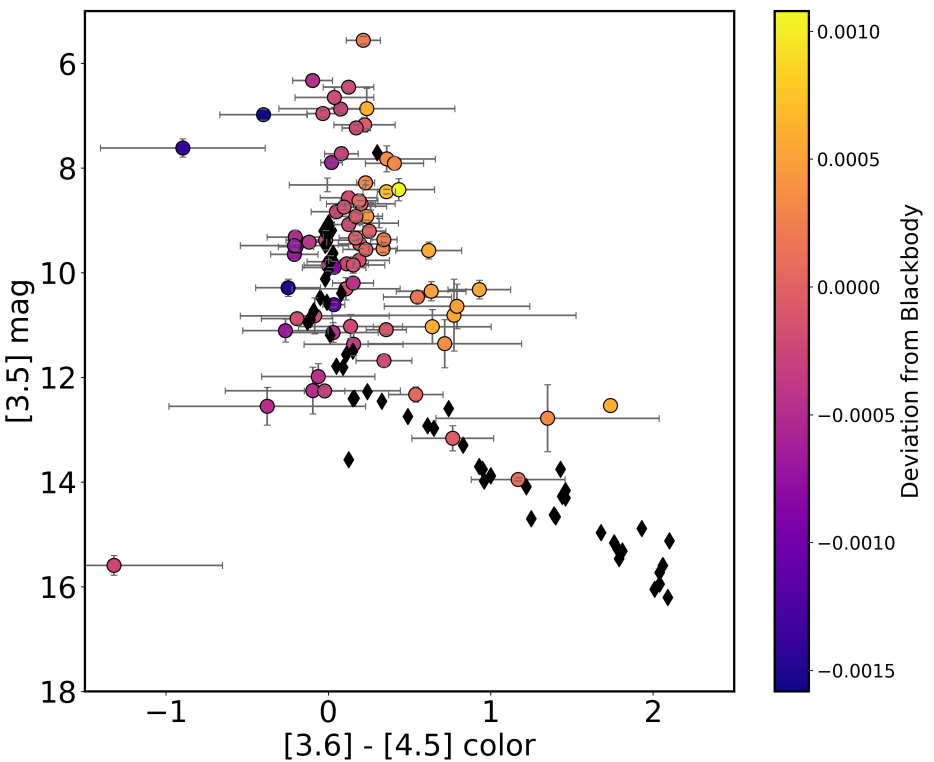


Fig. 2.12: $[3.6] - [4.5]$ color vs $[3.6]$ magnitude diagram of exoplanets and brown dwarfs planets with available eclipse depth measurements in the two warm Spitzer band-passes. Brown dwarf colors (estimated from the WISE catalog) are shown as black diamonds from Dupuy & Liu (2012). The color scale is the deviation from a blackbody metric described Baxter et al. (2020).

Melville et al. (2020) and Dransfield & Triaud (2020), which is suggested to be due to an increase in atmospheric diversity.

Figure 2.12 shows that the increase in scatter is driven by a small family of planets which lie redder than the brown dwarf spectral sequence. The color scale shows that this family of planets shows a positive deviation from a blackbody (Baxter et al. 2020). The positive deviation from a blackbody indicates methane absorption (nominal TP profile) or CO emission (inverted TP profile). Since these planets are around 1200–1500 K, we do not expect their atmospheres to be inverted, and we therefore think that these warmer planets could be displaying a signature of methane in their atmospheres. In Section 2.4.1.5 we show that the cooler planets (< 1000 K) deviate from equilibrium chemistry models by not showing signatures of methane in their atmospheres. Similarly, these warmer planets are not expected to have a high methane abundance given equilibrium chemistry, we again have to invoke non-equilibrium

processes such as vertical mixing. Warmer planets are expected to have larger vertical mixing than their cooler counterparts (Komacek et al. 2019), creating an ideal scenario for dredging up methane. Furthermore, brown dwarfs are expected to have smaller mixing than gas giant planets, with K_{zz} ranging from $10^4 - 10^{8.5}$ for brown dwarfs and $10^7 - 10^{12}$ (Zahnle & Marley 2014; Leggett et al. 2017; Miles et al. 2020). Although this prediction is based on non-irradiated, higher gravity objects with mostly convective atmospheres, GCMs of highly irradiated, radiative atmospheres of hot Jupiters do display stronger mixing (Parmentier et al. 2013; Komacek et al. 2019). We therefore propose that the increased atmospheric diversity of planets compared to their brown dwarf counterparts seen in Figure 2.12 could be due, in part, to the diversity of processes involved, such as the presence of vertical mixing.

Furthermore, brown dwarfs are expected to have smaller mixing than gas-giant planets (Zahnle & Marley 2014). Although this prediction is based on non-irradiated, higher gravity objects with mostly convective atmospheres, GCMs of highly irradiated, essentially radiative atmospheres of hot Jupiters do display stronger mixing (Parmentier et al. 2013; Komacek et al. 2019). With K_{zz} ranging from $10^4 - 10^{8.5}$ for brown dwarfs (Zahnle & Marley 2014; Leggett et al. 2017; Miles et al. 2020) and $10^7 - 10^{12}$ for gas giants (Parmentier et al. 2013; Komacek et al. 2019). We therefore propose that the increased atmospheric diversity of planets compared to their brown dwarf counterparts seen in Figure 2.12 could be due, in part, to the diversity of processes involved, such as the presence of vertical mixing.

2.6 Conclusion

We have performed the data analysis of 70 lightcurves and presented in total 49 planets with transit depths at 3.6 and $4.5 \mu\text{m}$ with Spitzer/IRAC. This survey represents the largest analysis of Spitzer/IRAC observations of gas giant transits to date, and it spans equilibrium temperatures from 500 K to 2700 K. We have implemented our custom Spitzer/IRAC data analysis pipeline which thoroughly searches over a grid of data reduction parameters before employing pixel level decorrelation (Deming et al. 2015) to correct for the strong Spitzer systematics and extract the transit depths using an MCMC transit fitting algorithm.

We then statistically studied the sample of all planets with transmission in these two band-passes. We create a fiducial cloud-free 1-D atmospheric model grid with 1x solar composition and equilibrium chemistry spanning the parameters of the planets in our sample. We compare the survey of planets with this model grid and note a family of outliers with equilibrium temperature < 1000 K, they do not show the expected methane abundance from these equilibrium chemistry models.

Next, we expand our grid in two dimensions by extending to 30x solar metallicity and incorporating non-equilibrium effects with different values of an eddy diffusion co-efficient (K_{zz}). We find that the best fitting grid for the cool planets ($T < 1000$ K) has high metallicity (30x solar) and low or no vertical mixing ($K_{zz} = 0$ or 10^8). On the other hand, we find that the hot planets ($T > 1000$ K) are best explained with 1x solar composition with a marginal better

fit with the high vertical mixing model ($K_{zz} = 10^{12}$). We conclude that the cool planets are better fit by models with higher metallicity as due to an observational bias resulting in lower masses. We find evidence supporting non-equilibrium chemistry in a survey of planets and find that our work agrees with the theory that hotter planets have higher vertical mixing.

Furthermore, we combine our transits with our previous literature eclipse survey. We do not find any trend between eclipses and transits, and propose that this is due to several effects: clouds at different pressures or more complex atmospheric processes. We then create a color magnitude diagram using the emission observations and compare to L/T transition brown dwarfs. With a larger sample size than previous studies, we also see the increase in scatter with increasing magnitude first seen in Triaud (2014). We see that the increase in scatter is driven by a family of mid-temperate planets showing a methane signature, which is not expected from equilibrium chemistry. We propose that this increase in scatter is due to methane being dredged up due to high levels of vertical mixing in the atmosphere. Which supports the theory that brown dwarfs have $\sim 100x$ lower levels of vertical mixing than planets.

2.A Pipeline results Figures and Tables

Table 2.7: Jump Parameters used as starting points for the MCMC analysis. Eccentricity was fixed to 0 for all planets since it did not affect the resulting transit depths. Stellar parameters (T_{eff} , $\log(g_*)$ and $[\text{Fe}/\text{H}]$) are used to calculate linear limb-darkening parameters.

Planet	a/R_s	inc °	R_p/R_s	Period days	Eccentricity	T_{eff} Kelvin	$\log(g_*)$ $\log_{10}(\text{cm/s}^2)$	$[\text{Fe}/\text{H}]$ dex	Ref
HAT-P-32 b	6.05(4)	88.9(4)	0.1508(4)	2.150008(1)	0.16(6)	6207(88)	4.33(1)	-0.04(8)	13
XO-1 b	11.24(9)	88.8(2)	0.1320(5)	3.94150685(91)	0	5750(75)	4.50(1)	0.02(8)	6
HAT-P-1 b	9.85(7)	85.63(06)	0.1180(2)	4.46529976(55)	0	5980(49)	4.36(1)	0.13(1)	19
WASP-17 b	7.05(7)	86.83(68)	0.13	3.7354380(68)	0.03(2)	6650(80)	4.16(3)	-0.19(9)	1
WASP-39 b	11.37(24)	87.75(27)	0.1457(16)	4.0552765(35)	0	5400(150)	4.4(2)	-0.12(10)	18,10
HAT-P-12 b	11.77(21)	89.0(4)	0.1406(13)	3.2130598(21)	0.03(3)	4650(60)	4.61(1)	-0.29(5)	11
HAT-P-18 b	16.04(75)	88.8(3)	0.1365(15)	5.508023(6)	0.08(5)	4803(80)	4.57(4)	0.10(08)	14
TrES2 b	7.90(2)	83.87(02)	0.1254(5)	2.47061317(9)	0.02(2)	5850(50)	4.43(2)	-0.15(10)	9,22
WASP-4 b	5.46(2)	88.52(39)	0.1544(2)	1.33823204(16)	0.003(7)	5436(34)	4.46(5)	-0.05(4)	15,20
XO-2 b	8.18(3)	88.9(7)	0.1	2.615857(50)	0	5340(32)	4.48(5)	0.45(2)	5
GJ3470 b	13.94(49)	88.88(72)	0.0764(4)	3.3366487(43)	0.02(2)	3652(50)	4.78(12)	0.17(6)	3
WASP-21 b	9.62(17)	87.12(24)	0.1030(8)	4.3225126(22)	0	5800(100)	4.2(1)	-0.46(11)	21,4
WASP-31 b	8.00(19)	84.41(22)	0.127	3.4059096(50)	0	6302(102)	4.31(2)	-0.20(09)	2
WASP-1 b	5.69(6)	90.0(1.3)	0.1036(8)	2.5199454(5)	0.01(3)	6200(200)	4.3(3)	0.1(2)	17,7
HAT-P-26 b	13.44(83)	88.6(9)	0.0737(12)	4.234516(15)	0.12(6)	5079(88)	4.56(6)	-0.04(8)	12
WASP-107 b	18.2(1)	89.56(08)	0.1446(2)	5.72149242(46)	0	4330(120)	4.5(1)	0.02(10)	23
WASP-13 b	7.58(15)	85.64(24)	0.0922(8)	4.353011(13)	0	5826(100)	4.04(20)	0.0(2)	24,25
WASP-121 b	3.75(3)	87.6(6)	0.1245(5)	1.27492550(25)	0	6459(140)	4.24(1)	0.13(9)	26
WASP-69 b	11.96(17)	86.71(20)	0.1336(16)	3.8681382(17)	0	4700(50)	4.54(2)	0.15(8)	35
WASP-67 b	13.42(13)	85.8(3)	0.1345(48)	4.61442(1)	0	5417(85)	4.53(2)	0.18(6)	36
HATS7 b	10.59(51)	87.92(75)	0.0711(19)	3.185315(5)	0	4985(50)	4.54(5)	0.25(8)	37
WASP-29 b	12.15(44)	88.8(7)	0.101(2)	3.922719(7)	0.03(5)	4875(65)	4.54(4)	0.11(14)	38
HAT-P-41 b	5.45(18)	87.7(1.0)	0.1028(16)	2.694050(4)	0	6390(100)	4.14(2)	0.21(10)	32

Table 2.7: continued.

Planet	a/R_s	inc °	R_p/R_s	Period days	Eccentricity	T_{eff} Kelvin	$\log(g_*)$ $\log_{10}(cm/s^2)$	[Fe/H] dex	Ref
WASP-101 b	8.45(30)	85.0(2)	0.1140(9)	3.585720(4)	0	6380(120)	4.31(8)	0.20(12)	32
WASP-131 b	8.53(9)	85.0(3)	0.0815(7)	5.3222023(5)	0	6030(90)	4.09(3)	-0.18(8)	39
WASP-36 b	5.85(6)	83.15(13)	0.1368(6)	1.53736596(24)	0	5959(134)	4.49(1)	-0.26(10)	40
WASP-63 b	6.59(30)	87.8(1.3)	0.0781(11)	4.378080(6)	0	5550(100)	4.01(3)	0.08(7)	32
WASP-79 b	7.03(36)	85.4(6)	0.1049(24)	3.662380(5)	0	6600(100)	4.20(15)	0.03(1)	32
WASP-94 Ab	7.3(7)	88.7(7)	0.1094(8)	3.9501907(44)	0	6153(75)	4.18(1)	0.26(15)	41
WASP-74 b	4.86(20)	79.81(24)	0.0964(7)	2.137750(1)	0	5990(110)	4.39(7)	0.03(10)	33
WASP-62 b	9.55(41)	88.30(75)	0.1095(9)	4.411950(3)	0	6230(80)	4.45(10)	0.04(6)	34
Kepler-45 b	10.6(1.0)	87.0(7)	0.179(2)	2.455239(4)	0.11(10)	3820(90)	3.1(1)	0.13(13)	16

- (1) Anderson et al. (2011b); (2) Anderson et al. (2011a); (3) Biddle et al. (2014); (4) Bouchy et al. (2010); (5) Burke et al. (2007); (6) Burke et al. (2010); (7) Collier Cameron et al. (2007); (8) Doyle et al. (2011); (9) Esteves et al. (2015); (10) Faedi et al. (2011); (11) Hartman et al. (2009); (12) Hartman et al. (2011b); (13) Hartman et al. (2011a); (14) Hartman et al. (2011c); (15) Hoyer et al. (2013); (16) Johnson et al. (2012); (17) Maciejewski et al. (2014); (18) Maciejewski et al. (2016); (19) Nikolov et al. (2014); (20) Petrucci et al. (2013); (21) Seeliger et al. (2015); (22) Sorzetti et al. (2007); (23) Močnik et al. (2017); (24) Barros et al. (2012); (25) Skillen et al. (2009); (26) Delrez et al. (2016); (27) Holman et al. (2010); (28) Torres et al. (2011); (32) Stassun et al. (2017); (33) Stassun et al. (2018); (34) Stassun et al. (2019); (35) Anderson et al. (2014); (36) Hellier et al. (2012); (37) Bakos et al. (2015); (38) Hellier et al. (2010); (39) Hellier et al. (2017); (40) Mancini et al. (2016); (41) Neveu-VanMalle et al. (2014).

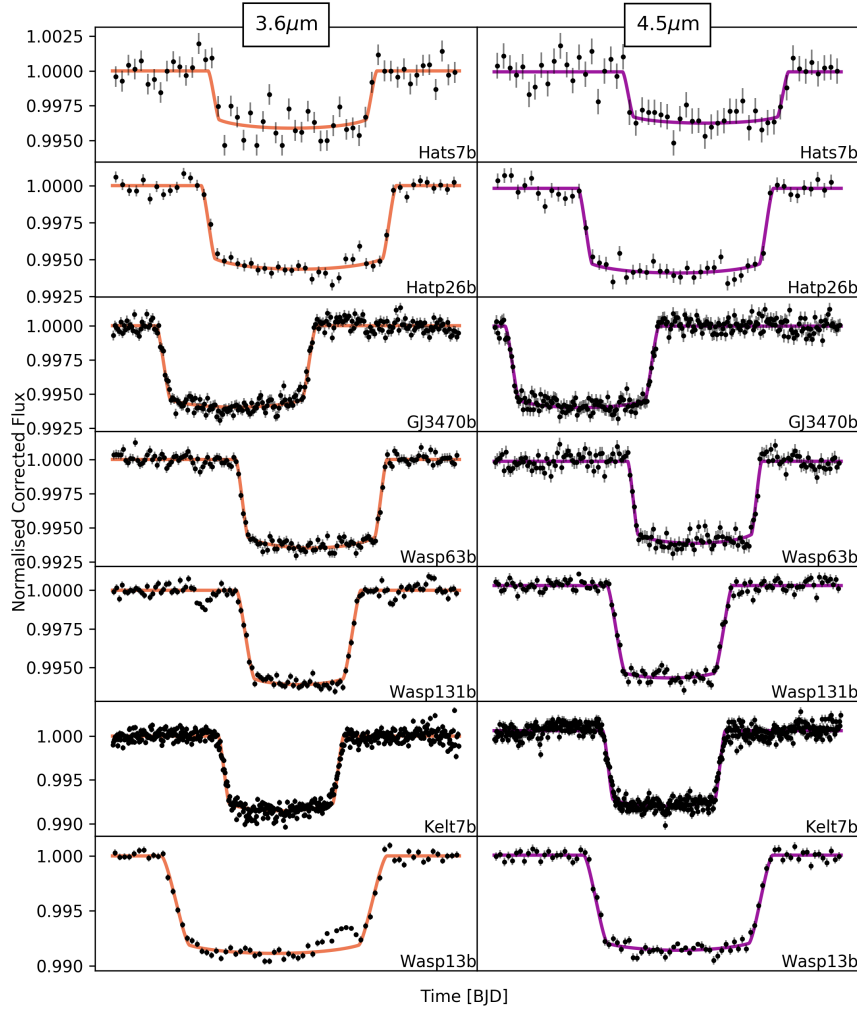


Fig. 2.13: Normalized and systematic corrected transit lightcurves for each planet at 3.6 (left column, orange) and $4.5\mu\text{m}$ (right column, purple). 1σ errorbars are those originally calculated from scaled photon noise. The data and the errorbars are binned in 5 minute intervals for display purposes. Continuous curves show the best fit transit models in each band-pass for comparison. Kepler-45b displays the result of 4 phase folded lightcurves in each channel.

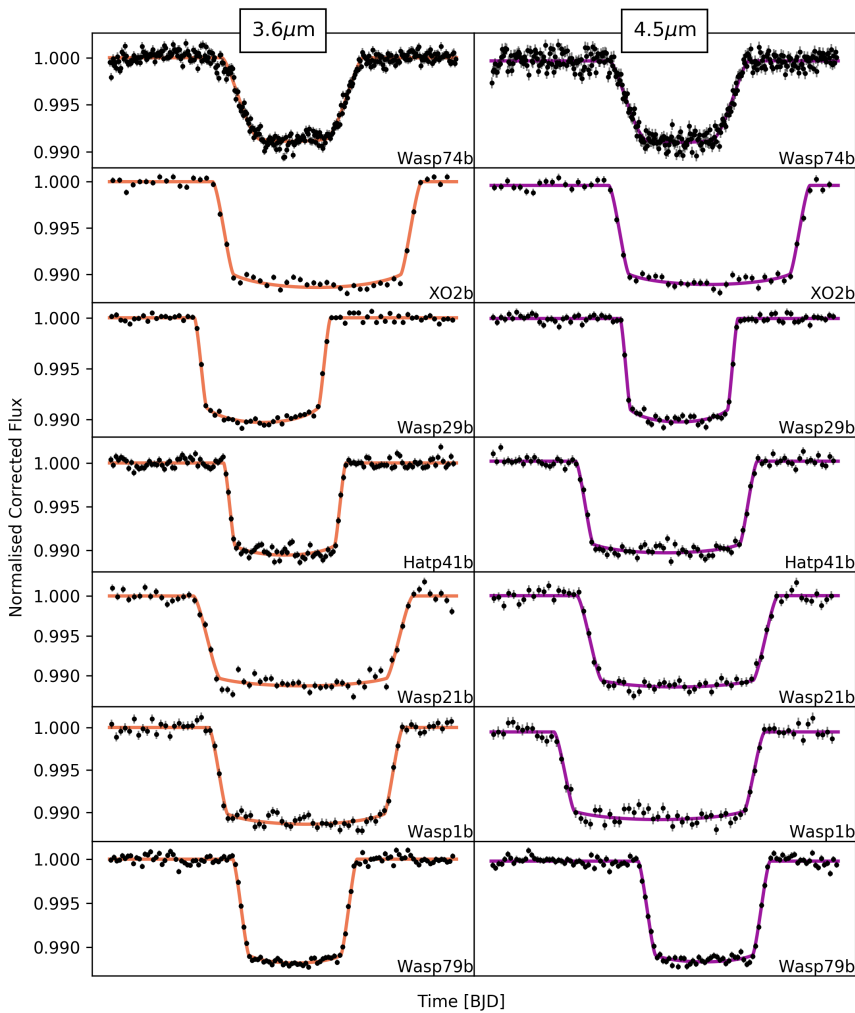


Fig. 2.13

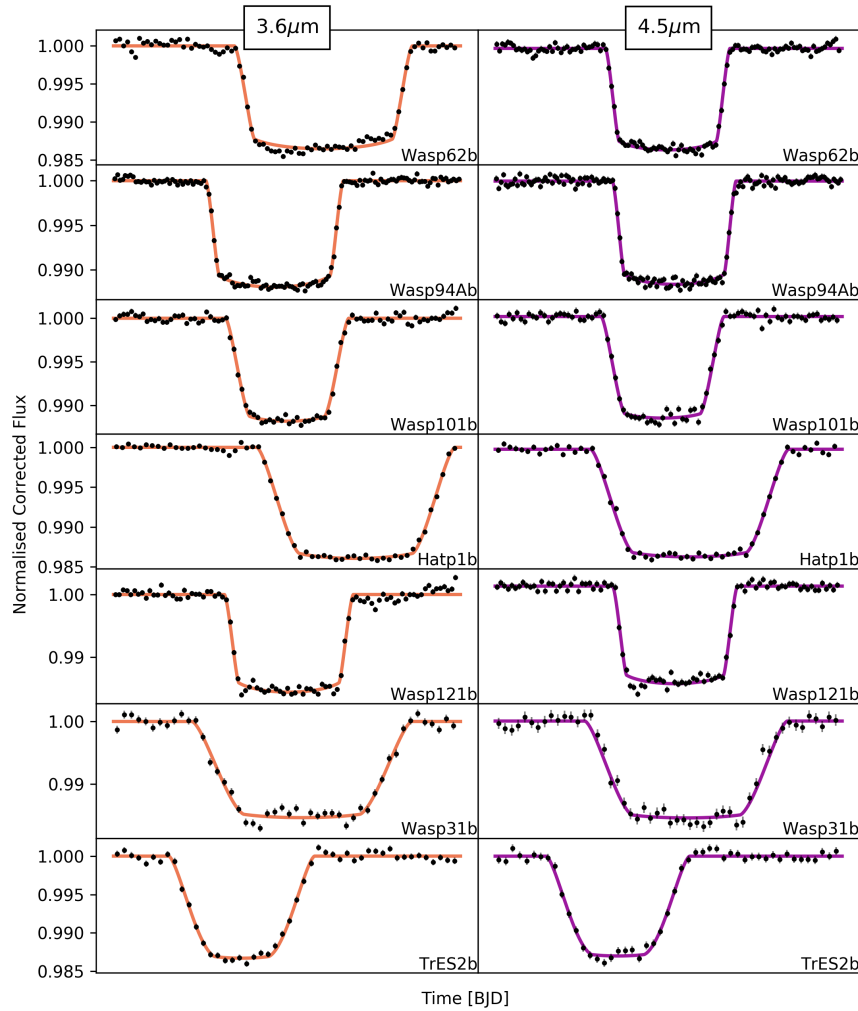


Fig. 2.13: *Continued.*

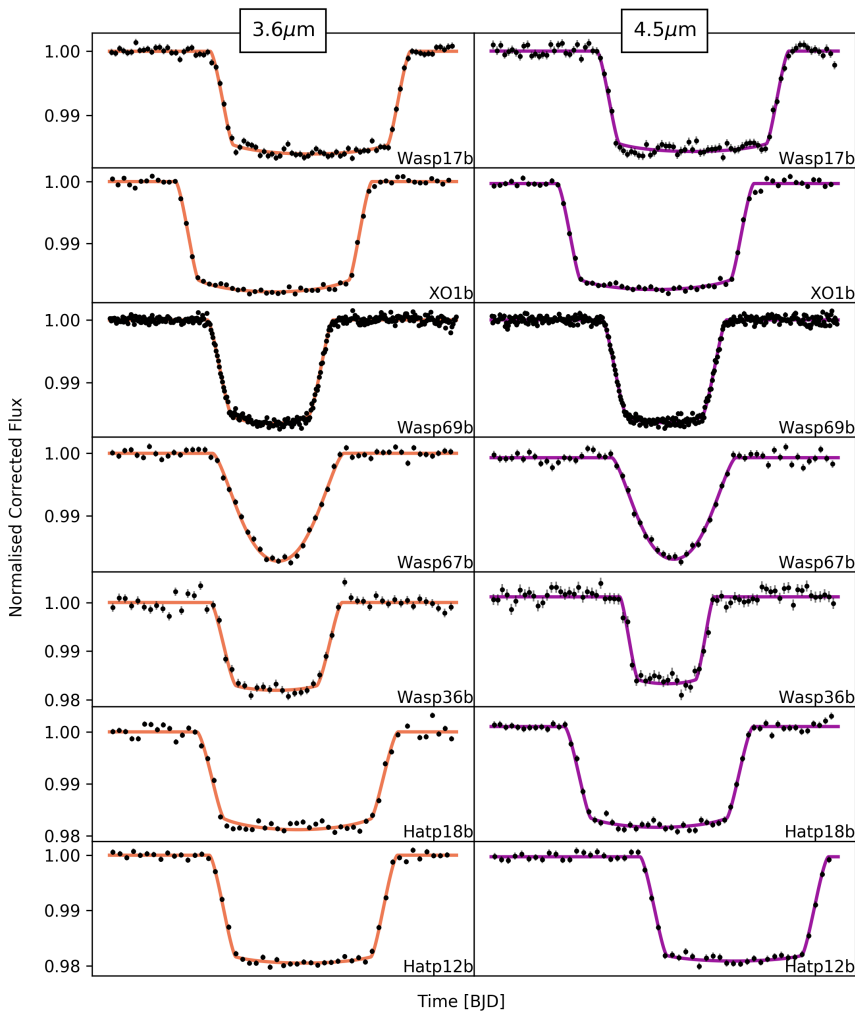


Fig. 2.13: *Continued.*

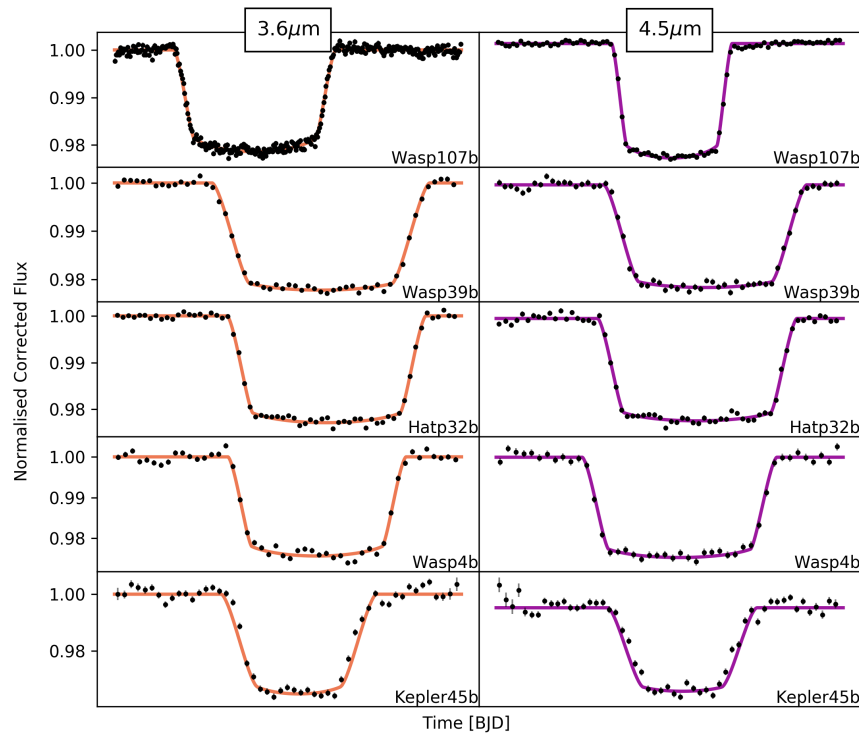


Fig. 2.13: *Continued.*

Table 2.8: Eclipse depths at 3.6 and 4.5 μm collected from the literature ($(F_p/F_s)_{3.6}$ and $(F_p/F_s)_{4.5}$ respectively). T_{eq} is the equilibrium temperature assuming no redistribution and 0 albedo. Distance is the estimated distance in parsec taken from Bailer-Jones et al. (2018). m_{W1}^s and m_{W2}^s are the stellar apparent magnitudes, $M_{3.6}^{pl}$ and $M_{4.5}^{pl}$ and the planetary absolute magnitudes in the wise 1 and wise 2 bandpasses (which are equivalent to the spitzer channel 1 and channel 2 respectively), calculated using the planet to star flux ratio. Color is the 4.5 minus 3.6 micron magnitude color of the planets. The final column details the reference for each of the eclipse depths in the literature, the majority of which were collected from exoplanets.org (Wright et al. 2011) and have been individually verified.

Planet	$(F_p/F_s)_{3.6}$	$(F_p/F_s)_{4.5}$	T_{eq} (a=0)	Distance	$M_{3.6}^{pl}$	$M_{4.5}^{pl}$	m_{W1}^s	m_{W2}^s	color	Ref.
ppm	ppm	Kelvin	parsec	mag	mag	mag	mag	mag		
HAT-P-32 b	3640±160	4380±200	1901±57	289.2±5.3	8.7±0.1	8.5±0.07	9.9±0.02	9.91±0.02	0.2±0.09	1
XO-1 b	860±70	1220±90	1207±30	163.6±0.6	11.1±0.1	10.73±0.08	9.49±0.02	9.52±0.02	0.36±0.12	2
HAT-P-1 b	800±80	1350±220	1306±33	159.0±1.0	10.5±0.1	9.92±0.18	8.73±0.02	8.75±0.02	0.55±0.21	3
WASP-39 b	880±150	960±180	1118±35	214.0±1.7	11.1±0.2	11.12±0.21	10.16±0.02	10.22±0.02	0.03±0.28	4
HAT-P-12 b	660±270	640±180	958±18	142.8±0.5	12.3±0.4	12.35±0.31	10.08±0.02	10.14±0.02	-0.1±0.54	5
HAT-P-18 b	437±145	326±146	847±26	161.4±0.6	12.6±0.4	12.93±0.49	10.2±0.02	10.25±0.02	-0.38±0.61	6
TrES2 b	1270±210	2300±240	1498±32	215.3±1.0	10.4±0.2	9.72±0.12	9.78±0.02	9.79±0.02	0.63±0.21	7
WASP-4 b	3190±310	3430±270	1651±27	267.2±3.7	9.8±0.1	9.78±0.09	10.68±0.02	10.75±0.02	0.01±0.15	8
XO-2 b	810±170	980±200	1322±23	154.3±1.4	11.0±0.2	10.89±0.22	9.24±0.02	9.31±0.02	0.14±0.32	9
GJ3470 b	113±24	3±22	662±45	29.4±0.1	15.3±0.2	19.25±7.96	7.81±0.03	7.78±0.02	-3.92±7.97	10
WASP-1 b	1170±160	2120±210	1876±69	393.1±10.5	9.6±0.2	8.96±0.12	10.22±0.02	10.25±0.02	0.62±0.2	11
HAT-P-26 b	85±0	265±70	994±48	141.8±1.1	14.0±0.0	12.78±0.29	9.54±0.02	9.6±0.02	1.17±0.29	6
WASP-121 b	3685±114	4684±121	2359±61	269.9±1.6	8.3±0.0	8.05±0.04	9.36±0.02	9.39±0.02	0.23±0.06	12
WASP-87 b	2080±127	2708±137	2343±68	298.4±3.6	8.7±0.1	8.47±0.06	9.4±0.02	9.43±0.02	0.26±0.1	12
WASP-100 b	1267±98	1720±119	2200±171	364.4±2.7	9.1±0.1	8.74±0.08	9.62±0.02	9.64±0.02	0.31±0.12	12
WASP-78 b	2001±218	2013±351	1957±256	754.3±16.7	8.3±0.1	8.33±0.2	10.96±0.02	10.98±0.02	-0.01±0.24	12
HAT-P-41 b	1842±319	2303±177	1937±44	348.2±4.5	8.7±0.2	8.49±0.09	9.56±0.02	9.6±0.02	0.2±0.21	12
WASP-101 b	1161±111	1194±113	1554±40	201.2±1.1	9.9±0.1	9.86±0.11	9.04±0.02	9.07±0.02	0.0±0.15	12
WASP-131 b	304±96	289±80	1458±35	200.1±2.6	10.8±0.3	10.91±0.3	8.54±0.02	8.57±0.02	-0.08±0.46	12
WASP-36 b	914±578	1953±544	1722±45	386.3±5.2	10.8±0.7	10.04±0.3	11.15±0.02	11.2±0.02	0.77±0.75	12
WASP-63 b	486±96	560±130	1531±45	290.7±2.0	10.3±0.2	10.2±0.25	9.34±0.02	9.39±0.02	0.11±0.33	12

Table 2.8: continued.

Planet	$(F_p/F_s)_{3.6}$	$(F_p/F_s)_{4.5}$	T_{eq} (a=0)	Distance	$M_{3.6}^{pl}$	$M_{4.5}^{pl}$	m_{W1}^s	m_{W2}^s	color	Ref.
	ppm	ppm	Kelvin	parsc	mag	mag	mag	mag	mag	
WASP-94 A b	867±59	995±93	1500±76	211.2±2.5	9.8±0.1	9.72±0.11	8.8±0.02	8.84±0.02	0.11±0.13	12
WASP-62 b	1616±146	1359±130	1427±35	175.6±0.6	9.7±0.1	9.86±0.11	8.9±0.02	8.92±0.02	-0.21±0.15	12
CoRoT-1 b	4150±420	4820±420	1900±81	787.9±23.5	8.6±0.1	8.45±0.12	12.1±0.02	12.14±0.02	0.12±0.17	13
CoRoT-2 b	3550±200	5000±200	1537±40	213.3±2.5	9.5±0.1	9.21±0.05	10.06±0.02	10.1±0.02	0.34±0.09	13
GJ 436 b	155±22	34±20	649±59	9.8±0.0	15.6±0.2	16.92±0.64	6.02±0.11	5.69±0.05	-1.32±0.67	14
HAT-P-19 b	620±140	620±140	1009±40	202.1±1.5	12.0±0.2	12.05±0.25	10.5±0.02	10.56±0.02	-0.06±0.35	4
HAT-P-2 b	996±72	1031±61	1540±30	127.8±0.4	9.5±0.1	9.52±0.07	7.57±0.02	7.58±0.02	0.03±0.11	15
HAT-P-20 b	615±82	1096±77	971±24	71.0±0.2	12.3±0.1	11.79±0.08	8.56±0.03	8.65±0.02	0.54±0.17	16
HAT-P-23 b	2480±190	3090±260	2051±71	364.8±4.7	9.5±0.1	9.26±0.1	10.75±0.02	10.79±0.02	0.19±0.13	17
HAT-P-26 b	-27±50	223±81	994±48	141.8±1.1	-±2.0	12.97±0.4	9.54±0.02	9.6±0.02	-±2.05	6
HAT-P-3 b	1120±225	940±125	1158±34	134.6±0.5	11.1±0.2	11.37±0.15	9.38±0.02	9.45±0.02	-0.26±0.26	5
HAT-P-4 b	1420±160	1220±130	1694±47	320.5±2.8	9.3±0.1	9.52±0.12	9.73±0.02	9.77±0.02	-0.2±0.17	5
HAT-P-6 b	1170±80	1060±60	1673±42	275.4±3.6	9.4±0.1	9.54±0.07	9.29±0.02	9.3±0.02	-0.12±0.11	18
HAT-P-7 b	1560±130	1900±110	2225±41	341.1±2.4	8.6±0.1	8.44±0.07	9.28±0.02	9.3±0.02	0.19±0.12	19
HAT-P-8 b	1310±85	1110±75	1772±48	211.6±1.7	9.5±0.1	9.71±0.08	8.93±0.02	8.95±0.02	-0.2±0.11	18
HD 149026 b	400±30	340±60	1673±65	75.9±0.2	10.9±0.1	11.07±0.19	6.79±0.07	6.8±0.02	-0.19±0.22	20
HD 189733 b	2560±140	2140±200	1200±22	19.8±0.0	10.3±0.2	10.54±0.11	5.29±0.15	5.34±0.05	-0.25±0.2	21
HD 209458 b	1190±70	1230±60	1446±19	48.3±0.1	10.2±0.1	10.05±0.06	6.31±0.09	6.19±0.03	0.15±0.13	22
Kepler-12 b	1370±200	1160±310	1481±31	88.1±9.7	9.5±0.2	9.69±0.29	12.05±0.02	12.08±0.02	-0.21±0.33	23
Kepler-17 b	2500±300	3100±350	1745±39	720.8±10.3	9.8±0.1	9.58±0.13	12.55±0.02	12.59±0.02	0.19±0.19	24
Kepler-5 b	1030±170	1070±150	1807±35	899.8±16.5	9.4±0.2	9.4±0.16	11.68±0.02	11.74±0.02	-0.02±0.24	25
Kepler-6 b	690±270	1510±190	1504±21	587.0±5.0	10.6±0.4	9.85±0.14	11.58±0.02	11.64±0.02	0.79±0.45	26
KOI-13 b	1560±310	2220±230	2607±94	519.1±29.1	7.8±0.2	7.47±0.17	9.39±0.02	9.41±0.02	0.36±0.3	27
Qatar-1 b	1511±455	2907±415	1389±43	185.6±0.8	11.0±0.3	10.39±0.16	10.32±0.02	10.4±0.02	0.64±0.36	28

Table 2.8: continued.

Planet	$(F_p/F_s)_{3.6}$	$(F_p/F_s)_{4.5}$	T_{eq} (a=0)	Distance	$M_{3.6}^{pl}$	$M_{4.5}^{pl}$	m_{W1}^s	m_{W2}^s	color	Ref.
	ppm	ppm	Kelvin	parsec	mag	mag	mag	mag	mag	
TrES-3 b	3460±350	3720±540	1629±32	231.3±1.3	9.9±0.1	9.86±0.16	10.57±0.02	10.61±0.02	0.04±0.2	29
TrES-4 b	1370±110	1480±160	1785±41	516.0±6.9	8.8±0.1	8.79±0.12	10.24±0.02	10.28±0.02	0.05±0.15	30
WASP-10 b	1000±110	1460±160	960±24	141.0±0.7	11.7±0.1	11.34±0.12	9.93±0.02	10.0±0.02	0.34±0.17	4
WASP-103 b	4458±383	5686±138	2505±78	883.3±153.1	6.9±0.4	6.63±0.38	10.72±0.02	10.75±0.02	0.24±0.54	31
WASP-12 b	4210±110	4280±120	2584±91	427.2±6.0	7.9±0.0	7.88±0.05	10.11±0.02	10.11±0.02	0.02±0.07	32
WASP-121 b	3150±103	4510±107	2359±61	269.9±1.6	8.5±0.0	8.1±0.03	9.36±0.02	9.39±0.02	0.36±0.06	12
WASP-14 b	1870±70	2240±180	1864±60	162.0±0.8	9.3±0.0	9.17±0.09	8.57±0.02	8.6±0.02	0.17±0.1	33
WASP-18 b	3000±200	3900±200	2398±73	123.5±0.4	8.9±0.1	8.69±0.06	8.07±0.02	8.12±0.02	0.24±0.1	34
WASP-19 b	4830±250	5720±300	2066±46	268.3±1.7	9.1±0.1	8.96±0.06	10.44±0.02	10.49±0.02	0.13±0.09	35
WASP-2 b	830±350	1690±170	1300±71	153.2±1.6	11.4±0.5	10.64±0.11	9.58±0.02	9.64±0.02	0.72±0.47	11
WASP-24 b	1590±130	2020±180	1769±39	322.1±4.4	9.6±0.1	9.33±0.1	10.1±0.02	10.13±0.02	0.23±0.14	36
WASP-33 b	2600±500	4100±200	2694±53	121.9±1.0	8.4±0.2	7.98±0.06	7.38±0.04	7.44±0.02	0.43±0.22	37
WASP-43 b	3460±130	3820±150	1375±79	86.7±0.3	10.6±0.0	10.58±0.05	9.15±0.02	9.22±0.02	0.03±0.07	38
WASP-48 b	1760±130	2140±200	2033±68	454.1±4.4	8.9±0.1	8.76±0.11	10.33±0.02	10.37±0.02	0.17±0.14	17
WASP-5 b	1970±280	2370±240	1742±68	309.1±3.4	9.9±0.2	9.7±0.11	10.54±0.02	10.59±0.02	0.15±0.19	39
WASP-6 b	940±190	1150±220	1184±32	197.1±1.6	11.4±0.2	11.21±0.21	10.28±0.02	10.34±0.02	0.16±0.3	4
WASP-67 b	220±130	800±180	1028±32	189.5±1.5	12.8±0.6	11.43±0.25	10.03±0.02	10.08±0.02	1.35±0.69	4
WASP-69 b	421±29	463±39	961±21	50.0±0.1	12.3±0.1	12.28±0.09	7.32±0.04	7.44±0.02	-0.02±0.13	6
WASP-8 b	1130±180	690±70	927±27	90.0±0.4	10.5±0.2	11.05±0.11	7.91±0.02	7.92±0.02	-0.55±0.21	40
WASP-80 b	455±100	944±65	775±25	49.8±0.1	13.2±0.2	12.4±0.08	8.3±0.02	8.32±0.02	0.77±0.25	41
XO-3 b	1010±40	1580±36	2046±40	213.1±2.7	9.6±0.1	9.13±0.04	8.75±0.02	8.76±0.02	0.47±0.07	42
XO-4 b	560±90	1350±85	1639±35	272.7±2.9	10.3±0.2	9.39±0.08	9.37±0.02	9.4±0.02	0.93±0.19	18
HAT-P-13 b	851±107	1090±124	1648±53	246.8±2.2	7.2±0.1	6.95±0.13	8.96±0.02	9.01±0.02	0.22±0.19	12
HAT-P-30 b	1603±107	1783±147	1637±43	214.0±2.2	6.9±0.1	6.8±0.09	9.04±0.02	9.08±0.02	0.08±0.12	12

Table 2.8: continued.

Planet	$(F_p/F_s)_{3.6}$	$(F_p/F_s)_{4.5}$	T_{eq} (a=0)	Distance	$M_{3.6}^{pl}$	$M_{4.5}^{pl}$	m_{W1}^s	m_{W2}^s	color	Ref.
	ppm	ppm	Kelvin	parsc	mag	mag	mag	mag	mag	
HAT-P-33 b	1663±127	1896±199	1780±34	396.1±7.5	6.5±0.1	6.33±0.12	10.0±0.02	10.02±0.02	0.13±0.16	12
HAT-P-40 b	988±168	1057±145	1765±66	464.5±6.4	6.7±0.2	6.62±0.15	9.98±0.02	10.01±0.02	0.04±0.24	12
KELT-2 A b	739±38	761±47	1710±31	134.1±0.8	7.0±0.1	6.99±0.07	7.27±0.04	7.34±0.02	-0.03±0.1	12
KELT-3 b	1788±97	1677±104	1822±44	210.3±5.4	6.3±0.1	6.43±0.09	8.57±0.02	8.6±0.02	-0.1±0.12	12
WASP-104 b	1709±195	2643±303	1516±43	185.9±1.5	7.9±0.1	7.5±0.13	9.84±0.02	9.91±0.02	0.41±0.18	12
WASP-46 b	1360±701	4446±589	1658±55	375.3±4.4	8.1±0.6	6.88±0.15	11.35±0.02	11.37±0.02	1.27±0.58	12
WASP-64 b	2859±270	2071±471	1690±52	369.9±3.0	7.0±0.1	7.38±0.25	10.96±0.02	11.01±0.02	-0.4±0.27	12
WASP-65 b	1587±245	724±318	1485±59	273.7±2.7	7.6±0.2	8.52±0.48	10.31±0.02	10.35±0.02	-0.9±0.51	12
WASP-76 b	2979±63	3762±82	2183±47	194.5±6.0	5.6±0.1	5.35±0.07	8.19±0.02	8.23±0.02	0.22±0.1	12
WASP-77 A b	2016±94	2487±127	1671±31	105.2±1.2	7.2±0.1	7.06±0.06	8.11±0.02	8.16±0.02	0.17±0.09	12
WASP-97 b	1359±84	1534±101	1540±42	151.1±0.5	7.7±0.1	7.65±0.07	8.96±0.02	9.01±0.02	0.08±0.1	12
WASP-74 b	1446±66	2075±100	1923±53	149.2±1.1	9.4±0.1	9.03±0.06	8.14±0.02	8.19±0.02	0.34±0.08	12
KELT-7 b	1688±46	1896±57	2050±35	136.7±0.9	8.7±0.0	8.65±0.04	7.5±0.03	7.52±0.02	0.1±0.06	12
WASP-79 b	1394±88	1783±106	1762±53	246.7±1.8	9.2±0.1	8.96±0.07	9.03±0.02	9.04±0.02	0.25±0.1	12

- (1) Zhao et al. (2014); (2) Machalek et al. (2008); (3) Todorov et al. (2010); (4) Garhart et al. (2020); (5) Kammer et al. (2015); (6) Todorov et al. (2013); (7) Wallack et al. (2019); (8) O'Donovan et al. (2010); (9) Beeler et al. (2011); (10) Machalek et al. (2009); (11) Benneke et al. (2019); (12) Wheatley et al. (2010); (13) Deming et al. (2011); (14) Morley et al. (2017); (15) Lewis et al. (2013); (16) Deming et al. (2015); (17) O'Rourke et al. (2014); (18) Todorov et al. (2012); (19) Christiansen et al. (2010); (20) Stevenson et al. (2012); (21) Charbonneau et al. (2008); (22) Diamond-Lowe et al. (2014); (23) Fortney et al. (2011); (24) Désert et al. (2011c); (25) Désert et al. (2011a); (26) Désert et al. (2011d); (27) Shporer et al. (2014); (28) Garhart et al. (2020); (29) Fressin et al. (2010); (30) ?; (31) Kreidberg et al. (2018a); (32) Stevenson et al. (2014c); (33) Blecic et al. (2013); (34) Nyfeler et al. (2011); (35) Anderson et al. (2013); (36) Smith et al. (2012); (37) Deming et al. (2012); (38) Blecic et al. (2014); (39) Baskin et al. (2013); (40) Cubillos et al. (2013); (41) Traiaud et al. (2015); (42) Machalek et al. (2010).

Table 2.9: The optimum parameters used for our pipeline which minimise the χ^2 of a least-squares fit to the systematics and the transit. If background method is “Annulus”, then the two parameters are the radius and width of a circular annulus, if it is “box” then the parameter is the size of the box taken in all of the 4 corners of the image. If the centroiding method is “baycenter” then the parameter is the number of pixels over which to create a box over the star for the flux weighting.

Planet	Channel	Aperture Size	Background Method	Background Params	Centroiding Method	Centroiding Params
		Pixels		Pixels		Pixels
HAT-P-32 b	ch1	2.50	Annulus	, 6, 4	Barycenter	3.0
HAT-P-32 b	ch2	2.50	Annulus	, 6, 4	Barycenter	5.0
XO-1 b	ch1	2.50	Annulus	, 6, 4	Moffat	-
XO-1 b	ch2	2.50	Annulus	, 6, 4	Gaussian	-
HAT-P-1 b	ch1	3.00	Box	4, -, -	Barycenter	5.0
HAT-P-1 b	ch2	3.50	Box	4, -, -	Barycenter	5.0
WASP-17 b	ch1	2.50	Annulus	, 6, 4	Barycenter	5.0
WASP-17 b	ch2	2.50	Annulus	, 6, 4	Barycenter	3.0
WASP-39 b	ch1	2.50	Annulus	, 6, 4	Barycenter	3.0
WASP-39 b	ch2	2.50	Annulus	, 6, 4	Barycenter	7.0
HAT-P-12 b	ch1	2.50	Annulus	, 6, 4	Moffat	-
HAT-P-12 b	ch2	2.50	Annulus	, 6, 4	Moffat	-
HAT-P-18 b	ch1	2.50	Annulus	, 6, 4	Barycenter	5.0
HAT-P-18 b	ch2	2.50	Annulus	, 6, 4	Moffat	-
TrES-2 b	ch1	2.50	Annulus	, 6, 4	Barycenter	5.0
TrES-2 b	ch2	2.50	Histogram	, -, -	Barycenter	3.0
WASP-4 b	ch1	2.50	Annulus	, 6, 4	Moffat	-
WASP-4 b	ch2	2.50	Annulus	, 6, 4	Barycenter	5.0
XO-2 b	ch1	2.50	Annulus	, 6, 4	Moffat	-
XO-2 b	ch2	2.50	Annulus	, 6, 4	Barycenter	7.0
GJ3470 b	ch1	2.50	Annulus	, 6, 4	Barycenter	3.0
GJ3470 b	ch2	2.50	Annulus	, 6, 4	Barycenter	3.0

Table 2.9: continued.

Planet	Channel	Aperture Size	Background Method	Background Params	Centroding Method	Centroding Params
		Pixels		Pixels		Pixels
WASP-21 b	ch1	2.50	Annulus	- , 6, 4	Barycenter	5.0
WASP-21 b	ch2	2.50	Annulus	- , 6, 4	Barycenter	5.0
WASP-31 b	ch1	2.50	Annulus	- , 6, 4	Barycenter	7.0
WASP-31 b	ch2	2.50	Annulus	- , 6, 4	Barycenter	7.0
WASP-1 b	ch1	2.50	Annulus	- , 6, 4	Barycenter	7.0
WASP-1 b	ch2	2.50	Annulus	- , 6, 4	Barycenter	7.0
HAT-P-26 b	ch1	2.50	Annulus	- , 6, 4	Barycenter	7.0
HAT-P-26 b	ch2	2.50	Annulus	- , 6, 4	Barycenter	5.0
WASP-107 b	ch1	2.25	Histogram	- , -, -	Barycenter	5.0
WASP-107 b	ch2	2.25	Histogram	- , -, -	Barycenter	3.0
WASP-13 b	ch1	2.25	Histogram	- , -, -	Gaussian	-
WASP-13 b	ch2	2.50	Histogram	- , -, -	Barycenter	3.0
WASP-121 b	ch1	1.00	Histogram	- , -, -	Barycenter	3.0
WASP-121 b	ch2	1.00	Box	4, -, -	Barycenter	3.0
WASP-69 b	ch1	2.00	Histogram	- , -, -	Gaussian	-
WASP-69 b	ch2	2.25	Histogram	- , -, -	Barycenter	3.0
WASP-67 b	ch1	2.00	Histogram	- , -, -	Moffat	-
WASP-67 b	ch2	2.00	Histogram	- , -, -	Moffat	-
HATS-7 b	ch1	2.00	Histogram	- , -, -	Barycenter	3.0
HATS-7 b	ch2	2.00	Histogram	- , -, -	Gaussian	-
WASP-29 b	ch1	2.25	Histogram	- , -, -	Gaussian	-
WASP-29 b	ch2	2.25	Histogram	- , -, -	Barycenter	3.0
HAT-P-41 b	ch1	2.25	Histogram	- , -, -	Barycenter	3.0
HAT-P-41 b	ch2	2.25	Histogram	- , -, -	Gaussian	-

Table 2.9: continued.

Planet	Channel	Aperture Size	Background Method	Background Params	Centroding Method	Centroding Params
		Pixels		Pixels		Pixels
WASP-101 b	ch1	2.25	Histogram	-,-,-	Barycenter	5.0
WASP-101 b	ch2	2.25	Histogram	-,-,-	Barycenter	3.0
WASP-131 b	ch1	2.25	Histogram	-,-,-	Barycenter	5.0
WASP-131 b	ch2	2.25	Histogram	-,-,-	Barycenter	3.0
WASP-36 b	ch1	2.00	Histogram	-,-,-	Gaussian	-
WASP-36 b	ch2	2.00	Histogram	-,-,-	Barycenter	3.0
WASP-63 b	ch1	2.25	Histogram	-,-,-	Barycenter	5.0
WASP-63 b	ch2	2.25	Histogram	-,-,-	Gaussian	-
WASP-79 b	ch1	2.50	Histogram	-,-,-	Barycenter	5.0
WASP-79 b	ch2	2.25	Histogram	-,-,-	Barycenter	3.0
WASP-94 Ab	ch1	2.50	Histogram	-,-,-	Moffat	-
WASP-94 Ab	ch2	2.25	Histogram	-,-,-	Barycenter	3.0
WASP-74 b	ch1	2.25	Histogram	-,-,-	Barycenter	3.0
WASP-74 b	ch2	2.00	Histogram	-,-,-	Barycenter	3.0
WASP-62 b	ch1	2.25	Histogram	-,-,-	Barycenter	3.0
WASP-62 b	ch2	2.25	Box	4,-,-	Barycenter	3.0
KELT-7 b	ch1	2.25	Histogram	-,-,-	Moffat	-
KELT-7 b	ch2	2.00	Histogram	-,-,-	Barycenter	3.0
Kepler-45 b	ch1	1.00	Histogram	-,-,-	Barycenter	3.0
Kepler-45 b	ch1	1.00	Histogram	-,-,-	Gaussian	-
Kepler-45 b	ch1	1.00	Histogram	-,-,-	Gaussian	-
Kepler-45 b	ch2	1.00	Histogram	-,-,-	Gaussian	-
Kepler-45 b	ch2	1.00	Histogram	-,-,-	Barycenter	3.0

Table 2.9: continued.

Planet	Channel	Aperture Size Pixels	Background Method	Background Params Pixels	Centroiding Method	Centroiding Params Pixels
Kepler-45 b	ch2	1.00	Histogram	~, -	Moffat	-
Kepler-45 b	ch2	1.00	Box	2, -, -	Gaussian	-

Table 2.10: Statistical tests outputted by our custom built pipeline. We measure the strength of the dependence on the chosen limb darkening parameters by varying them within 3σ of their error for 500 iterations, for each iteration we perform a least-squares fit and measure the variation on the measured R_p/R_s as a function of the final calculated error on R_p/R_s . Bad pix - the number of bad pixels corrected at the beginning of the analysis. Cut time (min) - the number of minutes cut from the beginning of each observation, this value is chosen such that we keep as much baseline as possible while minimizing the chi2 of the different possible baselines. Photon noise - the percentage above pure statistical noise we have for each lightcurve, typical values for Spitzer are 30-60% above photon noise.

Planet	$\lambda(\mu m)$	Vary 1d 3σ	Bad pix %	Cut time (min)	Photon noise %	MCMC acceptance fraction
HAT-P-32 b	3.6	0.804	0.306	0.0	1.31	0.384
HAT-P-32 b	4.5	0.603	0.056	0.0	1.32	0.383
XO-1 b	3.6	0.442	0.113	10.0	1.31	0.384
XO-1 b	4.5	0.194	0.061	10.0	1.23	0.385
HAT-P-1 b	3.6	0.018	0.270	10.0	1.47	0.386
HAT-P-1 b	4.5	0.035	0.052	10.0	1.34	0.385
WASP-17 b	3.6	0.198	0.309	50.0	1.41	0.385
WASP-17 b	4.5	0.106	0.058	30.0	1.37	0.386
WASP-39 b	3.6	1.188	0.294	20.0	1.39	0.382
WASP-39 b	4.5	0.416	0.062	0.0	1.32	0.381
HAT-P-12 b	3.6	0.387	0.289	10.0	1.35	0.382
HAT-P-12 b	4.5	0.273	0.062	10.0	1.34	0.383
HAT-P-18 b	3.6	0.382	0.243	20.0	1.47	0.382
HAT-P-18 b	4.5	0.183	0.067	0.0	1.34	0.385
TfES2 b	3.6	0.332	0.275	10.0	1.33	0.383
TfES2 b	4.5	0.193	0.069	5.0	1.26	0.385
WASP-4 b	3.6	1.424	0.295	10.0	1.53	0.384
WASP-4 b	4.5	0.771	0.049	30.0	1.48	0.385
XO-2 b	3.6	0.156	0.250	30.0	1.27	0.385
XO-2 b	4.5	0.052	0.048	20.0	1.24	0.383
GJ3470 b	3.6	0.523	0.007	5.0	1.22	0.382
GJ3470 b	4.5	0.246	0.006	5.0	1.28	0.383

Table 2.10: continued.

Planet	$\lambda(\mu\text{m})$	Vary ld	3σ	Bad pix %	Cut time (min)	photon noise %	MCMC acceptance fraction
WASP-21 b	3.6		0.029	0.242	40.0	1.39	0.383
WASP-21 b	4.5		0.020	0.070	10.0	1.32	0.383
WASP-31 b	3.6		0.034	0.317	30.0	1.46	0.383
WASP-31 b	4.5		0.037	0.055	10.0	1.43	0.383
WASP-1 b	3.6		0.742	0.331	10.0	1.43	0.384
WASP-1 b	4.5		0.490	0.055	40.0	1.39	0.387
HAT-P-26 b	3.6		1.501	0.265	10.0	1.35	0.384
HAT-P-26 b	4.5		0.689	0.069	10.0	1.29	0.383
WASP-107 b	3.6		9.628	0.010	95.0	1.30	0.384
WASP-107 b	4.5		4.939	0.048	15.0	1.26	0.385
WASP-13 b	3.6		0.319	0.263	55.0	1.25	0.383
WASP-13 b	4.5		0.137	0.060	10.0	1.26	0.384
WASP-121 b	3.6		0.585	0.248	45.0	1.13	0.384
WASP-121 b	4.5		0.343	0.070	30.0	1.08	0.382
WASP-69 b	3.6		0.078	0.008	30.0	1.25	0.383
WASP-69 b	4.5		0.057	0.009	25.0	1.21	0.382
WASP-67 b	3.6		0.548	0.193	45.0	1.33	0.385
WASP-67 b	4.5		0.196	0.075	30.0	1.24	0.385
HATS-7 b	3.6		0.039	0.240	35.0	1.38	0.386
HATS-7 b	4.5		0.017	0.056	30.0	1.40	0.385
WASP-29 b	3.6		1.719	0.274	70.0	1.35	0.384
WASP-29 b	4.5		0.822	0.054	10.0	1.22	0.381
HAT-P-41 b	3.6		0.403	0.221	30.0	1.31	0.382
HAT-P-41 b	4.5		0.201	0.061	150.0	1.27	0.384
WASP-101 b	3.6		0.231	0.261	30.0	1.33	0.385

Table 2.10: continued.

Planet	$\lambda(\mu\text{m})$	Vary ld 3 σ	Bad pix %	Cut time (min)	photon noise %	MCMC acceptance fraction
WASP-101 b	4.5	0.140	0.064	30.0	1.21	0.384
WASP-131 b	3.6	0.027	0.304	30.0	1.26	0.383
WASP-131 b	4.5	0.033	0.068	35.0	1.25	0.383
WASP-36 b	3.6	0.001	0.320	110.0	1.49	0.384
WASP-36 b	4.5	0.003	0.075	40.0	1.42	0.383
WASP-63 b	3.6	0.298	0.307	60.0	1.30	0.385
WASP-63 b	4.5	0.107	0.058	10.0	1.23	0.384
WASP-79 b	3.6	0.169	0.291	35.0	1.45	0.385
WASP-79 b	4.5	0.158	0.062	10.0	1.22	0.385
WASP-94 Ab	3.6	0.591	0.268	105.0	1.35	0.384
WASP-94 Ab	4.5	0.348	0.065	30.0	1.21	0.385
WASP-74 b	3.6	0.894	0.008	90.0	1.26	0.384
WASP-74 b	4.5	0.560	0.007	70.0	1.24	0.384
WASP-62 b	3.6	0.373	0.255	85.0	1.47	0.384
WASP-62 b	4.5	0.239	0.064	40.0	1.21	0.384
KELT-7 b	3.6	0.248	0.009	60.0	1.29	0.384
KELT-7 b	4.5	0.182	0.007	50.0	1.21	0.382
Kepler-45 b	3.6	0.022	0.277	30.0	1.50	0.383
Kepler-45 b	3.6	0.021	0.280	10.0	1.55	0.384
Kepler-45 b	3.6	0.026	0.269	40.0	1.71	0.384
Kepler-45 b	3.6	0.024	0.265	20.0	1.78	0.384
Kepler-45 b	4.5	0.005	0.047	20.0	1.44	0.384
Kepler-45 b	4.5	0.006	0.065	20.0	1.51	0.383
Kepler-45 b	4.5	0.008	0.059	20.0	1.41	0.383
Kepler-45 b	4.5	0.005	0.052	20.0	1.46	0.385

2.B VULCAN validation on HD 209458b

2.C Radius Anomaly

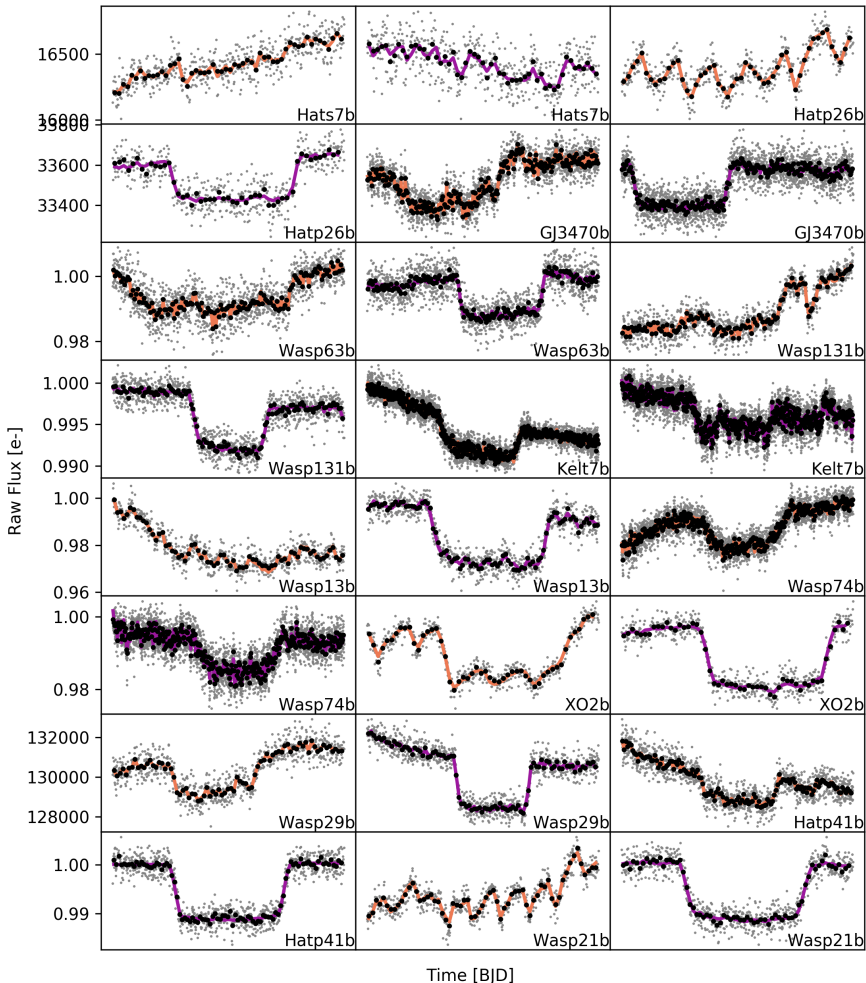


Fig. 2.14: Raw lightcurves for each planet. Flux binned in 5 minutes is shown in black and 30 seconds is shown in gray. Colored lines indicate the best-fit instrumental and transit model from our MCMC analysis.

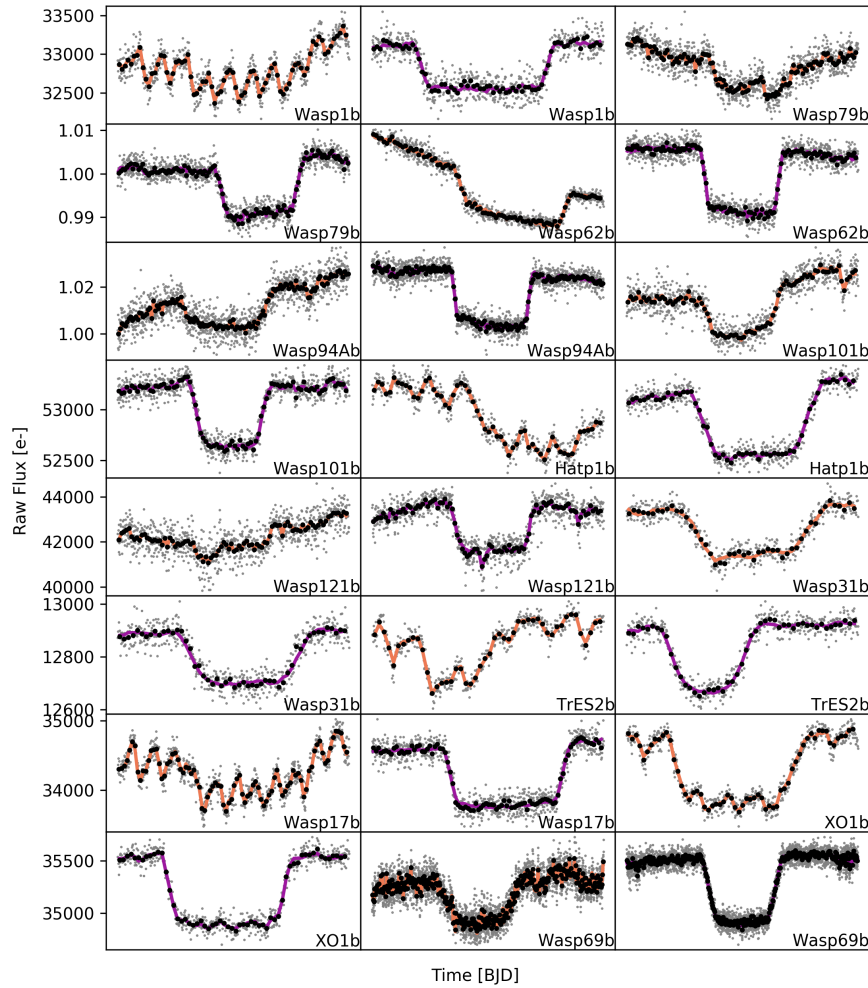


Fig. 2.14: *Continued.*

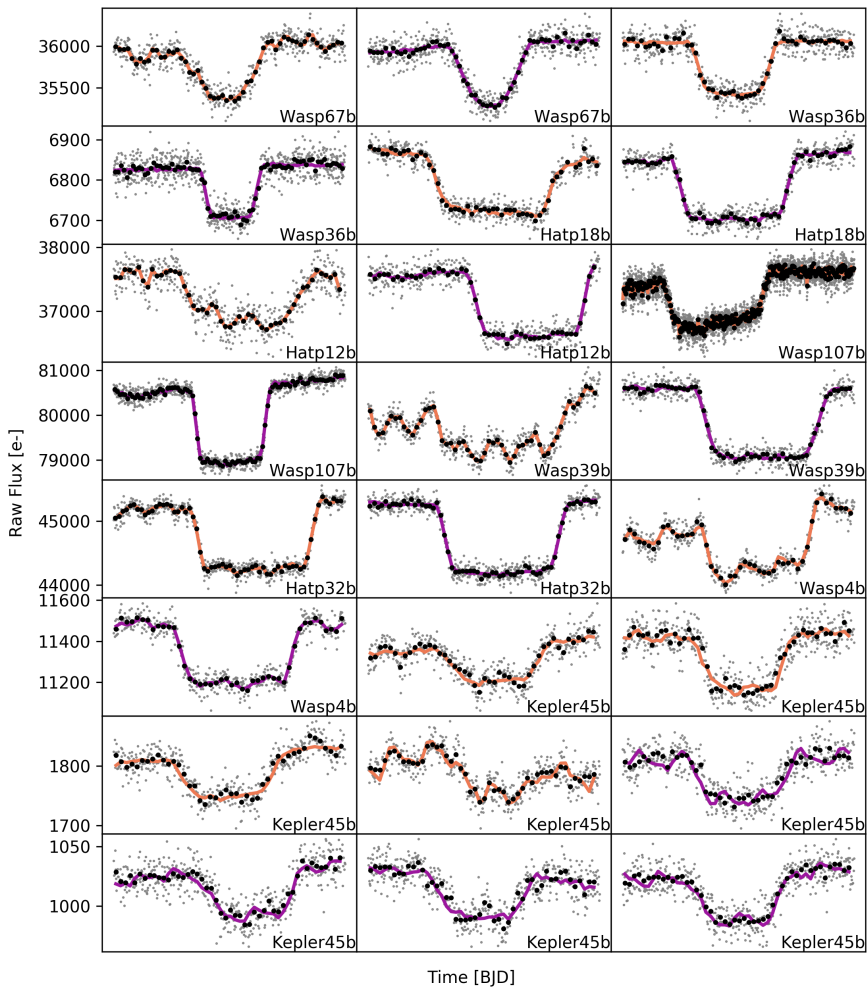


Fig. 2.14: *Continued.*

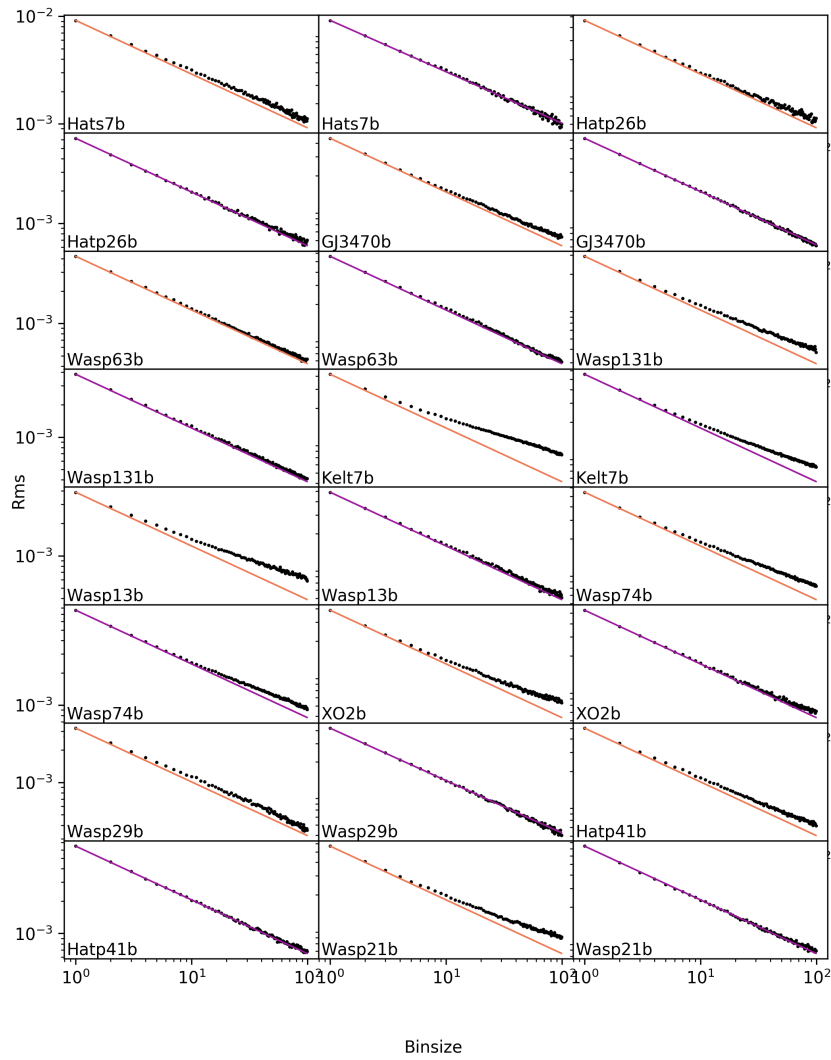
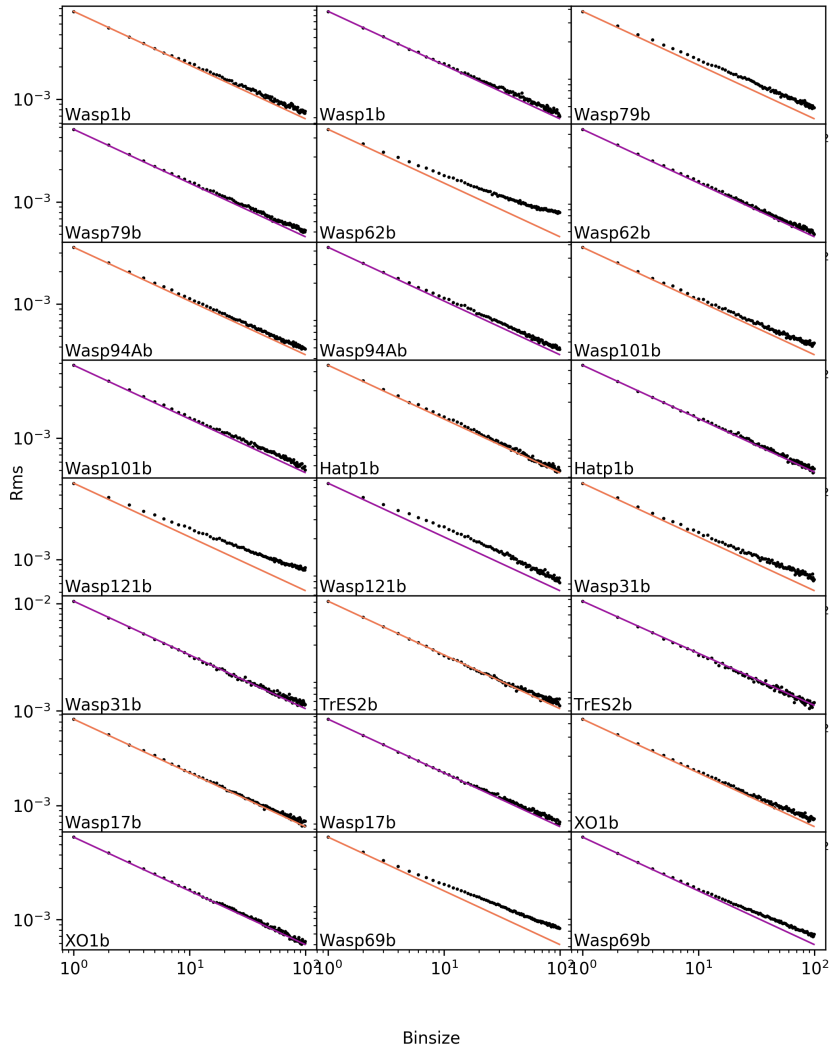


Fig. 2.15: RMS vs normalized binsize of each of the fitted lightcurves. Straight line is the \sqrt{N} theoretical value.

**Fig. 2.15:** *Continued.*

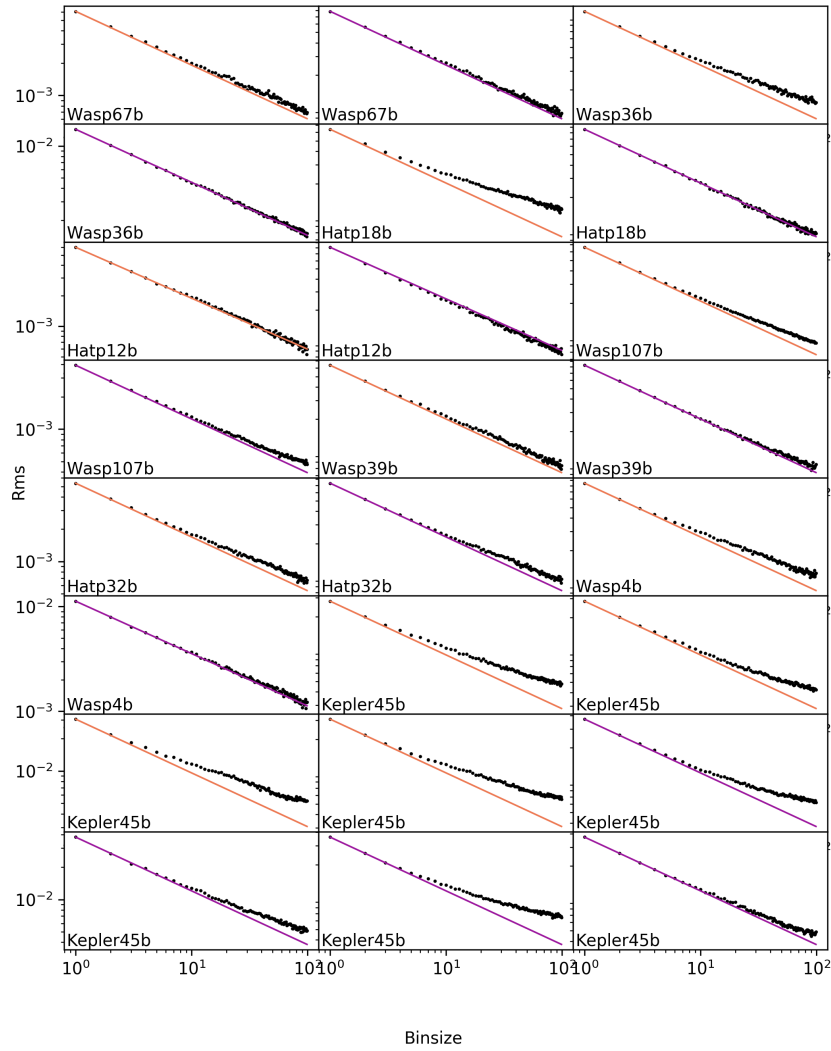


Fig. 2.15: *Continued.*

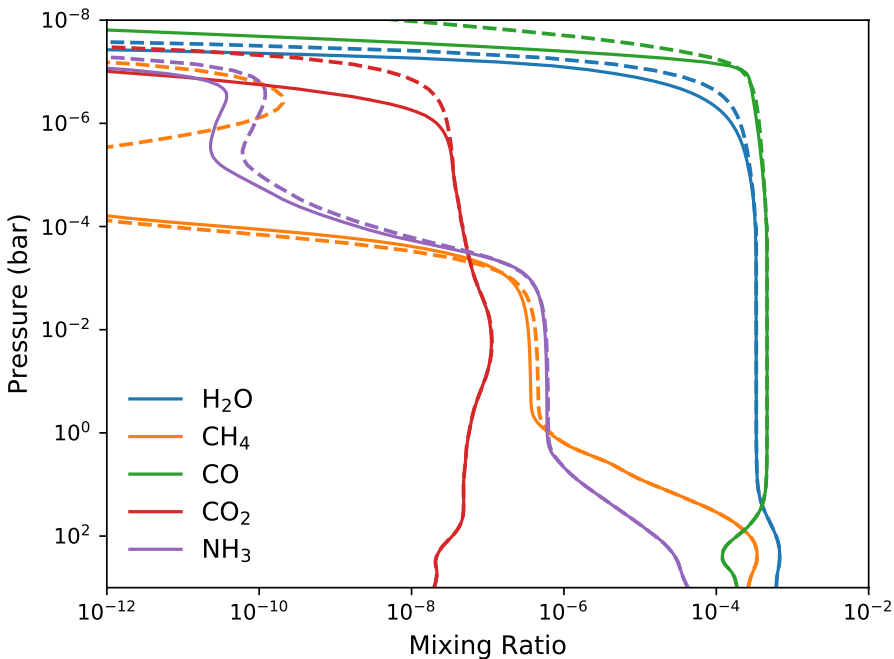


Fig. 2.16: Abundance mixing ratios at different pressures for the main species in the Spitzer bandpasses in HD 209458 b. The solid line shows the results from our VULCAN calculation and the dashed line the results from Moses et al. (2011). The temperature and eddy-diffusion structure are taken the same as the dayside-average P-T profile in Moses et al. (2011). The solar flux is also used as an analog for HD 290458 at a distance of 0.04747 AU.

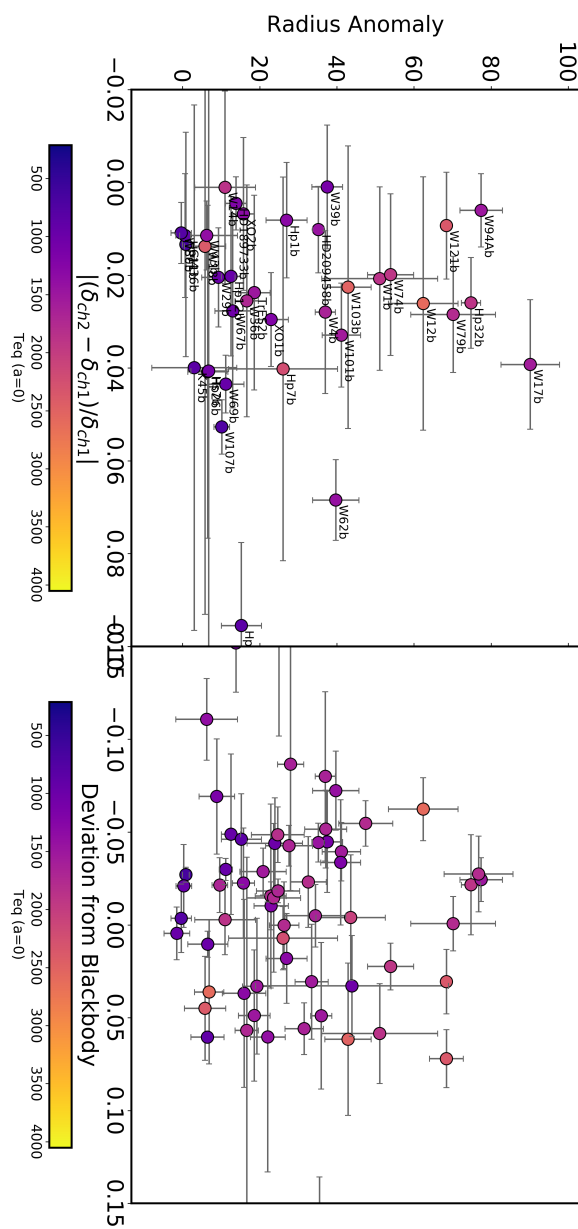


Fig. 2.17: Radius Anomaly (calculated using models from Thorngren et al. (2016); Thorngren & Fortney (2018) against the absolute value of the normalized difference in transit depths for the available planets. Color scale is the equilibrium temperature of the planet.

3

A TRANSITION BETWEEN THE HOT AND THE ULTRA-HOT JUPITER ATMOSPHERES

Claire Baxter, Jean-Michel Désert, Vivien Parmentier, Michael Line, Jonathan J. Fortney, Jacob Arcangeli, Jacob L. Bean, Kamen O. Todorov, Megan Mansfield

Astronomy & Astrophysics, 639, A36 (2020)

Abstract

A key hypothesis in the field of exoplanet atmospheres is the trend of atmospheric thermal structure with planetary equilibrium temperature. We explore this trend and report here the first statistical detection of a transition in the near-infrared (NIR) atmospheric emission between hot and ultra-hot Jupiters. We measure this transition using secondary eclipse observations and interpret this phenomenon as changes in atmospheric properties, and more specifically in terms of transition from non-inverted to inverted thermal profiles. We examine a sample of 78 hot Jupiters with secondary eclipse measurements at $3.6\text{ }\mu\text{m}$ and $4.5\text{ }\mu\text{m}$ measured with Spitzer Infrared Array Camera (IRAC). We calculate the planetary brightness temperatures using PHOENIX models to correct for the stellar flux. We measure the deviation of the data from the blackbody, which we define as the difference between the observed $4.5\text{ }\mu\text{m}$ eclipse depth and that expected at this wavelength based on the brightness temperature measured at $3.6\text{ }\mu\text{m}$. We study how the deviation between 3.6 and $4.5\text{ }\mu\text{m}$ changes with theoretical predictions with equilibrium temperature and incoming stellar irradiation. We reveal a clear transition in the observed emission spectra of the hot Jupiter population at $1660 \pm 100\text{ K}$ in the zero albedo, full redistribution equilibrium temperature. We find the hotter exoplanets have even hotter daysides at $4.5\text{ }\mu\text{m}$ compared to $3.6\text{ }\mu\text{m}$, which manifests as an exponential increase in the emitted power of the planets with stellar insolation. We propose that the measured transition is a result of seeing carbon monoxide in emission due to the formation of temperature inversions in the atmospheres of the hottest planets. These thermal inversions could be caused by the presence of atomic and molecular species with high opacities in the optical and/or the lack of cooling species.

Our findings are in remarkable agreement with a new grid of 1D radiative and convective models varying metallicity, carbon to oxygen ratio (C/O), surface gravity, and stellar effective temperature. We find that the population of hot Jupiters statistically disfavors high C/O planets ($\text{C}/\text{O} \geq 0.85$).

3.1 Introduction

Observing the infrared secondary eclipse of transiting tidally locked hot Jupiters allows us to measure their dayside thermal flux (e.g., Charbonneau et al. 2005; Deming et al. 2005; Cowan & Agol 2011b,a; Triaud 2014; Schwartz & Cowan 2015; Schwartz et al. 2017; Zhang et al. 2018; Garhart et al. 2020). The dayside flux is determined by the temperature pressure (T-P) profile and the atmospheric opacities. In turn, the T-P profile is determined by the albedo, heat redistribution, and atmospheric opacities. Hot Jupiters have equilibrium temperatures around 1500K. But recently, a newer class of hot Jupiters has emerged, the ultra-hot Jupiters (UHJ). Ultra-hot Jupiters have equilibrium temperatures in excess of 2000K and receive irradiation 10-100 times the insolation of other hot Jupiters (e.g., Figure 9. Parmentier & Crossfield 2018). There is evidence that they exhibit different atmospheric properties from their cooler counterparts (e.g., Bell et al. 2017; Arcangeli et al. 2018; Mansfield et al. 2018; Parmentier & Crossfield 2018; Kreidberg et al. 2018a). Investigations by Hubeny et al. (2003); Fortney et al. (2006) and Fortney et al. (2008) suggest that temperature inversions could appear in hot Jupiter atmospheres at temperatures as low as 1700K resulting from a fundamental change in atmospheric opacity due to TiO and VO (Gandhi & Madhusudhan 2019). Furthermore, Thorngren et al. (2019) suggest that the deep atmospheres of these planets are so hot that TiO and VO are able to stay in the gas phase at \sim 1700-2000K rather than being cold-trapped into clouds at depth.

Previous studies have looked for signatures of physical processes (chemistry, thermal inversions, redistribution, albedo, stellar activity) in a large sample of atmospheres, specifically by looking at the thermal eclipse measurements (Knutson et al. 2010; Cowan & Agol 2011a; Triaud 2014; Schwartz & Cowan 2015; Schwartz et al. 2017; Zhang et al. 2018; Garhart et al. 2020; Keating et al. 2019; Melville et al. 2020). Triaud (2014) created color-magnitude diagrams of planets with available Spitzer/IRAC eclipses in all four bandpasses (3.6, 4.5, 5.8, and 8.0 μm). They found that hot Jupiters lie closer to brown dwarf (MLT) colors than they do to blackbodies, (i.e., they do not have featureless spectra in the infrared).

Additional studies have focused on breaking the degeneracy between albedo and redistribution efficiency. Cowan & Agol (2011b) perform a statistical study on the energy budget of 24 hot Jupiters with secondary eclipses in at least one infrared waveband ($>0.8 \mu\text{m}$) and, when available, phase variation measurements. They found the sample as a whole could be represented with low Bond albedos. Additionally, in combination with Zhang et al. (2018), there is evidence of low redistribution efficiencies of the eight hottest planets (WASP-12b, WASP-18b, HAT-P-7b, OGLE-TR-56b, WASP-19b, CoRoT-1b, WASP-33b, HD149026b), suggesting that these atmospheres could exhibit different behaviors from the rest.

Following this, Schwartz & Cowan (2015) calculate the dayside temperature of 50 planets with thermal eclipse measurements in at least two infrared wavelengths ($>0.8 \mu\text{m}$). They note an unexpectedly steep correlation, such that the hotter planets had temperatures even hotter than irradiation temperature predictions. This supports the previous claim by Cowan & Agol (2011b) that the hottest planets have lower Bond albedo and/or less efficient heat

transport. Schwartz et al. (2017) incorporate phase offsets into their energy budget calculations of six planets, which pushes the results toward lower Bond albedos and slightly higher heat transport than before. Keating et al. (2019) and Beatty et al. (2019) estimate the nightside temperature of several hot Jupiters using Spitzer phase curves and find that despite the different levels of irradiation, they all demonstrate similar nightside temperatures. This suggests that they might all have some chemically similar high optically thick cloud layer that is emitting at the nightside temperature.

Additionally, Garhart et al. (2020) perform uniform analyses of 36 planets with Spitzer/IRAC secondary eclipses at 3.6 and $4.5\text{ }\mu\text{m}$. They find an increasing trend in the brightness temperature ratio with equilibrium temperature. They find that this trend is present throughout the entire temperature range continuously between the coolest and the hottest planets (800K to 2500K).

Our study builds on the previous works by expanding to 78 planets, with almost double the number of ultra-hot Jupiters, and by employing a careful treatment of the stellar flux. We use the two warm Spitzer/IRAC bandpasses ($3.6\text{ }\mu\text{m}$ and $4.5\text{ }\mu\text{m}$) (Fazio et al. 2004; Werner et al. 2004) to study the near infrared trends in hot Jupiter emission. At these wavelengths, based on equilibrium chemistry, we expect to see spectral signatures of methane (CH₄) (in the cooler planets) and carbon monoxide (CO) (in the hotter planets). More specifically, we focus on the deviation of these points from a blackbody, particularly on its effect when including the ultra-hot Jupiters. Furthermore, we now compare our results to a grid of forward models that encompass the processes relevant for the coolest to the ultra-hot planet atmospheres (molecular dissociation, H- opacity, latent heat, and the formation of temperature inversions). In Section 3.2 we describe the Spitzer/IRAC observations and data collection. In Section 3.3 we describe the data analysis and the various temperatures used. In Section 3.4 we present the results of the survey, we make a comparison to blackbodies, and demonstrate a transition to the ultra-hot Jupiters. In Section 3.5 we interpret our results in terms of albedo, redistribution, and temperature inversions.

3.2 Observations

Our comprehensive survey is composed of 78 planets with eclipse depths taken with the Spitzer/IRAC at $3.6\text{ }\mu\text{m}$ and $4.5\text{ }\mu\text{m}$. The literature data for the planets in this survey were collected via exoplanets.org (Han et al. 2014), exoplanet.eu (Schneider et al. 2011), or directly from the studies. We analyzed two $4.5\text{ }\mu\text{m}$ eclipses of KELT-9b (Mansfield et al. 2020) using our custom pipeline (Baxter et al. in prep.) implementing Pixel Level Decorrelation to correct systematics (Deming et al. 2015) (Appendix 3.D). The planets, eclipse depths, stellar parameters, references, and key results and uncertainties are displayed in Table 3.2. Our work relies on the calculation of the equilibrium temperature, and since this parameter is sensitive to the eccentricity of the planetary orbit, especially on short period exoplanets, we opted to perform an eccentricity cut and only select planets with eccentricity less than 0.2.

3.3 Data analysis

3.3.1 Calculating the planetary brightness temperatures

The secondary eclipse depth measures the ratio of the planetary flux (F_p) to the stellar flux (F_s) at a given spectral bandpass. The planets selected for our survey have eclipse depths (F_p/F_s) measured in the two Spitzer/IRAC bandpasses (3.6 μm and 4.5 μm) (Werner et al. 2004). We remove the contribution of the stellar flux from the eclipse depths and convert the planetary flux to flux density (erg cm $^{-2}$ s $^{-1}$ Å $^{-1}$), which we use to calculate the brightness temperature by inverting the Planck function for the planet

$$T_b(\lambda) = \frac{hc}{k_b\lambda} \left[\ln \left(\frac{2hc^2\pi\delta_{tra}}{\lambda^5 \bar{F}_s(\lambda)\delta_{occ}} \right) \right]^{-1}, \quad (3.1)$$

where δ_{tra} is the published transit depth (R_p/R_s) 2 , and δ_{occ} is the eclipse depth measured at the Spitzer wavelengths (F_p/F_s), λ is the wavelength of the observed eclipse depth, either 3.6 μm or 4.5 μm , and $\bar{F}_s(\lambda)$ is the flux density of the stellar model weighted by the Spitzer/IRAC spectral response at this wavelength.

Since both the planetary and the stellar model need to be integrated over the Spitzer spectral response functions, the spectral response weighted brightness temperature needs to be calculated iteratively. We create a grid of brightness temperatures around an estimated value (obtained from solving equation 3.1 directly) and convert this to a grid of eclipse depths by convolving both the planetary blackbody function and the stellar models with the spectral responses. Our adopted brightness temperature is thus the one that produces the eclipse depth which best matches the data (lowest χ^2). For this minimization we chose grids encompassing 200K around the calculated brightness temperatures, with step sizes of 2K, which is much smaller than the typical uncertainty of 100K. We then confirmed that we had reached a minimum χ^2 for each planet.

The integration of the spectral response with the model flux densities is done using the following equation:

$$\bar{F}(\lambda) = \frac{\int_0^\infty F(\lambda)\lambda R(\lambda)d\lambda}{\int_0^\infty \lambda R(\lambda)d\lambda}. \quad (3.2)$$

Here $R(\lambda)$ is the spectral response function at either 3.6 μm or 4.5 μm [e-/photon] taken from Quijada et al. (2004) and $F(\lambda)$ is the flux density of the planet or the star. The output, $\bar{F}(\lambda)$, is the average flux density that would be observed with Spitzer/IRAC.

We decided to estimate the uncertainties on the adopted brightness temperatures by taking the minimum and maximum eclipse depth (based on the 1σ uncertainty presented in Table 3.2) and propagating it through Equation 3.1 to calculate a minimum and maximum brightness temperature. The 1σ uncertainty on the brightness temperature is then the mean of these two deviations from the best fit brightness temperature. Since the Rayleigh-Jeans limit is for long wavelengths and high temperatures, the Rayleigh-Jeans formula cannot be simply used

to calculate the uncertainties as the temperatures of the planets are overestimated. However, the formula can be used to get an estimate of the uncertainties provided the temperatures used in the propagation are those calculated using the full Planck function. Our method estimates uncertainties that are equivalent to those calculated using the differentiated and propagated Rayleigh-Jeans law formula.

We test different stellar models to correct the stellar flux contribution when calculating T_B (see Appendix 3.B). We then compare these temperatures to theoretical predictions for the zero albedo full redistribution equilibrium temperature $T_{eq,0}$, irradiation temperature T_0 , and maximum dayside temperature T_{max} . Throughout this paper we fit all correlations with an orthogonal distance regression (ODR), and obtain uncertainties by bootstrapping (see Appendix 3.A.1).

3.3.2 Extracting the planetary flux deviation from a blackbody

We define a new metric that allows us to self-consistently compare how similar these planets are to blackbodies. We do this by first calculating the brightness temperature at $3.6\ \mu\text{m}$ then we propagate this as a blackbody to $4.5\ \mu\text{m}$ and recalculate the expected eclipse depth at $4.5\ \mu\text{m}$. We measure the deviation between this value and the actual $4.5\ \mu\text{m}$ eclipse depth (Observed - Calculated) and call it the deviation from the blackbody (devBB). A positive deviation means that the $4.5\ \mu\text{m}$ eclipse depth is greater than expected. Uncertainties are fully propagated from the uncertainties on the eclipse depths at 3.6 and $4.5\ \mu\text{m}$. Results are displayed in Table 3.2. Since devBB is the difference of flux ratios it is unitless, but for convenience we express it as the difference in percentages. We also note that using the Rayleigh-Jeans law, we can demonstrate that the deviation from the blackbody is equivalent to the normalized difference in the brightness temperatures. However, it has the advantage that it is derived directly from an observable quantity, the planet-to-star flux ratio.

3.3.3 Irradiation, equilibrium, effective, and max dayside temperatures definitions

Following Hansen (2008), we define the irradiation temperature (T_0) as the temperature of the planetary atmosphere at the substellar point caused by the irradiation received from the host star at the distance of the planetary orbit $T_0 = T_{eff} \sqrt{R_*/a}$, where T_{eff} is the stellar effective temperature, R_* is the stellar radius, and a is the semi-major axis of the orbit (assuming a circular orbit). The equilibrium temperature is another theoretical calculation that takes into account the albedo of the planet and the amount of redistribution over the planet's surface. The equilibrium temperature for isotropic (full) redistribution of incoming irradiation is thus defined as $T_{eq} = T_{eff}(1 - A_B)^{1/4} \sqrt{R_*/2a}$, where A_B is the planetary Bond albedo. When we take the Bond albedo to be zero and assume full redistribution, the equilibrium temperature can be written in terms of the irradiation temperature: $T_{eq,0} = (1/4)^{1/4} T_0$. Subsequently, we define the disk integrated apparent maximum dayside temperature (Schwartz et al. 2017) as

the equilibrium temperature where the incoming radiation is immediately re-radiated (i.e., no redistribution: $T_{eq,max} = (2/3)^{1/4}T_0$). We do not expect any planets to have temperatures hotter than this as we do not expect any heat from contraction since most of these stars have ages $\gtrsim 1$ Gyr. Furthermore, since temperatures add to the fourth power, even planets with a substantially high internal temperature (e.g., Thorngren et al. 2019) would be within the noise for this study. The uncertainties on these temperatures are calculated through full propagation of uncertainties from the stellar and orbital parameters.

The final temperature used in our analysis is the planetary effective temperature used in Appendix 3.C. We calculate the average brightness temperature, which we take as the error weighted mean of the two brightness temperatures, such that $\langle T_B \rangle = (T_{b_{3.6}}/\sigma_{3.6}^2 + T_{b_{4.5}}/\sigma_{4.5}^2)/2$, where T_{b_λ} is the brightness temperature at wavelength λ and σ_λ is the corresponding error on this measurement. $\langle T_B \rangle$ is algebraically the same as T_{eff} defined in Schwartz & Cowan (2015) and Cowan & Agol (2011a).

3.3.4 Grid of forward emission models to interpret observations

We utilize a new grid of cloud-free self-consistent radiative-convective thermochemical-equilibrium grid models, ScCHIMERA, originally developed and validated against analytical solutions and previously published brown dwarf models in Piskorz et al. (2018) and subsequently applied to the UHJ datasets presented in Arcangeli et al. (2018); Mansfield et al. (2018) and Kreidberg et al. (2018a). These new models are a successor to the Fortney et al. (2008) models.

Briefly, the model solves for the temperature profile through a vertical flux divergence minimizing via the Newton-Raphson iteration (McKay et al. 1989) utilizing the two stream source function technique for the radiative fluxes (Toon et al. 1989). Mixing length theory is used to compute the convective fluxes as prescribed in Hubeny (2017). Opacities (at R=100, 0.3 - 200 μm , where available) are treated within the correlated-K resort-rebin mixing framework (Lacis & Oinas 1991; Amundsen et al. 2017) and include hot Jupiter-to-UHJ relevant atoms/molecules/ions: H₂-H₂/He collision induced absorption, H₂O, CO, CO₂, CH₄, NH₃, H₂S, HCN, C₂H₂, Na, K, TiO, VO, FeH, H- free-free/bound-free, PH₃, Fe, Fe+, Ca, and Mg, obtained from a variety of sources (ExoMol, Freedman et al. (2008, 2014) and Kurucz & Bell (1995)). Figure 3.1 demonstrates a selection of the abundance weighted opacities extracted at the approximate pressure of the Spitzer contribution functions for three example planets (1000K, 1800K, and 3000K). Atom/Molecule/Ion abundances are computed using the Gibbs free energy minimization routine, NASA CEA2 (?), given the specified scaling to the Lodders et al. (2009) elemental abundances. This approach also accounts for vertically varying abundances from thermal dissociation. The model assumes full redistribution at a given irradiation temperature, and an internal temperature of 150K (however, see Thorngren et al. (2019)). We utilize the PHOENIX (Allard et al. 2011) models derived from the STScI pysynphot routine for the incident stellar flux (assuming a hemispheric mean incident flux-u=0.5).

The model grid consists of 297 spectra and spans a range of carbon to oxygen ratios (C/O

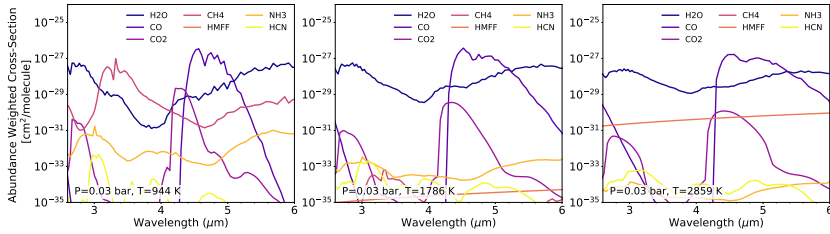


Fig. 3.1: Abundance weighted cross sections for a selection of the emission model grid described in Section 3.3.4, (Piskorz et al. 2018). Each panel presents the abundance weighted cross sections for planets with equilibrium temperatures of 1000K, 1800K, and 3000K. Each TP profile is for a planet around a 5300K star with C/carbon to oxygen (O =) 0.54, $[M/H] = 0.0$, $\log g = 3.0$; the full grid is shown in the first panel of Figure 3.2. The plotted abundances are taken from a pressure of 30mbar, resulting in probing temperatures of 944K, 1786K, and 2859K in each of the respective TP profiles.

$= 0.1, 0.54, 0.84$), planetary surface gravities ($\log(g) = 2.5, 3.0, 3.5, 4.0$), metallicity ($[M/H] = -1, 0, 1, 1.5$), stellar temperatures ($T_{eff} = 4300, 5300, 6300$ K), and planetary equilibrium temperatures ($T_{eq,0} = 1000-3600$ K in steps of 100K). Figure 3.2 demonstrates a selection of the emission spectra at the Spitzer wavelengths, where F_p/F_s is calculated using $R_s/R_p = 9.95$. We show three tracks corresponding to the three different stellar temperatures. For 4300K and 6300K we fix $[M/H] = 0$, C/O = 0.54, and $\log(g) = 3$, whereas for 5300K we show $[M/H] = 1.5$, C/O = 0.54, and $\log(g) = 3$. The right panel contains the temperature pressure profile, which shows the atmosphere turning isothermal very briefly for planetary atmospheres with an equilibrium temperature of 1900K and the temperature inversion appearing for models with equilibrium temperature of 2200K. The left panel demonstrates the emission spectra: carbon monoxide can be seen clearly in emission for the hottest temperatures where the inversion exists.

3.4 Results

3.4.1 Deviation between equilibrium and brightness temperatures

In Figure 3.3 we present the measured brightness temperatures plotted against $T_{eq,0}$ for the two IRAC bandpasses. We fit linear functions using an orthogonal distance regression (ODR), see Appendix 3.A.1). If the brightness temperature is the same as $T_{eq,0}$ then the gradient of the slope will be unity. The measured gradients at $3.6 \mu\text{m}$ and $4.5 \mu\text{m}$ are 1.09 ± 0.06 and 1.19 ± 0.06 , respectively. At $4.5 \mu\text{m}$, this is a statistically significant (3.2σ) deviation from $T_{eq,0}$. On the other hand, at $3.6 \mu\text{m}$ the brightness temperatures are consistent with the equilibrium temperature (1.5σ). Thus, the source of this deviation exhibits a stronger effect at $4.5 \mu\text{m}$ compared to $3.6 \mu\text{m}$. Furthermore, comparing to the grid of forward models demonstrates that the different stellar temperature model grids converge at lower tempera-

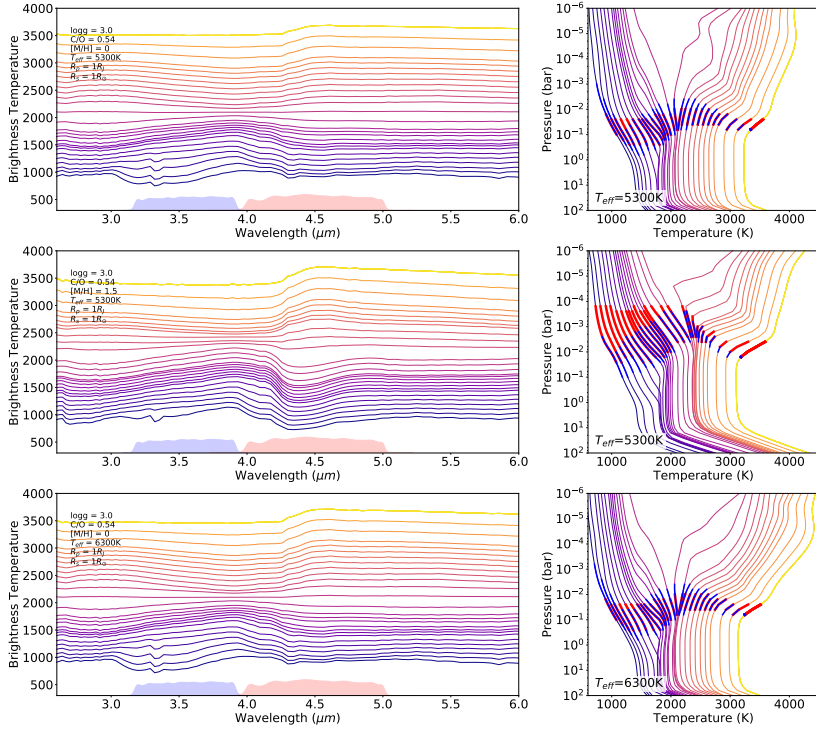


Fig. 3.2: ScCHIMERA model emission spectra for hot Jupiters (Piskorz et al. 2018) for a set of models of varying equilibrium temperature with $\log(g) = 3.0$, C/O = 0.54, [M/H] = 0, $R_p = 1R_J$, and $R_* = 1R_\odot$. In each row we show the flux ratio (left) and temperature pressure profiles (right) for the 1D atmospheres of planets with colors indicating the increasing equilibrium temperatures ranging from 1000K to 3600K (in 100K increments). Top, middle, and bottom rows show the grid for planets around a 4300K, 5300K, and a 6300K star, respectively. Blue and red shaded regions in the left panel indicate the Spitzer/IRAC 3.6 μm and 4.5 μm bandpasses, respectively. Blue and red bold lines on the TP profiles correspond to the FWHM of the weighting functions for the 3.6 μm and 4.5 μm channels.

tures and diverge at higher temperatures. We measure the residuals and standard deviations of the brightness temperatures to the best fit lines in three equally spaced temperature regimes (649K-1330K, 1330K-2012K, 2012K-2693K). At 4.5 μm the standard deviation of the residuals is 83K, 193K, and 258K, respectively, for the low, medium, and high temperature bins. At 3.6 μm they are 157K, 187K, and 242K. The standard deviation of the residuals increases with increasing temperature, following the trends predicted by the models with temperature inversions in Figure 3.3.

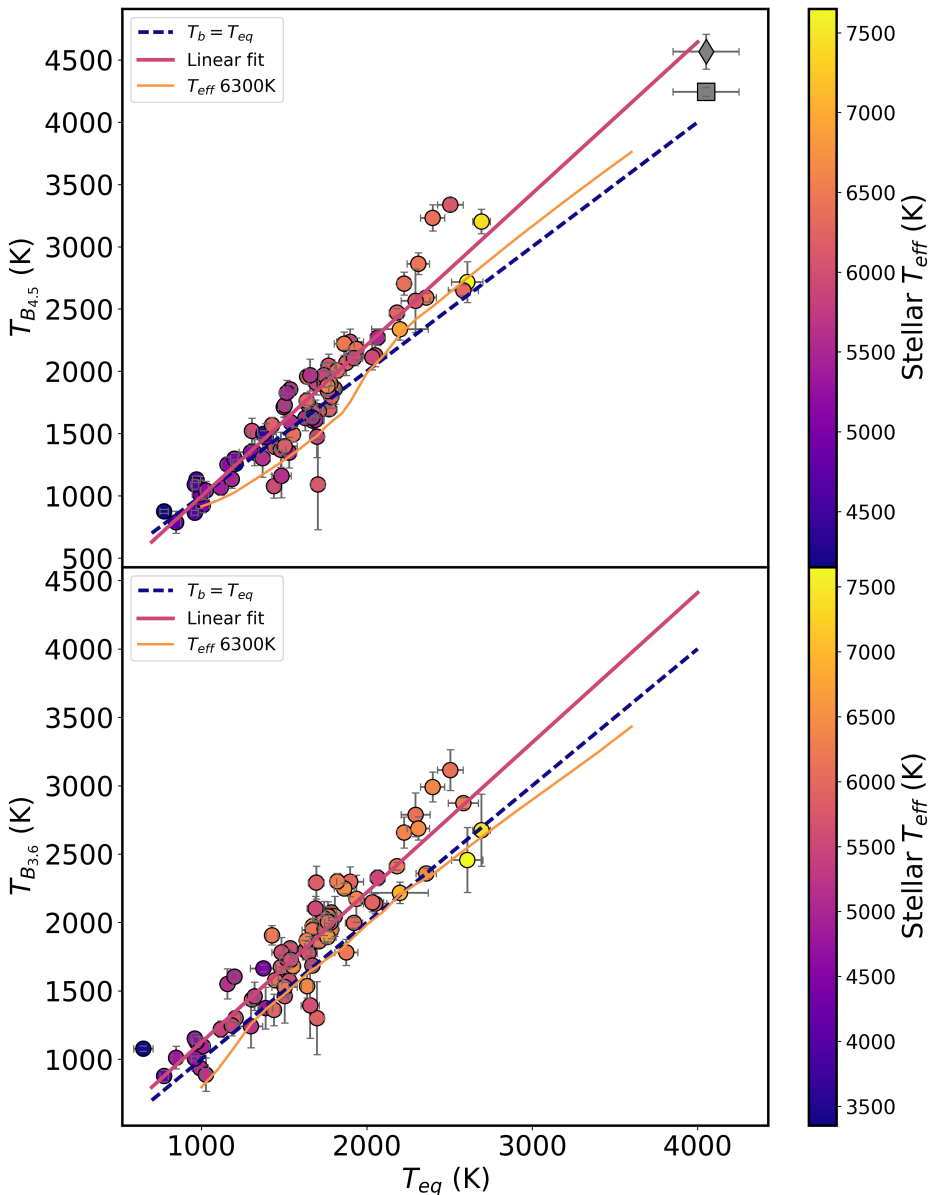


Fig. 3.3: Brightness temperatures vs $T_{eq,0}$ (full redistribution, 0 albedo) at 3.6 μm (bottom panel) and 4.5 μm (top panel). Magenta trend lines show a linear ODR fit to the data (gradient in the legends) and the blue dashed line shows the $T_B = T_{eq,0}$ slope (gradient of 1). The gray points are the 4.5 μm brightness temperatures of KELT-9b: the square is our analysis presented in Appendix 3.D, and the diamond is the analysis presented in Mansfield et al. (2020). Forward ScCHIMERA models are displayed in orange for one stellar effective temperature of 6300K

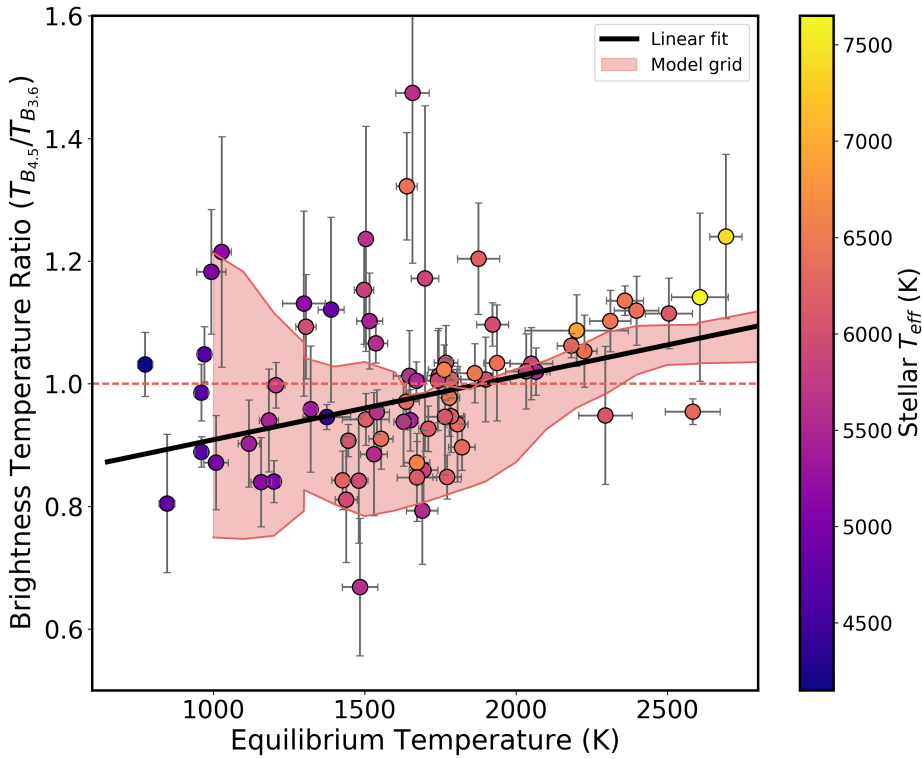


Fig. 3.4: Brightness temperature ratio ($T_{B_{4.5}}/T_{B_{3.6}}$) vs the equilibrium temperature ($T_{eq,0}$) of all of the available planets with secondary eclipses measured with Spitzer/IRAC. The blue line shows an ODR fit to the data with a slope significance of 3.1σ . Several functions were tested (see Section 3.4.2) and the model with the lowest BIC is plotted as a straight line. The orange shaded area shows the span of the ScCHIMERA model grid described in Section 3.3.4. The color scale is the effective temperature of the star.

Despite doing an eccentricity cut at an eccentricity of 0.2, there are still some planets with a nonzero eccentricity; these planets are typically outliers in Figure 3.3. Eccentric orbits result in stellar insulation changing throughout the planets orbit, and thus it is expected that their measured brightness temperatures deviate from standard equilibrium temperature calculations (which assumes a circular orbit).

3.4.2 Increasing trend in brightness temperature ratio versus equilibrium temperature

We demonstrate an increasing trend in the brightness temperature ratio with the $T_{eq,0}$ (Figure 3.4). This is a manifestation of the $4.5 \mu\text{m}$ individual brightness temperatures deviating more from equilibrium than $3.6 \mu\text{m}$ as seen in Figure 3.3. We fit the increasing trend, and find a

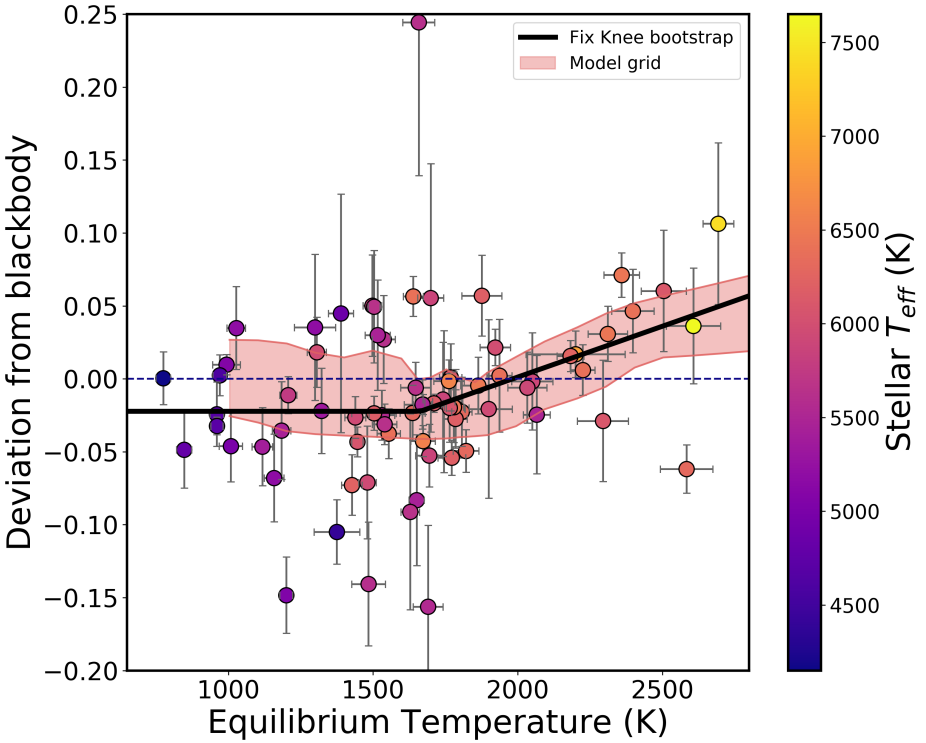


Fig. 3.5: Deviation of the $4.5 \mu\text{m}$ eclipse depth from the $3.6 \mu\text{m}$ blackbody propagated to $4.5 \mu\text{m}$ vs equilibrium temperature (computed with zero albedo and full redistribution). Several functions were tested (see Section 3.4.3) and the model with the lowest BIC is plotted as a bilinear with a knee. The color bar presents the stellar effective temperature. The dashed horizontal line indicates a zero deviation, meaning that the eclipses are consistent with a blackbody. The orange shaded area represents the span of the fiducial forward ScCHIMERA models described in Section 3.3.4.

slope of 95 ± 31 ppm per Kelvin for the PHOENIX models, which is significant to 3.1σ . In addition to the linear fit we also test a bilinear model, but we find that the change in the BIC does not favor this scenario. Finally, we make a comparison with our grid of forward models and find that they are consistent with the data.

3.4.3 Increasing trend in planetary deviation from a blackbody

Assuming that the planetary flux is a blackbody set at $3.6 \mu\text{m}$, we calculate the predicted eclipse depth at $4.5 \mu\text{m}$ and then calculate the deviation from the measured eclipse depth. Figure 3.5 presents this deviation as a function of the equilibrium temperature. We fit three different trend lines to the data and compare their Bayesian information criteria (BIC). First,

we fit a simple linear function (two free parameters), then we fit a bilinear model (four free parameters), and finally a bilinear model with the slope of the first line segment fixed to zero (three free parameters). The χ^2_{red} for the three models are 3.77, 3.51, and 3.50 and the BICs are 279, 261, and 259 for the straight line, bilinear, and fix bilinear, respectively. According to the Δ BIC and χ^2_{red} , the fixed bilinear model provides the best fit. This model captures a transition to the UHJs with an intercept of 1660 ± 100 K. We also show that the grid of emission models are consistent with the data and predict these trends.

3.5 Discussion

3.5.1 Summary of our main results

The 3.6 μm brightness temperatures are statistically consistent with $T_{eq,0}$ (Figure 3.3), but 4.5 μm shows a statistically significant increase in T_B compared to $T_{eq,0}$, which is seen as a continuum between the hot and ultra-hot planets. Additionally, the $T_{B_{4.5}}/T_{B_{3.6}}$ ratio also demonstrates a smooth continuous increase with $T_{eq,0}$ (Figure 3.4). We note that, with our larger sample size, different uncertainty calculation, and different stellar model correction, we support the results of the linear fit of the $T_{B_{4.5}}/T_{B_{3.6}}$ ratio in Garhart et al. (2020) to better than 0.3σ .

However, in addition to the metrics in previous studies, our work includes the deviation from a blackbody which shows evidence of a transition between the hot and the ultra-hot Jupiters (Figure 3.5) that is not captured in the brightness temperature ratio (Figure 3.4). The deviation from a blackbody is proportional to the difference between the two brightness temperatures, whereas Garhart et al. (2020) present the ratio of the brightness temperatures. The ratio of two constantly increasing values is also a constant, but their difference is not. This subtle mathematical difference between the two metrics is the reason why a transition is not captured by the brightness temperature ratio. A bilinear fit of the deviation from a blackbody is statistically favored, indicating that the UHJs are driving the transition. This transition is also captured in our new grid of 1D self-consistent models (see Section 3.5.3). The 3.6 and 4.5 μm phase curve results of 12 hot Jupiters presented in Keating et al. (2019) tentatively support this transition in thermal structure. They visually demonstrate a difference in the temperature structures between the coolest and the hottest planets by plotting the difference in the two dayside brightness temperatures. We interpret below these trends and transitions in terms of temperature inversions and efficiency of redistribution.

3.5.2 Expected opacities at 3.6 μm and 4.5 μm

The dominant absorbers at the wavelengths probed by Spitzer/IRAC are methane (3.6 μm), carbon monoxide (4.5 μm), and water (both wavelengths). Parmentier & Crossfield (2018) and Lee et al. (2012) provide temperature–pressure profiles and the corresponding contribution functions for their analysis of emission spectra of WASP-121b (2400 K) and HD189733b

(1200 K). Despite the different temperature regimes, the $4.5 \mu\text{m}$ contribution function probes lower pressures than $3.6 \mu\text{m}$. This is driven by the bimodality at $4.5 \mu\text{m}$ caused by the H₂O deeper in the atmosphere (~ 30 mbar) and higher CO/CO₂ at lower pressures ($\sim 2-3$ mbar), whereas $3.6 \mu\text{m}$ probes ~ 40 mbar.

The transition between the dominating carbon-bearing species in hot Jupiters is expected to occur at around 1000K (e.g., Zahnle & Marley 2014; ?; Molaverdikhani et al. 2019), with hotter atmospheres becoming dominated by CO. Consequently, any changes in the structure of the T-P profile would be seen at $4.5 \mu\text{m}$ due to the presence of CO (Fortney et al. 2008; Parmentier & Crossfield 2018; Arcangeli et al. 2018). Specifically, a temperature inversion would result in CO in emission, increasing the $4.5 \mu\text{m}$ brightness temperature compared to $3.6 \mu\text{m}$. As the planets approach the ultra-hot temperature regime, water and most other molecular species should begin to dissociate, except the CO. This will further increase the difference in the two pressures probed by Spitzer, making our observations even more sensitive to possible temperature inversions.

More generally, the peak of the Planck function corresponding to the thermal emission of the planet shifts at shorter wavelengths when the effective temperature of the planet dayside increases. Since the opacities generally increase with increasing wavelength, the difference between the opacities at the continuum and either of the Spitzer wavelengths then increases with increasing equilibrium temperature. The overall opacity of an atmosphere increases from $\sim 1 \mu\text{m}$ to $10 \mu\text{m}$, mostly due to water. Therefore, any difference (positive or negative) between our measured T_B and $T_{eq,0}$ will be larger for hotter planets, as demonstrated in Figure 3.3. However, the relative difference in the water opacity between the two Spitzer wavelengths is small enough that we do not expect the Planck function shift to be playing a role when comparing the brightness temperatures to each other (e.g., Figures 3.4 and 3.5). Differences between the two Spitzer wavelengths are dominated by the CO opacity at $4.5 \mu\text{m}$.

3.5.3 Grid of forward models

In Figure 3.2 we plot the range of 1D models from the emission model grid for three different stellar temperatures (4300K top row, 5300K middle row, and 6300K bottom row). We can see that, for each model track, as the equilibrium temperature increases, the atmosphere switches from being non-inverted to being inverted. This causes the strong CO emission feature in the $4.5 \mu\text{m}$ bandpass to emerge. The hotter the equilibrium temperature of the planet, the stronger the temperature inversion, and the stronger the CO emission feature. We note that we also see the CH₄ absorption feature appearing as a dip in the brightness temperatures at $3.6 \mu\text{m}$ for the coolest (non-inverted) models. The trend from hot to cold is from a weakening inversion until finally the TiO and VO condense out, with a very small isothermal transition region, as can be seen in the grid model T-P profiles displayed in Figure 3.2.

Additionally, Figure 3.2 demonstrates that as the effective temperature of the star increases, the atmosphere of the planet with a given equilibrium temperature has a stronger inversion than a planet with the same temperature does around a cooler star. This is in part

because at a given planetary temperature, the wavelength separation between the stellar spectrum and the planetary spectrum increases for hotter stars, which results in a higher effective visible-to-infrared Planck mean opacity. The atmosphere of the planet may respond differently to these fluxes, resulting in different temperature pressure profiles.

We compare the complete sample of eclipses to our grid of 1D emission models for the individual planetary brightness temperatures, for which a subset is plotted in Figure 3.2. We highlight that since most of the hottest ($T_{eq,0} > 2000K$) planets in our sample have stellar temperatures $> 5900K$ they should be modeled by the 6300K track. We plot modeled tracks corresponding to planets around a 6300K star on Figure 3.3. We find that the temperatures we measured for our survey planets are higher than expected from the model tracks. We interpret this as being due to the model equilibrium temperature assuming full uniform redistribution, whereas these planets are likely tidally locked and thus will have hotter daysides. However, we do find that the models capture the stronger deviation between brightness and equilibrium temperatures at $4.5 \mu\text{m}$ compared to $3.6 \mu\text{m}$ for hotter planets.

We use the full grid of emission models (see Section 3.3.4) for comparison with the deviation measured in channel 2 ($4.5 \mu\text{m}$) from the blackbody estimated from channel 1 ($3.6 \mu\text{m}$) and with the brightness temperature ratio (Figure 3.5 and Figure 3.4 respectively). First, we find that the model grid is consistent with both of the trends we measured from the data. The models show a clear transition at $\sim 1700K$, which is consistent with the transition temperature we fit from the data in Figure 3.5. Second, the envelope of models do not show the same abrupt transition at $\sim 1700K$ in the brightness temperature ratio (Figure 3.4) as they do in the deviation from the blackbody. Instead, they show a continuous increase with equilibrium temperature, with significant variations at the lower temperatures, which is in agreement with the data and the straight line we fit in Section 3.4.2.

We find that the spread in the models for both the deviation from the blackbody (Figure 3.5) and the brightness temperature ratio (Figure 3.4) is primarily caused by differences in metallicity and C/O ratio, with surface gravity and stellar temperature having little effect here. Thus, using the grids of different C/O ratios we are able to evaluate trends from the whole population. We find that we can rule out tracks with a high C/O ratio of 0.85 ($\Delta\text{BIC} \approx 270$), meaning that the population of hot Jupiters statistically favors low or solar C/O ratios ($\text{C}/\text{O} \leq 0.54$). This means that high C/O planets are rare ($\text{C}/\text{O} \geq 0.85$).

3.5.4 Interpretation of the transition from hot Jupiters to ultra-hot Jupiters

3.5.4.1 Assumptions on albedo, redistribution, clouds, and thermal structure

We compute the equilibrium temperature ($T_{eq,0}$) assuming full redistribution and null Bond albedo, see Section 3.3.3. Changing these assumptions would have an effect on our results. A nonzero albedo would result in the predicted theoretical equilibrium temperature being lower than $T_{eq,0}$, and relaxing the full redistribution assumption would increase the predicted equilibrium temperature toward $T_{eq,max}$ (no redistribution). This likely explains the few cooler

planets whose brightness temperatures are lower than the equilibrium temperature (Figure 3.3).

In Figures 3.3 and 3.4, we find a continuous increase in the brightness temperature with $T_{eq,0}$, with the hottest planets being even hotter than the predicted equilibrium temperature, especially at $4.5\text{ }\mu\text{m}$. Empirical estimates of the Bond albedo for hot Jupiters and ultra-hot Jupiters range from 0 to 0.3 (Schwartz & Cowan 2015; Schwartz et al. 2017). A nonzero albedo would statistically lower T_{eq} below $T_{eq,0}$, which in turn would strengthen the deviation seen. Furthermore, Figure 3.3 demonstrates that the increase in brightness temperatures with equilibrium temperature is also predicted by the models that assume zero albedo and full redistribution. Increasing the albedo in the models would also strengthen this deviation. We thus do not think our zero albedo assumption changes these trends.

On the other hand, a lower redistribution efficiency for the hottest planets would increase their T_{eq} , resulting in hotter brightness temperatures. However, a compilation of Spitzer phase curves shows no trend with the difference of the phase curve offsets at the two Spitzer wavelengths (Beatty et al. 2019; Zhang et al. 2018). This provides no evidence for potential different redistribution in the two IRAC bandpasses, and we would thus expect the deviation to be equal at the two wavelengths; however, this is not observed (Figure 3.3). We hypothesize that a broader range of redistribution efficiencies for the hotter planets could explain the increasing scatter with increasing $T_{eq,0}$ in Figure 3.3. The degree to which hot Jupiters redistribute heat has been known to vary from planet to planet (Showman & Guillot 2002; Cowan et al. 2007; Cowan & Agol 2011b; Knutson et al. 2007; Showman & Polvani 2011).

Figure 3.5 shows a transition at $T_{eq} \approx 1700\text{K}$ in the dayside emission of our sample of 78 hot Jupiters. We find a similar transition in the new model grid described in Section 3.3.4. Dayside clouds made of large particles could, in theory, equalize the brightness temperature at 3.6 and $4.5\text{ }\mu\text{m}$; however, we do not think that a transition from cloudy to cloud-free is a likely explanation for the trend seen in Figure 3.5. The main reason for this is that a large majority of hot Jupiters show very low geometric albedos in optical wavelengths, indicative of daysides that are not significantly dominated by cloud opacity. Second, if clouds made of small particles ($\sim 1\mu\text{m}$) were dominating the opacity structure in the Spitzer bandpasses, they would be even more dominant in the Hubble Space Telescope wide field camera 3 (HST/WFC3) bandpass. However, the two emission spectra of hot Jupiters (not ultra-hot) taken with the HST/WFC3 and with a good enough signal to noise ratio (HD209458b and WASP-43b) show evidence of water absorption and not the blackbody emission expected from a cloudy dayside (Line & Parmentier 2016; Stevenson et al. 2014a). Additionally, clouds composed of reflective species would create large shifts in the optical phase curves Shporer & Hu (2015). In searching for these large shifts in phase curves measured with the Kepler telescope, there is evidence that clouds could be present in only a tiny fraction of the dayside (Parmentier et al. 2016). Based on this range of evidence, we consider it reasonable in this paper to model the daysides of planets with $T_{eq} > 1400\text{K}$ as being cloud-free.

We conclude that the main cause of the increase in brightness temperature with equilibrium temperature and of the increasing deviation from a blackbody is indeed physical, and

is not due to our assumptions of the albedo, redistribution, or cloud-free atmosphere when calculating the equilibrium temperature.

3.5.4.2 Transition in thermal inversions

The strength of the deviation from blackbody calculation (Figure 3.5) is that it is free of re-distribution and albedo assumptions; it simply compares $4.5\text{ }\mu\text{m}$ to $3.6\text{ }\mu\text{m}$. Theoretically, the positive deviation from blackbody could be emission by CO at $4.5\text{ }\mu\text{m}$ (inverted T-P profile) or absorption by methane at $3.6\text{ }\mu\text{m}$ (non-inverted T-P profile). However, given equilibrium chemistry, methane is very unlikely to be in the hottest atmospheres. Moreover, three of our hottest planets have already been shown to have temperature inversions: WASP-33b, WASP-121b, and WASP-18b (Haynes et al. 2015; von Essen et al. 2015; Evans et al. 2017; Arcangeli et al. 2018; Kreidberg et al. 2018a). Furthermore, the best fitting model is bilinear with an intercept of $1660 \pm 100\text{K}$, highlighting the statistical power of the UHJ deviation. Our grid of forward models also predict a curve that is similar to this bilinear fit, capturing the location of the intercept of the two lines at $\sim 1700\text{K}$.

Interestingly, this corresponds to the condensation temperatures of TiO and VO, which could be the origins of thermal inversions (Hubeny et al. 2003; Burrows et al. 2007; Fortney et al. 2008). We thus interpret that this deviation represents the transition to a different physical realm in these atmospheres, for example as the temperature approaches that of the UHJs, atmospheres transition from non-inverted to inverted. For the cooler hot Jupiters, temperature inversions are suggested to be caused by the absorption of optical incoming stellar irradiation by gas phase TiO and VO (Hubeny et al. 2003; Fortney et al. 2008). On the other hand, for UHJs, inversions can form through other absorbers such as Na/FeH/Fe/Fe+/Mg (e.g Lothringer et al. 2018; Pino et al. 2020) or from lack of cooling due to molecular dissociation (Parmentier & Crossfield 2018). As molecular dissociation occurs, H- becomes an important opacity source, leading to blackbody-like emission spectra, as seen in HST/WFC3 near $1.4\text{ }\mu\text{m}$ (e.g., Arcangeli et al. 2018). WASP-12b is the biggest outlier in Figure 3.5 (it has the lowest deviation from a blackbody for planets with $T_{eq} > 2500$), but this planet is thought to have potential mass loss, and so our considerations may not apply to it directly (Cowan et al. 2012; Bell et al. 2019).

In Figure 3.3 we observe a stronger deviation from equilibrium temperature at $4.5\text{ }\mu\text{m}$ compared to $3.6\text{ }\mu\text{m}$. We interpret that at $4.5\text{ }\mu\text{m}$ we see CO in emission, whereas at $3.6\text{ }\mu\text{m}$ there is a weaker emission feature from non-dissociated H₂O originating deeper and cooler in the atmosphere. This is also captured by the grid of models, especially for the hot stars which represent the majority of the deviating planets. However, in Figure 3.3 there is a systematic discrepancy between the models and the data which is not captured in Figure 3.5 (i.e., our fitted lines lie lower than the models predict). Our interpretation for this discrepancy and for the intrinsic scatter of the brightness temperatures is that it is either due to the difference in strength of the inversions or that the models are not capturing all of the underlying physics. For example, these models do not account for atmospheric drag (e.g., Arcangeli et al. 2019)

or assume that stratospheres are cloud-free. Moreover, whatever the effect is, it does not appear to correlate uniquely with stellar insolation since planets with similar equilibrium temperatures can exhibit different strengths of deviation.

KELT-9b is the hottest known transiting exoplanet and is thus a great probe of the extreme scenarios that we have already discussed above. In Appendix 3.D we measure the $4.5\text{ }\mu\text{m}$ eclipse depth of KELT-9b from an observation centered around eclipse and lasting three times the eclipse duration. We compare this with the results of Mansfield et al. (2020) who use the full phase curve observation. Our brightness temperature is 4.6σ lower than the value calculated in Mansfield et al. (2020), which is likely due to the underestimation of the eclipse depth in our modeling since we approximate the concave down phase variation with a linear function; this discrepancy has been studied before (e.g., Bell et al. 2019). Nevertheless, we plot both T_B on Figure 3.3 and find that both follow the trend of increasing T_B with T_{eq} . In particular, the brightness temperatures calculated from the phase curve in Mansfield et al. (2020) agree with our fitted trend line to $<1\sigma$. However, both brightness temperature calculations are cooler than an extrapolation of the model grid might suggest. We hypothesize that this is due to possible partial CO dissociation, given the ultra-hot equilibrium temperature of KELT-9b, resulting in lower CO emission in the $4.5\text{ }\mu\text{m}$ dayside observation (e.g., Kitzmann et al. 2018; Lothringer et al. 2018). A dedicated modeling analysis would be necessary to confirm this hypothesis, which is beyond the scope of this work.

In summary, our work demonstrates that a transition exists in the infrared emission spectra between hot Jupiters and ultra-hot Jupiters and that this is likely due to a change between non-inverted and inverted temperature-pressure profiles as the stellar irradiation increases on these planets.

3.6 Clues from HST/WFC3

Our knowledge of the physics occurring at the IRAC bandpass is deeply influenced by our knowledge of the spectrally resolved HST/WFC3 bandpass. We combine our Spitzer survey with available HST/WFC3 data from the literature and discuss the deviation from the blackbody in the context of the water feature at $1.4\text{ }\mu\text{m}$ in the HST/WFC3 spectral band. Figure 3.6 shows the deviation from the blackbody calculated at the Spitzer wavelengths (right panel). This is combined with the individual Spitzer emission photometry and the HST emission spectra for a subsample of the available planets (middle and left panels respectively).

We see a continuum between the coolest and the hottest hot Jupiters. The hottest planets in our sample (WASP-33b and WASP-18b) have blackbody-like spectra in HST/WFC3 caused by the H- opacity (Arcangeli et al. 2018), and they show signs of a temperature inversion in Spitzer. HAT-P-32Ab is centered in the middle of the deviation from a blackbody plot, exhibiting no absorption or emission of CO, and shows a similar (albeit noisier) blackbody emission spectrum with WFC3 (Nikolov et al. 2018). Finally, as we approach the coolest planets in HST (HD209458b and WASP-43b $\sim 1500K$), we see the water feature appearing

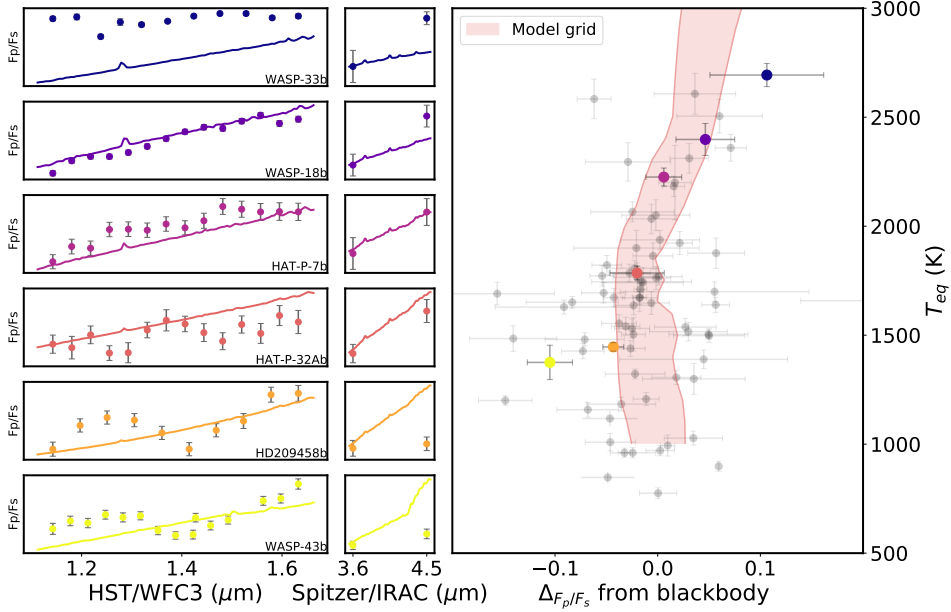


Fig. 3.6: Right panel: Deviation from the blackbody in the Spitzer bandpass against equilibrium temperature. Planets here demonstrate the continuous transition between the hot and the ultra-hot planets. Several planet with available HST spectra are highlighted and their spectra are plotted in the left (HST/WFC3) and middle (Spitzer) panels. These planets are color-coded by increasing temperature. For simplicity and clarity, we show only six of the HST spectra as examples. The models shown in the left and middle panels are the blackbody at $T_{b3.6}$ and PHOENIX model ratio emission spectra. The model overplotted on the rightmost panel is the emission model grid described in Section 3.3.4.

strongly in absorption. For these planets we see a negative deviation from the blackbody in Spitzer. We interpret this negative deviation as CO in absorption at $4.5 \mu\text{m}$ since at these cooler temperatures we expect to have non-inverted TP profiles. We highlight that our grid of models predicts these observations.

Building on the color-magnitude work of Triaud (2014) we also create a color-color diagram, where we use the difference between two brightness temperatures. Figure 3.7 shows the Spitzer color plotted against the HST color. The HST/WFC3 color is designed to capture inside and outside the water feature at $1.25 \mu\text{m}$ and $1.4 \mu\text{m}$. We also show horizontal and vertical dashed lines representing blackbodies for each regime as well as the fiducial model track from our forward model grid ($T_{eff} = 5300\text{K}$, C/O=0.54, $[\text{M}/\text{H}] = 0$, $\log(g)=3.0$). Following the increasing temperature of the model track demonstrates the manifestation of the changing TP profiles (seen in Figure 3.2). The Spitzer color (horizontal axis), becomes larger as the models switch from exhibiting CO in absorption to CO in emission, whereas the HST color is slightly more complicated (vertical axis). First, there is a group of models around

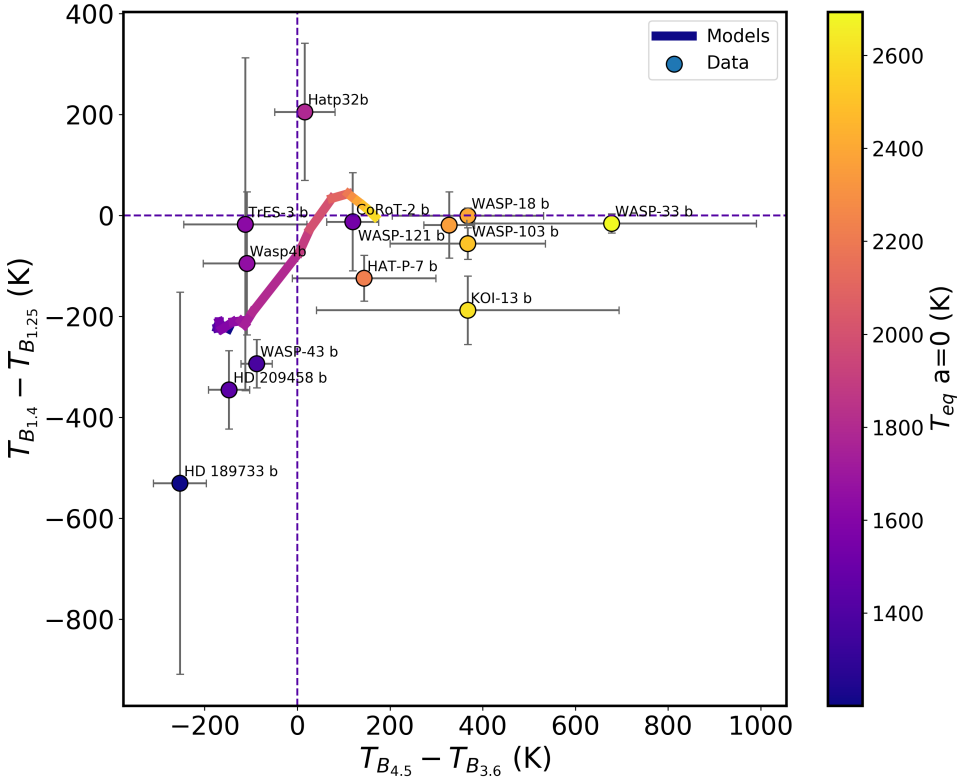


Fig. 3.7: Color-color plot of the planets with available HST spectra. We calculate the color as the difference between the brightness temperatures in and out of the water feature in HST and as the difference between the brightness temperatures in the Spitzer bandpass.

-200K (both axes) with negative colors, capturing the strong water absorption feature. This is followed by an increase toward a blackbody as the strength of the water feature decreases (-120K to +50K on the X-axis) and the atmospheres begin to transition toward thermally inverted with a slightly positive HST color, up to ~ 50 K. Finally, beyond a mid-IR color of +100K, the model HST colors become consistent with blackbodies again as the water feature disappears as the H- opacity takes over.

In the available data, we note a clear gap in measured planetary temperatures (between HAT-P-7b (2225K) and HAT-P-32Ab (1785K)) where we expect to be probing the transition, which allows us to split the data into two families. The hotter sample planets (> 1785 K) have an average Spitzer color of 350K and exhibit less variance in the HST color, which captures the CO in emission at $4.5 \mu\text{m}$ and of their blackbody-like features in HST. Instead, the cooler sample planets (≤ 1785 K) have an average Spitzer color of ~ 80 K, indicative of CO in absorption at $4.5 \mu\text{m}$. Furthermore, the cooler sample follows the increasing model track as the strength of the water feature becomes less strong. Thus, our data largely follow

the trends predicted by the models in both HST and Spitzer wavelengths, and we find that the published sample of HST data supports our claim of a continuum to the ultra-hot Jupiters. An analysis of an expanded dataset including new HST/WFC3 emission spectra for transiting giant planets will be presented in a forthcoming paper (Mansfield et al., in prep.).

3.7 Conclusions

We present our analysis of a literature survey of 78 hot Jupiters with secondary eclipses observed with Spitzer at $3.6\text{ }\mu\text{m}$ and $4.5\text{ }\mu\text{m}$. Our survey spans equilibrium temperatures (zero albedo and full redistribution) between 800K and 2700K. We tested different stellar models (blackbody, ATLAS, PHOENIX) in order to correct the stellar flux from the secondary eclipse depths, and found that improper treatment of the star could bias results, particularly for planets around hotter stars. We then calculated the brightness temperatures at the two Spitzer wavelengths by using PHOENIX models to correct the stellar flux, by inverting the Planck function and integrating over the Spitzer spectral responses.

We find that the brightness temperatures at $4.5\text{ }\mu\text{m}$ are increasingly hotter than equilibrium temperature predictions for the hotter planets, which we interpret as a result of seeing CO in emission at $4.5\text{ }\mu\text{m}$ due to the temperature inversions in combination with the Planck function shift. The Planck function of a planetary atmosphere shifts to shorter wavelengths for higher temperatures, increasing the difference between the pressures probed by the equilibrium temperature and the pressures probed by Spitzer, and thus the magnitude of the difference between the brightness temperature and equilibrium temperature will be larger for hotter planets. However, we note that any differences between $3.6\text{ }\mu\text{m}$ and $4.5\text{ }\mu\text{m}$ are going to be dominated by the strong CO band at $4.5\text{ }\mu\text{m}$.

We confirm a previous finding that the $T_{B_{4.5}}/T_{B_{3.6}}$ ratio exhibits a smooth continuum increasing with $T_{eq,0}$. However, we also measure, for the first time, the deviation of the data from the blackbody, which we defined as the difference between the observed $4.5\text{ }\mu\text{m}$ eclipse depth and the eclipse depth expected at $4.5\text{ }\mu\text{m}$ based on the brightness temperature measured at $3.6\text{ }\mu\text{m}$. We find a transition at an equilibrium temperature of $1660 \pm 100\text{K}$ in the deviation of the data from a blackbody.

We compare our result to a new grid of 1D self-consistent models (ScCHIMERA) which contain the appropriate physics for temperature inversion formation. We find that the model grid is consistent with both of the trends we measured from the data; in particular, we find an excellent agreement between our measured transition and what is expected from the models. We suggest that this transition is capturing a change in the temperature pressure profile of these atmospheres, from non-inverted to inverted atmospheres as the stellar irradiation increases on these planets.

We find that the spread in the models for the deviation from the blackbody and for the brightness temperature ratio is primarily caused by differences in metallicity and C/O ratio, with surface gravity and stellar temperature having little effect here. We rule out tracks with

a high C/O ratio (0.85), meaning that the population of hot Jupiters statistically favors low or solar C/O ratios ($C/O \leq 0.54$), and that high C/O planets are rare ($C/O \geq 0.85$).

3.A Details of the data analysis

3.A.1 Fitting correlations with x and y errors

Fitting of linear functions is often done using an ordinary least squares (OLS) or Markov chain Monte Carlo (MCMC) method, both of which assume Gaussian errors. However, our data has errors on both the abscissa and the ordinate, meaning a simple OLS cannot be performed (Hogg et al. 2010). We opted for the *scipy.odr* package, translated from the FORTRAN-77 ODRPACK by ?. ODRPACK is a weighted orthogonal distance regression function which takes into account errors on x and on y by minimizing the weighted orthogonal distance between the observations and the model. However, as pointed out in Beatty et al. (2019), ODRPACK uses relative errors between the data points, meaning that the resulting covariance matrix remains the same even when you multiply all of the individual errors by some factor. This has the potential for producing incorrect uncertainties on the parameters. Beatty et al. (2019) use another package, bivariate correlated errors and intrinsic scatter (BCES) (Akritas & Bershady 1996; Nemmen et al. 2012). However, this package only fits a linear model, and so is not suitable for our cases.

Furthermore, these regression methods rely on the assumption that the model perfectly captures the data and that the data are drawn from a purely Gaussian distribution (e.g., ??). In our case, we know that both of these assumptions are not true, and that estimating errors from the covariance matrix could result in underestimated uncertainties. We thus decide to sample the parameter space using bootstrapping. Bootstrapping estimates posterior distributions by repeatedly resampling with replacement and refitting the function (?). We use ODR to fit the function, accounting for errors on x and y, and then we bootstrap to obtain parameter distributions. Our parameter estimates are then quoted as the 16th, 50th, and 84th percentiles on the marginalized parameter distributions.

When measuring the slope of brightness temperature ratio against equilibrium temperature, we find a slope of 95 ± 31 ppm, which has a significance of 3.1σ , see Section 3.4.2. This is consistent but slightly less significant than 4σ the result presented in Garhart et al. (2020) (98 ± 26), despite our larger sample size. We test our method with their sample and still cannot reproduce their accuracy. We thus expect that the difference is simply due to the fitting and sampling methods chosen. Garhart et al. (2020) use a Gibbs MCMC sampler assuming Gaussian errors based on methods described in Kelly (2007), whereas our bootstrap method does not assume that the errors are Gaussian, and thus end up with broader posterior distributions for our parameters.

Table 3.1: We measure the gradient of temperature vs irradiation temperatures for three different temperatures: the individual brightness temperatures ($T_{b_{3.6}}$ and $T_{b_{4.5}}$) and the dayside effective temperature (T_{day}), calculated as a weighted mean. Each set of temperatures is calculated using three different stellar models: blackbodies, ATLAS models, and PHOENIX models. Figure 3.3 displays the individual brightness temperatures for PHOENIX models and Figure 3.8 displays the effective temperatures.

	T_{eff}	$T_{b_{3.6}}$	$T_{b_{4.5}}$
BB	0.85 ± 0.03	0.81 ± 0.05	0.92 ± 0.05
ATLAS	0.80 ± 0.03	0.79 ± 0.04	0.84 ± 0.04
PHOENIX	0.80 ± 0.03	0.76 ± 0.05	0.84 ± 0.05

3.B Importance of using stellar models

The calculation of the brightness temperature requires an assumption of the stellar model in order to disentangle the planetary flux from the measured planet-to-star flux ratio (F_p/F_s). The simplest assumption is to model the star as a blackbody using the Planck function; however, it is also possible to use a grid of synthetic stellar models. For the first time, to our knowledge, we use our survey to test three different types of models for the star: blackbodies, ATLAS models (Kurucz 1979), and PHOENIX models (Allard & Hauschildt 1995; Husser et al. 2013).

For ATLAS models we use the ATLAS9 version of the code (Castelli & Kurucz 2003). This assumes steady-state plane-parallel layers in local thermodynamic equilibrium (LTE), and opacities that are treated by averaging the contribution of different molecular and/or atomic species resulting in a line blanketing effect. Conversely, the PHOENIX models assume spherical geometry and direct opacity sampling of molecular and atomic species. They are also computed under the LTE assumption; however, non-local thermodynamic equilibrium (NLTE) effects are included for the spectral line profiles of selected important species (Li I, Na I, K I, Ca I, Ca II).

3.B.1 Effect of different stellar models on measured temperature

Comparing the gradients (presented in Table 3.1) of each set of brightness and effective temperatures quantifies the difference between the stellar models. For the effective temperature we can see that the ATLAS and PHOENIX models are consistent with each other at better than 1σ level; however, blackbodies are systematically $\sim 2\sigma$ above the stellar models. This larger gradient was also seen in Schwartz & Cowan (2015) with their sample, where they measured a value of 0.87(5) for the effective temperature. If any of these temperature sets were to be representative of the equilibrium temperature then the expected gradient would be 0.71 ($T_{eq} = (1/4)^{1/4}T_0 = 0.71T_0$). The Schwartz & Cowan (2015) of 0.87(5) is statistically significantly steeper than 0.71, which they interpreted as hotter planets having a low Bond albedo and/or less efficient heat transport in their atmospheres. However, the gradient displayed in Table 3.1 shows that this could also be an effect of the use of blackbodies to correct

the stellar flux, and thus blackbodies cannot be excluded as the cause of their deviation.

A similar result is seen in the individual brightness temperatures, whereby ATLAS and PHOENIX models are consistent with each other. Thus, for statistical studies of the planets with a wide range of temperatures, using blackbodies for the star can be misleading. We therefore decided to use stellar models to correct the stellar flux from eclipse measurements of our sample of hot and ultra-hot Jupiters. PHOENIX models have some advantages over other stellar models; they are computed at a higher resolution, span a larger range of temperatures, and contain direct opacity sampling. Additionally, PHOENIX models also account for some NLTE effects, which has been shown to be important for ultra-hot planets (Lothringer & Barman 2019). Thus, we decided to use PHOENIX models instead of ATLAS for the remainder of the analysis.

We also found that integrating over the spectral response increases the measured flux compared to taking the exact flux density at the average wavelength of the Spitzer band pass, as is done in Schwartz & Cowan (2015). This is due to the nonlinear slope of both the stellar and planetary models over the bandpass, see Figure 3.B. We calculate that ignoring this effect could lead to planetary brightness temperatures overestimated by as much as 115K at $3.6\text{ }\mu\text{m}$. This effect is more prominent where the slope of the spectra are steeper (e.g., at $3.6\text{ }\mu\text{m}$ compared to $4.5\text{ }\mu\text{m}$ or for hotter planets and stars). On average, for the whole sample, without integration we calculate overestimation of 32K at $3.6\text{ }\mu\text{m}$ and 14K at $4.5\text{ }\mu\text{m}$. Thus, if not accounted for, this could enhance or diminish any statistical differences seen when comparing $3.6\text{ }\mu\text{m}$ and $4.5\text{ }\mu\text{m}$. Additionally, we find the hottest planets in our survey around the hotter stars. Thus, when looking for trends throughout a wide range of temperatures, it is imperative to carefully correct for the stellar flux to ensure that what we are seeing is a result of the planetary atmosphere.

We find the trend in the brightness temperature ratio with equilibrium temperature to be 99 ± 37 ppm with blackbodies 97 ± 35 ppm with ATLAS models and 95 ± 31 ppm with PHOENIX models (Section 3.4.2). The maximum difference between the significance of these slopes for all of three stellar models is negligible, which suggests that any importance of stellar models vanishes somewhat when looking at the ratios. Nevertheless, we keep the results from the PHOENIX models (Section 3.4.2).

3.C Comparing effective temperatures with Schwartz & Cowan (2015)

Schwartz & Cowan (2015) measure the slope of the effective dayside temperature against the irradiation temperature. They note that their slope 0.87 ± 0.05 is significantly steeper than equilibrium temperature predictions (0.71), and that this increasing deviation could lower redistribution efficiencies in the hottest planets. We recreate their results with our expanded survey. We follow their method for calculating the effective temperature, which is the weighted mean of the brightness temperatures, and thus we call it $\langle T_B \rangle = (T_{b_{3.6}}/\sigma_{3.6}^2 + T_{b_{4.5}}/\sigma_{4.5}^2)/2$.

We then fit the resulting trends with an ODR (see Section 3.A.1). However, first we test their method of brightness temperature calculation of inverting the Planck function and using a blackbody for the star. Then we test our method using a stellar model and fully integrating the Planck function.

Figure 3.8 presents the results for weighted mean effective temperature using the PHOENIX model calculations of the brightness temperatures. We find a slope of 0.76 ± 0.05 , which is consistent with equilibrium temperature (1σ) and inconsistent with the 0.87 ± 0.05 of Schwartz & Cowan (2015). However, with brightness temperatures calculated without integration over the bandpass and with blackbodies for the star we are able to retrieve a slope of 0.81 ± 0.05 , which is in statistical agreement (0.9σ) with their trend.

Since we are able to retrieve the results using blackbodies, we conclude that the discrepancy is a result of careful use of stellar models and integration over the bandpasses and not of the differences in the sample sizes. More importantly, our findings do not support the findings presented in Schwartz & Cowan (2015) as we do not find that the effective temperature trend with irradiation temperature increases disproportionately. This means that we do not think the effective temperature calculated in this way tells us anything about the redistribution in the hottest planets. On the other hand, in Figure 3.3, we find that the $4.5 \mu\text{m}$ brightness temperature is deviating from equilibrium, likely due to the strong CO opacity appearing in emission. This does support the hypothesis that these hottest planets are exhibiting different behaviors, but it is not expected to be captured in the effective temperatures since the weighted mean of the two brightness temperatures is likely muting this deviation.

3.D KELT-9b Eclipse: the hottest of the UHJs

A question arises of whether the trends presented in Section 3.5 hold at even higher temperatures. To test this we include the $4.5 \mu\text{m}$ eclipse depth of the hottest of the UHJs, KELT-9b (Gaudi et al. 2017). Significantly hotter than any other ultra-hot Jupiter, KELT-9b is the hottest gas giant planet known. A 1.48-day orbital period around its A-type host star of 10170K makes it the most highly irradiated planet with an equilibrium temperature of 4050K (Gaudi et al. 2017). At these temperatures, the planet itself is similar to a K4 star; its atmosphere is subject to molecular dissociation, leaving behind atomic metals such as iron and titanium (Hoeijmakers et al. 2018, 2019).

We analyse two $4.5 \mu\text{m}$ eclipses of KELT-9b. The data were taken from the phase curve survey, program ID 14059 lead by PI J Bean. We extracted the two secondary eclipses from the available phase curves. The analysis from raw data to eclipse depth values was done using our custom pipeline described in Baxter et al. (in prep.). In summary, we allow for different background correction methods, different centroiding methods, and different aperture radii to find the combination that gives the lowest χ^2 . We correct for the strong Spitzer systematics using Pixel Level Decorrelation (Deming et al. 2015) and perform a full MCMC analysis using Batman (Kreidberg 2015) to fit for the eclipse parameters on the best photo-

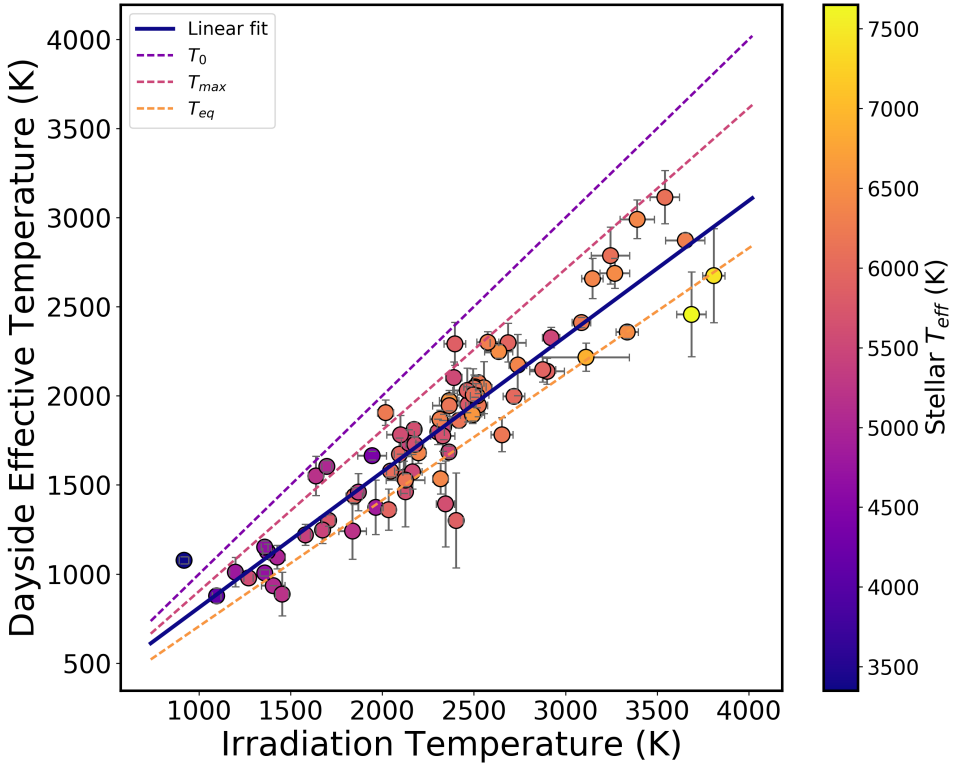


Fig. 3.8: Dayside effective temperature ($< T_B >$) vs the theoretical irradiation temperature (T_{eq}) with zero albedo and full redistribution, similar to Schwartz & Cowan (2015), but with 28 more planets. We also plot the expected irradiation temperature (T_0), the equilibrium temperature with zero albedo (T_{eq}), and the maximum dayside temperature (T_{max}). The color scale is the effective temperature of the host star in Kelvin.

metric lightcurve. The raw photometry, the corrected lightcurves, and one of our statistical tests (RMS vs binsize, which characterizes how well we correct red noise) are presented in Figure 3.9. The two eclipse depths (F_p/F_s) are calculated to be 2793 ± 44 (ppm) and 2809 ± 48 (ppm) for AORs r67667712 and r67667968, respectively. The eclipse depth used in the analysis is the mean of these two values 2801 ± 33 (ppm). This eclipse depth is used to calculate the brightness temperatures shown in Figure 3.3.

Our results disagree with the $4.5\mu m$ eclipse depths presented in Mansfield et al. (2020) by 4.6σ . This significant difference is likely not due to any problems with the systematic correction algorithm, but is rather a result of the choice of baseline between eclipse and phase curve observations. Eclipse-only observations ignore phase variations, and can thus underestimate eclipse depths when the real phase variations are concave over the secondary eclipse (e.g., Bell et al. 2019). Since the large phase amplitude (0.601) presented in Mansfield

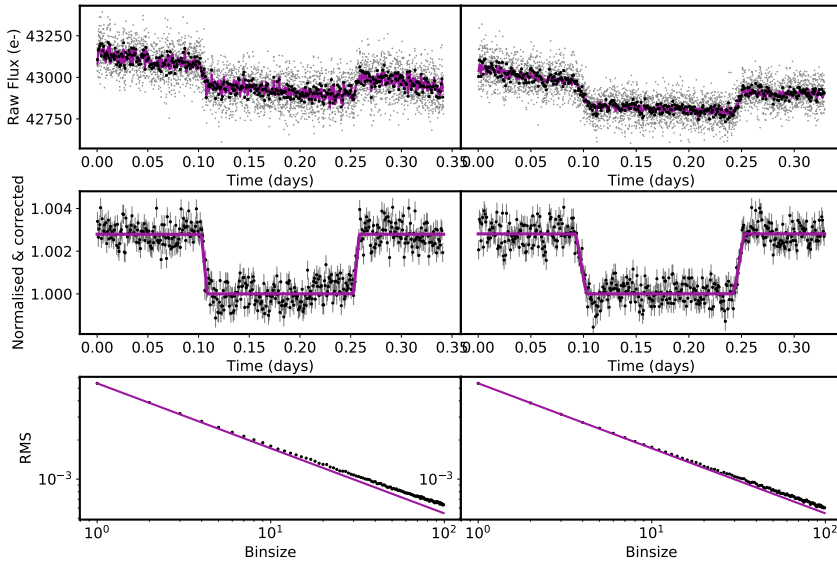


Fig. 3.9: Eclipses of KELT-9b for AORs r67667712 (left panel) and r67667968 (right panel). The top row shows the raw photometric lightcurve with our best fit PLD model. The middle row shows the corrected lightcurves with the best fit eclipse model. The bottom row shows the RMS vs binsize of the data; since this closely follows the photon noise line (\sqrt{N}) we can see that we are capturing the systematics well.

et al. (2020) clearly demonstrates a concave phase variation around the ellipse, this is likely the cause of the discrepancy between the two sets of data analyses. However, since we do not see any trend with the phase curve offsets between the two Spitzer bandpasses (discussed in Section 3.5.4.1) we expect that any underestimation of the eclipse depth will apply to both $3.6\ \mu\text{m}$ and $4.5\ \mu\text{m}$, and thus the deviation from the blackbody will be largely unaffected. Nevertheless, such an effect could be relevant for higher precision measurements with the James Webb Space Telescope.

Since we only have the available $4.5\ \mu\text{m}$ measurement of KELT-9b, this data point is excluded from any of the fits in our analysis. Nevertheless, we can see that the brightness temperature deviates positively from equilibrium at $4.5\ \mu\text{m}$. However, like several of the hottest planets, the deviation is smaller than expected compared to the model predictions in Figure 3.3. We interpret this as indicative of more complex physical processes happening in the atmosphere of this extreme object (Bell & Cowan 2018; Komacek 2018; Lothringer et al. 2018; Kitzmann et al. 2018; Mansfield et al. 2020). For example, due to the high temperature on the dayside of KELT-9b, there could be less carbon monoxide available in the atmosphere due to it being dissociated (Kitzmann et al. 2018).

Table 3.2: Planetary eclipse depths from the literature, calculated equilibrium temperatures, calculated brightness temperatures, and deviations from blackbody using PHOENIX models and stellar parameters used to obtain the correct stellar models.

Planet	$(F_p/F_s)_{3.6}$	$(F_p/F_s)_{4.5}$	$T_{eq_{\ell=0}}$	T_{eff}	logg	[Fe/H]	$T_{B_{3.6}}$	$T_{B_{4.5}}$	devBB	Ref.
	(ppm)	(ppm)	(K)	(K)	(cgs)	(dex)	(K)	(K)	(%)	
HAT-P-32b	3640±160	4380±200	1785±32	6207±88	4.33±0.01	-0.04±0.08	2073±40	2023±46	0.006±0.026	1
XO1b	860±70	1220±90	1207±30	5750±75	4.5±0.01	0.02±0.08	1301±32	1257±34	-0.001±0.012	2
HAT-P-1b	800±80	1350±220	1306±33	5980±49	4.36±0.01	0.13±0.01	1437±47	1521±103	0.026±0.024	3
WASP-39b	880±150	960±180	1118±35	5400±150	4.4±0.2	-0.12±0.1	1220±60	1066±63	-0.034±0.026	4
HAT-P-18b	437±145	326±146	847±26	4803±80	4.57±0.04	0.1±0.08	1011±83	787±88	-0.04±0.025	5
TrES2b	1270±210	2300±240	1498±32	5850±50	4.43±0.02	-0.15±0.1	1543±90	1712±81	0.063±0.034	6
WASP-4b	3190±310	3430±270	1651±27	5436±34	4.46±0.05	-0.05±0.04	1825±72	1650±57	-0.049±0.042	7
XO2b	810±170	980±200	1322±23	5340±32	4.48±0.05	0.45±0.02	1460±104	1346±104	-0.011±0.028	8
WASP-1b	1170±160	2120±210	1876±69	6200±200	4.3±0.3	0.1±0.2	1781±95	2067±103	0.066±0.027	9
HAT-P-26b	85±0	265±70	994±48	5079±88	4.56±0.06	-0.04±0.08	935±0	1067±90	0.011±0.007	5
CoRoT-1 b	4150±420	4820±420	1900±81	5950±150	4.25±0.3	-0.3±0.25	2298±109	2236±102	0.006±0.06	10
CoRoT-2 b	3550±200	5000±200	1537±40	5625±120	4.53±0.02	0.03±0.06	1811±40	1854±36	0.062±0.029	10
HAT-P-17 b	118±39	149±...	779±17	5246±80	4.53±0.02	0.0±0.08	807±54	704±...	-0.009±...	5
HAT-P-19 b	620±140	620±140	1009±40	4990±130	4.54±0.05	0.23±0.08	1095±66	924±59	-0.036±0.023	4
HAT-P-2 b	996±72	1031±61	1428±57	6290±60	4.16±0.08	0.14±0.08	2256±76	2065±62	-0.012±0.01	11
HAT-P-20 b	615±82	1096±77	971±24	4595±80	4.63±0.02	0.35±0.08	1127±40	1131±26	0.014±0.013	12
HAT-P-23 b	2480±190	3090±260	2051±71	5905±80	4.33±0.05	0.15±0.04	2137±73	2128±92	0.018±0.032	13
HAT-P-3 b	1120±225	940±125	1158±34	5185±80	4.56±0.03	0.27±0.08	1550±110	1252±60	-0.053±0.028	14
HAT-P-4 b	1420±160	1220±130	1694±47	5860±80	4.36±0.11	0.24±0.08	2291±120	1906±98	-0.041±0.021	14
HAT-P-6 b	1170±80	1060±60	1673±42	6570±80	4.22±0.03	-0.13±0.08	1973±57	1681±43	-0.035±0.01	15
HAT-P-7 b	1560±130	1900±110	2225±41	6389±17	47±0.06	0.26±0.08	2657±113	2704±92	0.016±0.017	16
HAT-P-8 b	1310±85	1110±75	1772±48	6200±80	4.15±0.03	0.01±0.08	2050±58	1695±52	-0.045±0.012	15
HD 149026 b	400±30	340±60	1673±65	6160±50	4.28±0.05	0.36±0.08	1945±61	1603±122	-0.014±0.007	17

Table 3.2: continued.

Planet	$(F_p/F_s)_{3.6}$	$(F_p/F_s)_{4.5}$	$T_{eq,i=0}$	T_{eff}	logg (cgs)	[Fe/H] (dex)	$T_{B_{3.6}}$ (K)	$T_{B_{4.5}}$ (K)	devBB (%)	Ref.
HD 189733 b	2560±140	2140±200	1200±22	5040±50	4.59±0.01	-0.03±0.08	1604±32	1298±45	-0.115±0.025	18
HD 209458 b	1190±70	1230±60	1446±19	6065±50	4.36±0.01	0.0±0.05	1577±33	1392±27	-0.033±0.01	19
Kepler-12 b	1370±200	1160±310	1481±31	5947±100	4.18±0.01	0.07±0.04	1672±91	1369±142	-0.058±0.038	20
Kepler-17 b	2500±300	3100±350	1745±39	5781±85	4.53±0.12	0.26±0.1	1952±98	1902±102	0.008±0.047	21
Kepler-5 b	1030±170	1070±150	1807±35	6297±60	3.96±0.1	0.04±0.06	2045±146	1859±124	-0.016±0.023	22
Kepler-6 b	690±270	1510±190	1504±21	5647±44	4.24±0.01	0.34±0.04	1462±196	1726±98	0.058±0.036	23
KOI-13 b	1560±310	2220±230	2607±94	7650±250	4.2±0.5	0.2±0.2	2456±238	2716±164	0.044±0.039	24
Qatar-1 b	1490±510	2730±490	1389±43	4861±125	4.54±0.02	0.2±0.1	1374±153	1470±108	0.068±0.077	25
TrES-3 b	3460±350	3720±540	1629±32	5650±75	4.58±0.01	-0.19±0.08	1797±72	1624±103	-0.056±0.066	26
TrES-4 b	1370±110	1480±160	1785±41	6200±75	4.06±0.02	0.14±0.09	1947±65	1793±90	-0.017±0.02	27
WASP-10 b	1000±110	1460±160	960±24	4675±100	4.4±0.2	0.03±0.2	1151±35	1091±39	-0.007±0.021	11
WASP-103 b	4458±383	5686±138	2505±78	6110±160	4.22±0.08	0.06±0.13	3114±149	3337±52	0.088±0.04	28
WASP-12 b	4210±110	4280±120	2584±91	6300±150	4.38±0.1	0.3±0.1	2872±40	2649±43	-0.034±0.016	29
WASP-121 b	3150±103	4510±107	2359±61	6459±140	4.24±0.01	0.13±0.09	2358±36	2591±35	0.09±0.015	25
WASP-14 b	1870±70	2240±180	1864±60	6475±100	4.07±0.2	0.0±0.2	2248±39	2221±93	0.007±0.019	30
WASP-18 b	3000±200	3900±200	2398±73	6400±100	4.37±0.04	0.0±0.09	2990±109	3231±104	0.063±0.028	31
WASP-19 b	4830±250	5720±300	2066±46	5500±100	4.5±0.2	0.02±0.09	2326±57	2270±63	0.02±0.039	32
WASP-2 b	830±350	1690±170	1300±71	5200±200	4.54±0.04	0.1±0.2	1241±158	1350±51	0.048±0.046	9
WASP-24 b	1590±130	2020±180	1769±39	6075±100	4.26±0.17	0.0±0.1	2044±73	2044±92	0.013±0.022	33
WASP-33 b	2600±500	4100±200	2694±53	7430±100	4.3±0.2	0.1±0.2	2674±264	3202±98	0.119±0.054	34
WASP-43 b	3460±130	3820±150	1375±79	4400±200	4.65±0.05	-0.05±0.17	1664±24	1497±24	-0.053±0.02	35
WASP-48 b	1760±130	2140±200	2033±68	5920±150	4.03±0.03	-0.12±0.12	2147±70	2113±101	0.008±0.024	13
WASP-5 b	1970±280	2370±240	1742±68	5880±150	4.4±0.04	0.09±0.09	2030±125	1969±98	0.002±0.038	36
WASP-6 b	940±190	1150±220	1184±32	5450±100	4.6±0.2	-0.2±0.09	1247±75	1134±72	-0.022±0.032	4

Table 3.2: continued.

Planet	$(F_p/F_s)_{3.6}$	$(F_p/F_s)_{4.5}$	$T_{eq_{\text{eff}0}}$	T_{eff}	logg	[Fe/H]	$T_{B_{3.6}}$	$T_{B_{4.5}}$	devBB	Ref.
	(ppm)	(ppm)	(K)	(K)	(cgs)	(dex)	(K)	(K)	(%)	
WASP-67 b	220±130	800±180	1028±32	5200±100	4.35±0.15	-0.07±0.09	887±122	1042±73	0.039±0.027	4
WASP-69 b	421±29	463±39	961±21	4700±50	4.5±0.15	0.15±0.08	1006±17	864±19	-0.024±0.006	5
WASP-8 b	1130±180	690±70	927±27	5600±80	4.5±0.1	0.17±0.07	1573±90	1144±39	-0.078±0.021	37
WASP-80 b	455±100	944±65	775±25	4150±100	4.6±0.2	-0.14±0.16	878±42	875±16	0.01±0.016	38
XO-3 b	1010±40	1580±36	2046±40	6429±50	3.95±0.06	-0.18±0.03	1814±29	1972±21	0.033±0.006	39
XO-4 b	560±90	1350±85	1639±35	6397±70	4.18±0.07	-0.04±0.03	1535±86	1957±60	0.061±0.013	15
HAT-P-13 b	851±107	1090±124	1648±53	5653±90	4.13±0.04	0.41±0.08	1775±87	1728±89	0.003±0.017	25
HAT-P-30 b	1584±107	1825±147	1637±43	6304±88	4.36±0.3	0.13±0.08	1868±51	1763±65	-0.012±0.019	25
HAT-P-33 b	1603±127	1835±199	1780±34	6446±88	4.15±0.01	0.05±0.08	2000±67	1901±98	-0.009±0.024	25
HAT-P-40 b	988±168	1057±145	1765±66	6080±100	3.93±0.02	0.22±...	2005±146	1840±119	-0.012±0.023	25
HAT-P-41 b	1829±319	2278±177	1937±44	6390±100	4.14±0.02	0.21±0.1	2173±172	2179±88	0.014±0.037	25
KELT-2 A b	650±38	678±47	1710±31	6151±50	4.03±0.02	-0.02±0.07	1862±44	1679±52	-0.012±0.006	25
KELT-3 b	1766±97	1656±104	1822±44	6304±49	4.2±0.03	0.05±0.08	2300±59	2006±62	-0.038±0.014	25
WASP-100 b	1267±98	1720±119	2200±171	6900±120	4.35±0.17	-0.03±0.1	2216±79	2337±88	0.024±0.016	25
WASP-101 b	1161±111	1194±113	1554±40	6380±120	4.31±0.08	0.2±0.12	1680±61	1492±58	-0.029±0.017	25
WASP-104 b	1709±195	2643±303	1516±43	5475±127	4.5±0.02	0.32±0.09	1734±76	1828±98	0.05±0.037	25
WASP-131 b	364±97	282±78	1439±36	5950±100	3.9±0.1	-0.18±0.08	1361±115	1077±96	-0.023±0.014	25
WASP-36 b	913±578	1948±544	1699±45	5881±136	4.5±0.01	-0.31±0.12	1300±267	1475±168	0.064±0.089	25
WASP-46 b	1360±701	4446±589	1658±55	5620±160	4.49±0.02	-0.37±0.13	1394±241	1968±129	0.258±0.101	25
WASP-62 b	1616±146	1359±130	1427±35	6230±80	4.45±0.1	0.04±0.06	1906±71	1568±63	-0.061±0.02	25
WASP-63 b	552±95	533±128	1531±45	5550±100	4.01±0.03	0.08±0.07	1573±97	1347±123	-0.018±0.017	25
WASP-64 b	2859±270	2071±471	1690±52	5550±150	4.39±0.02	-0.08±0.11	2102±87	1610±159	-0.129±0.055	25
WASP-65 b	1587±245	724±318	1485±59	5600±100	4.25±0.1	-0.07±0.07	1781±108	1160±177	-0.125±0.041	25
WASP-74 b	1446±66	2075±100	1923±53	5990±110	4.39±0.07	0.39±0.13	1997±39	2106±51	0.034±0.012	25

Table 3.2: continued.

Planet	$(F_p/F_s)_{3.6}$	$(F_p/F_s)_{4.5}$	$T_{eq,a=0}$	T_{eff}	logg	[Fe/H]	$T_{B_{3.6}}$	$T_{B_{4.5}}$	devBB	Ref.
	(ppm)	(ppm)	(K)	(K)	(cgs)	(dex)	(K)	(K)	(%)	
WASP-76 b	2645±63	3345±82	2183±47	6250±100	4.4±0.1	0.23±0.1	2411±28	2471±33	0.034±0.01	25
WASP-77 A b	1845±94	2362±127	1671±31	5500±80	4.33±0.08	0.0±0.11	1685±32	1628±37	0.002±0.016	25
WASP-78 b	2001±218	2013±351	2295±88	6100±150	4.1±0.2	-0.35±0.14	2787±160	2565±255	-0.019±0.041	25
WASP-79 b	1394±88	1783±106	1762±53	6600±100	4.2±0.15	0.03±0.1	1893±49	1882±54	0.008±0.014	25
WASP-87 b	2077±127	2705±137	2311±68	6450±120	4.32±0.21	-0.41±0.1	2687±85	2863±87	0.04±0.019	25
WASP-94 A b	867±59	995±93	1504±77	6170±80	4.27±0.07	0.26±0.15	1527±36	1398±50	-0.016±0.011	25
WASP-97 b	1359±84	1534±101	1540±42	5640±100	4.45±0.08	0.23±0.11	1727±40	1590±44	-0.017±0.014	25
KeLT-9 b	...±...	2802±33	4051±199	10170±450	4.09±0.01	-0.03±0.2	...±...	...±...	...±...	40

(1) Zhao et al. (2014); (2) Machalek et al. (2008); (3) Todorov et al. (2010); (4) Kammer et al. (2015); (5) ?; (6) O'Donovan et al. (2010); (7) Beeler et al. (2011); (8) Machalek et al. (2009); (9) Wheatley et al. (2010); (10) Deming et al. (2011); (11) Lewis et al. (2013); (12) Deming et al. (2015); (13) O'Rourke et al. (2014); (14) Todorov et al. (2013); (15) Todorov et al. (2012); (16) Christiansen et al. (2010); (17) Stevenson et al. (2012); (18) Charbonneau et al. (2008); (19) Diamond-Lowe et al. (2014); (20) Fortney et al. (2011); (21) Désert et al. (2011c); (22) Désert et al. (2011a); (23) Désert et al. (2011d); (24) Shporer et al. (2014); (25) Garhart et al. (2020); (26) Fressin et al. (2010); (27) Knutson et al. (2009); (28) Kreidberg et al. (2018a); (29) Stevenson et al. (2018a); (30) Blecic et al. (2013); (31) Nyrmeyer et al. (2011); (32) Anderson et al. (2013); (33) Smith et al. (2012); (34) Deming et al. (2012); (35) Blecic et al. (2014); (36) Baskin et al. (2013); (37) Cubillos et al. (2013); (38) Triaud et al. (2015); (39) Machalek et al. (2010); (40) This work;

PERIODIC VARIABILITY IN THE BRIGHTNESS OF AN ULTRA-HOT JUPITER ATMOSPHERE



Claire Baxter & Jean-Michel Désert

Astronomy & Astrophysics, (to be submitted)

Abstract

Context With close-in orbits and strong stellar irradiation on tidally locked daysides, hot Jupiter atmospheres are predicted to form large-scale weather structures. Observing the variability of a hot Jupiter is a key probe of such weather patterns as well as probing the atmospheric dynamics and temperature structures.

Aims We aim to characterize the brightness variability of the ultra-hot Jupiter WASP-18b by analyzing ten secondary eclipses at $4.5\text{ }\mu\text{m}$ with Spitzer/IRAC.

Methods Our observations span a time frame of 21.6 days which covers 23 planetary orbits. We search for temporal variability by robustly analyzing each of the lightcurves using our custom pipeline which implements pixel level decorrelation. We benchmark our results against the well-studied XO-3b.

Results We observe a variability in the eclipse depth with time, which is the first infrared temporal variability in secondary eclipse observations of hot Jupiters. Using a sinusoidal model, we derive a variability period of 23.12 ± 1.66 days and a peak-to-trough amplitude of 456 ± 71 ppm, corresponding to $\sim 12\%$ variability. We discuss possible causes of this variability, such as stellar variability, variable wind speeds, clouds, changes in atmospheric composition, and magnetic field coupling. We find that a 12% variability signal would not be detected in the four available sectors of TESS containing WASP-18b, or with the 5 available HST/WFC3 eclipses, and that future observatories would be required for followup.

4.1 Introduction

Hot Jupiters are ideal targets for precise atmospheric characterization due to their large planet-to-star flux ratios. There have now been many secondary eclipse observations of hot Jupiters in the infrared, ranging from individual studies (e.g., Charbonneau et al. 2005; Deming et al. 2005) to large-scale survey programs (e.g., Schwartz et al. 2017; Baxter et al. 2020; Garhart et al. 2020). The vast majority of hot Jupiter atmospheres are expected to form clouds and photochemical hazes (Sing et al. 2016; Parmentier et al. 2016; Wakeford et al. 2019). Inhomogeneous coverage of such clouds could lead to brightness variability in time.

Temporal variations have been observed at $5\text{ }\mu\text{m}$ in the equatorial banded structures of Jupiter (Antuñano et al. 2019). Variability in time is also common in cool brown dwarfs, with variability amplitudes of a few percent in more than 50% of L and T brown dwarfs (Metchev et al. 2015). Furthermore, variability has also recently been detected on directly imaged free-floating planetary-mass objects (e.g., Biller et al. 2015). However, observing variability on directly imaged exoplanets is difficult due to the contrast between the host star and planet (Apai et al. 2016).

Nevertheless, atmospheric variability in time has been measured with phase curve observations of 3 hot Jupiters to date: HAT-P-7b (Armstrong et al. 2016), Kepler-76b (Jackson et al. 2019), and WASP-12b (Bell et al. 2019). Armstrong et al. (2016) use 4 years of public *Kepler* data of HAT-P-7b to search for variability. They find temporal variations in the phase curve shape, including the hot-spot offset, such that the hot-spot shifts from one side of the substellar point to the other on timescales of tens to hundreds of days. However, they find only marginal evidence of brightness variability in time, which they note can be explained by systematic noise in their fits. Also using *Kepler* data, Jackson et al. (2019) found similar phase offset variability in Kepler-76b, however, they do measure variability in the phase curve amplitude. Furthermore, two phase-curve observations at $3.6\text{ }\mu\text{m}$ taken 3 years apart of WASP-12b measure the phase curve offset to be $32.6 \pm 6.2^\circ$ eastward to $13.6 \pm 3.8^\circ$ westward (Bell et al. 2019).

To date, there has been no periodic brightness variability measured in secondary eclipse observations of hot Jupiters in the infrared. Agol et al. (2010) place an upper limit of 2.7% at $8\text{ }\mu\text{m}$ on the eclipse depth variability of HD 189733b. Furthermore, Kilpatrick et al. (2020) carried out multi-epoch secondary eclipse observations with Spitzer/IRAC in an attempt to constrain the variability of HD 189733b and HD 209458b. They do not find a periodic variability signal, but they can place upper limit constraints on any possible variability to 12% and 1.6% at $4.5\text{ }\mu\text{m}$ for HD 189733b and HD 209458b respectively.

A possible cause of the variability on HAT-P-7b in the optical is variable wind speeds leading to variable cloud coverage (Armstrong et al. 2016). Similarly, Jackson et al. (2019) proposed the advance and retreat of thermal structures on Kepler-76b. This leads to cloud formation on the nightside blowing over to the dayside and creating a feedback loop resulting in periodic variability. Rogers (2017) explored the effect of magnetic fields on HAT-P-7b by incorporating magnetohydrodynamics (MHD) into their global circulation models (GCMs).

They conclude that coupling of the magnetic field with ionized species in the atmosphere can act against the eastward hot spot offset caused by the day-night temperature contrast. Such feedback can settle into an oscillating pattern on timescales of $\sim 10^6$ seconds, creating the observed variability. In the case of WASP-12b, analysis of the 3.6 and 4.5 μm phase curves suggest mass-loss of the planet (Bell et al. 2019). Variability in the mass loss rate could be the cause of the phase offset variability. However, they also note that, following the arguments of Rogers (2017), variability due to magnetic coupling would be expected on WASP-12b.

In this paper, we measure and discuss the atmospheric brightness variability in the infrared of the ultra-hot Jupiter WASP-18b.

4.2 Observations

We observed ten secondary eclipses of WASP-18b at 4.5 μm with Spitzer/Infrared array camera (IRAC), program 11099 (PI: Kreidberg). Each observation consisted of 11776 exposures of 2-second integration in sub-array mode, resulting in 6.54 hours per lightcurves. Our observations were preceded with a scheduled 30-minute throw-away "peak-up" observation to obtain accurate pointing before the main observation to minimize the effect of IRACs well known intrapixel sensitivity. The ten eclipses span from 8th-30th September 2015, a total time of 21.65 days, corresponding to 23 orbits of WASP-18b, given its orbital period of 0.94124000 days (Pearson 2019).

Furthermore, we also analyzed the ten eclipses of XO-3b, program 90032 (PI: Knutson), to test the robustness of our pipeline and our results, particularly on the variability. These eclipses were previously part of the repeatability and reliability data challenge presented in Ingalls et al. (2016).

4.3 Data Analysis

4.3.1 Spitzer/IRAC photometric lightcurve reduction

We reduce the Spitzer/IRAC secondary eclipse lightcurves with our custom pipeline described fully in Baxter et al. (submitted.) which follows the analysis method from (Deming et al. 2015). For clarity, we recall the main steps of our pipeline. In each of the Spitzer subarray frames, we correct the dark current, flat field, and convert to flux units before performing aperture photometry using a circular aperture around the calculated centroid position of the star. A full run of our pipeline creates a grid of data reductions and finds the optimum methods and parameters for background subtraction, centroiding, and aperture photometry radius utilizing a lowest reduced χ^2 on the resulting lightcurves. Uncertainties on the photometric points are calculated from photon noise and scaled up such that the reduced χ^2 after an initial least-squares fit is equal to 1.

Our resulting optimum pipeline reduction methods were to centroid using the barycenter

method, with a box size of 3x3, calculate the background using 4 pixels in each of the 4 corners of the image, and to perform aperture photometry with a radius of 2.5 pixels around the star. In each lightcurve, we masked between 0.053% and 0.076% bad pixels at 4σ . We also removed 15 minutes from the beginning of each of the lightcurves to remove the peak-up period of the observations. The best raw normalized photometric lightcurve for each observation is then used in the next step for a complete statistical analysis of the transit/eclipse parameters.

4.3.2 Spitzer/IRAC secondary eclipse fitting

To find the eclipse parameters from the raw photometric lightcurve, we fit a batman eclipse model (Kreidberg 2015) in combination with a temporal quadratic function (1 or 2 order) and a pixel level decorrelation (PLD) systematic model (Deming et al. 2015). In our fit of WASP-18 b, we fix the period to 0.9414529 ± 0.00000234 (Pearson 2019) and the eccentricity and angle of periastron passage to 0.

Typically, the PLD systematic model uses a 3x3 grid of pixels around the centroid of the star to model the systematics. Since WASP-18b is a bright star, a significant portion of the stellar PSF may spread beyond these nine pixels, we, therefore, test the effect of including more pixels with a 5x5 PLD grid. However, we found that a 5x5 PLD box compared to a 3x3 PLD box was not improving the fits.

Furthermore, since assuming a 1 order quadratic (linear) baseline can result in underestimating the eclipse depth for hot planets with large phase amplitudes (e.g., Bell et al. 2019), we also tested a 2 order quadratic baseline in time. However, such a 2 order quadratic coefficient can also be degenerate with the eclipse depth. We tested including a 2 order quadratic baseline (2 free parameters) compared to a 1 order baseline (1 free parameter). We found that it was not statistically significant to have a 2 order quadratic free in each of the fits (mean ΔBIC of 3). However, we also tested fixing the 2 order quadratic co-efficient while still leaving the 1 order co-efficient free. This test was statistically significant (mean ΔBIC of 53) when comparing it with a 1 order quadratic (linear) baseline. We, therefore, opted to fix the 2 order coefficient to the weighted mean value from the first fit, -0.031 ± 0.004 . This method corrects the astrophysical signal from the large phase amplitudes (2 order) without compromising the systematic correction (1 order) and thus leads to accurate results on the eclipse depths.

To achieve our final results we perform two fits of the lightcurves. First, we perform an initial fit with 15 free parameters (a/R_s , inclination, F_p/F_s , $T_{\text{secondary}}$, 9 PLD parameters and a 2 order quadratic baseline in time). Then we fix a/R_s , inclination and the 2 order quadratic coefficient to the weighted mean over all ten lightcurves. We do this since we do not expect these parameters to be physically changing in time. Our final MCMC fits have 12 free parameters (R_p/R_s , $T_{\text{secondary}}$, 9 PLD parameters and 1 temporal slope). As a sanity check, we compare the brightness temperatures between the first and second fit in Figure 4.4, and find that it still shows variability.

Posterior distributions and uncertainties are calculated on the fitted parameters by performing a full Markov Chain Monte Carlo (MCMC) exploration of parameter space using emcee (Foreman-Mackey et al. 2013). We run chains with 100 walkers with a typical 500 step burn-in period followed by a 1000 step production run and confirm the convergence of our chains via the auto-correlation time and the mean acceptance fraction.

4.4 Results

4.4.1 Spitzer/IRAC secondary eclipse lightcurves

Table 4.1 displays the a/R_s , inclination and 2 order quadratic coefficient from the first fit alongside F_p/F_s , $T_{\text{secondary}}$ and T_B from the second fit. Figure 4.1 shows the final resulting systematic corrected lightcurves. We find that the weighted mean eclipse depth is 3729 ± 56 ppm, which is consistent with the eclipse presented in Nymeyer et al. (2011) and the phase curve presented in Maxted et al. (2013). We also find that the weighted mean secondary eclipse timings are within 1σ agreement with the previously calculated eclipse ephemeris from Maxted et al. (2013). Raw lightcurves and residuals are shown in Appendix 4.A.

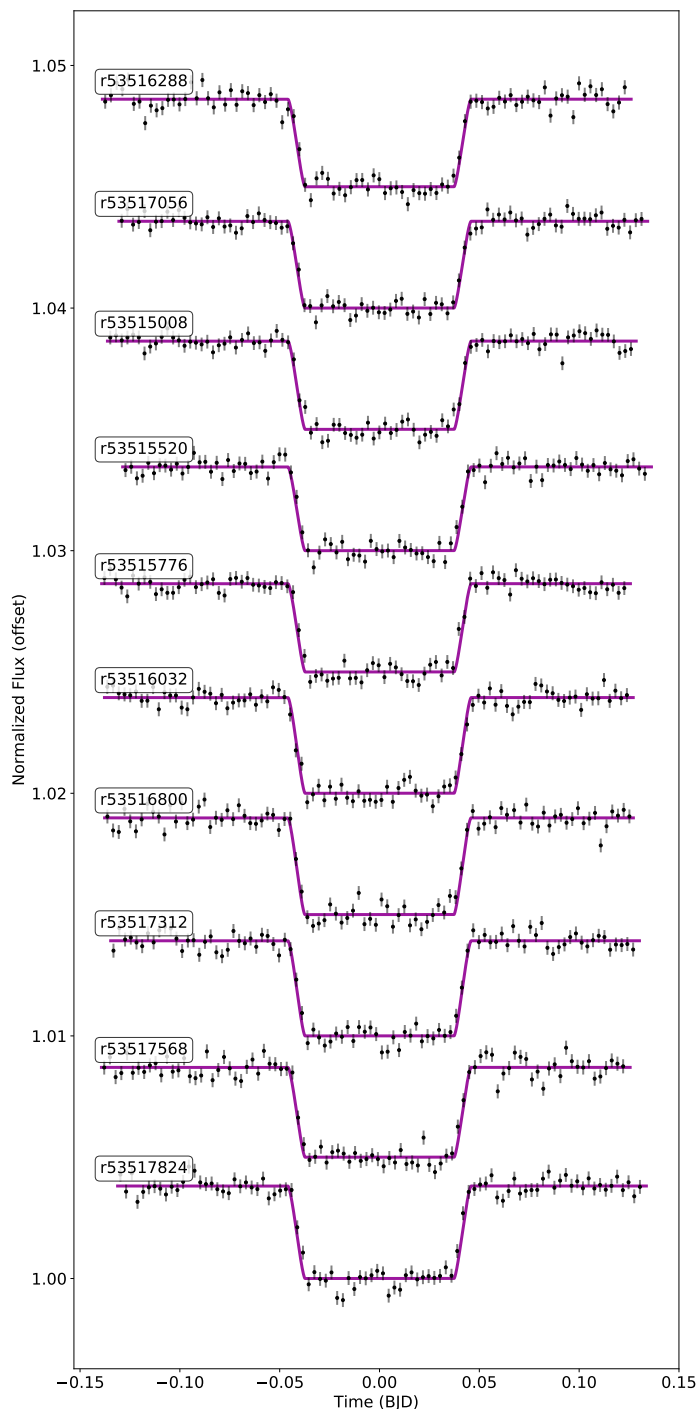


Fig. 4.1: Normalized and corrected eclipse lightcurves of WASP-18b, vertically offset for display purposes. These lightcurves are from the final fit, where we fixed a/R_s , inclination and the 2 quadratic coefficient to their weighted means from the first fit.

Table 4.1: Best fit eclipse and systematic parameters using an MCMC method. The semi-major axis (a/R_s), inclination and 2nd order quadratic co-efficient (h) are shown from the first fits, they are fixed to the weighted mean in the final fit. The eclipse depth (F_p/F_s), brightness temperature (T_B) and the time of secondary eclipse ($T_{secondary}$) are shown from the final fits.

AOR	a/R_s	Inclination Degrees	h	F_p/F_s ppm	T_B Kelvin	$T_{secondary}$ BJD
r53517824	3.48 ± 0.15	83.29 ± 2.05	-0.03 ± 0.008	3810 ± 68	3079 ± 37	2457274.14104 ± 0.00029
r53517568	3.46 ± 0.14	83.38 ± 1.95	-0.039 ± 0.008	3700 ± 68	3011 ± 37	2457275.08202 ± 0.0003
r53517312	3.43 ± 0.16	83.09 ± 2.22	-0.035 ± 0.01	3919 ± 78	3166 ± 41	2457278.84855 ± 0.00028
r53516800	3.34 ± 0.15	82.04 ± 1.94	-0.038 ± 0.008	3984 ± 66	3163 ± 36	2457279.78877 ± 0.00026
r53516032	3.15 ± 0.15	80.42 ± 1.75	-0.011 ± 0.009	3954 ± 69	3147 ± 37	2457283.55482 ± 0.00028
r53515776	3.48 ± 0.14	83.27 ± 1.85	-0.041 ± 0.008	3640 ± 68	2984 ± 38	2457286.37946 ± 0.00028
r53515520	3.28 ± 0.18	81.15 ± 2.26	-0.046 ± 0.009	3454 ± 70	2890 ± 37	2457288.26257 ± 0.00029
r53515008	3.06 ± 0.18	78.70 ± 2.09	-0.028 ± 0.009	3633 ± 67	2988 ± 35	2457289.2035 ± 0.00029
r53517056	3.32 ± 0.19	82.08 ± 2.41	-0.025 ± 0.008	3585 ± 71	2943 ± 37	2457293.91153 ± 0.00031
r53516288	3.38 ± 0.18	82.32 ± 2.27	-0.013 ± 0.009	3616 ± 69	2973 ± 38	2457295.79433 ± 0.0003
Weighted Mean	3.45 ± 0.04	81.96 ± 0.49	-0.031 ± 0.004	3729 ± 56	3033 ± 31	
Standard Deviation	0.13	1.43	0.01	169	93	
Mean Error	0.16	2.08	0.01	69	37	

4.4.2 Brightness variability of WASP-18b in time

We plot the secondary eclipse depths of WASP-18b in time (see Figure 4.2), and we find that the eclipse depths are not constant, but instead they show a level of variability, that isn't random, but that is reproduced by a periodic sinusoidal signal. We find that the eclipse depth measurements deviate from a straight line by more than 7σ . We fit this temporal brightness variability with a sinusoidal function in time (t). We parameterize the sinusoid with four free parameters: semi-amplitude (A), frequency (ν), phase (φ) and an offset (\bar{D}) such that the eclipse depths in time are modeled with $D(t) = A\sin(\nu t) + \bar{D}$. We tested fixing the phase parameter (φ) but this did not significantly improve the fits ($\Delta\text{BIC} = 2.2$). We calculate posterior distributions on these parameters by running an MCMC exploration using emcee (Foreman-Mackey et al. 2013) with 300 walkers, 1000 burn-in steps and 20000 production steps. We confirm convergence of the chains using the auto-correlation time and the mean acceptance fraction. We then test the robustness of our sinusoidal fit by comparing it with a straight line using the Bayesian Information Criteria (BIC).

Figure 4.3 shows the posterior distributions from the MCMC sinusoidal fits and the best sinusoidal fit is also shown in Figure 4.2. We find that the sinusoidal fit is statistically significantly favored over a straight line fit where BIC of the straight line being 62.3 and the BIC of the sinusoid being 18.2. The best fit sinusoidal parameters are: $A = 228 \pm 36$ ppm, $\nu = 0.27 \pm 0.02$, $\varphi = -0.01 \pm 0.23$, $\bar{D} = 3732 \pm 23$ ppm. This corresponds to a 23.1 ± 1.7 days period of variability and a $12.2 \pm 1.9\%$ peak-to-trough brightness variability ($2A$).

We tested for variability and correlations with the other parameters we let free in the fits. The standard deviation is smaller than the mean error over all ten lightcurves for a/R_s and inclination (see Table 4.1). This indicates that there is no variability in these parameters. We also tested for correlations between a/R_s and inclination with F_p/F_s , in both cases they had low Pearson correlation coefficients (0.05 and 0.13 respectively) with high associated chance probabilities (0.9 and 0.7 respectively). These numbers indicate that a/R_s and inclination are not correlated with F_p/F_s .

4.4.3 Testing the method to measure variability

To test the robustness of our analysis and ensure that our method does not introduce any spurious variability, we analyze the ten secondary eclipses of another hot Jupiter, XO-3b, which has been widely studied, and which serves as a calibration of our methods. These eclipses were first published in Wong et al. (2014) and later used as part of the extensive repeatability and accuracy post-cryogenic Spitzer/IRAC data challenge (Ingalls et al. 2016). Ingalls et al. (2016) test seven different techniques for correcting the correlated noise. Across these seven techniques they measure an average eclipse depth of 1520 ± 30 ppm. This value is a straight average of the weighted mean and weighted uncertainty over the ten eclipses for each technique. We calculate the weighted mean and weighted uncertainty using the same method (see their eq. 5-9) and find that the weighted mean eclipse depth of our PLD corrected

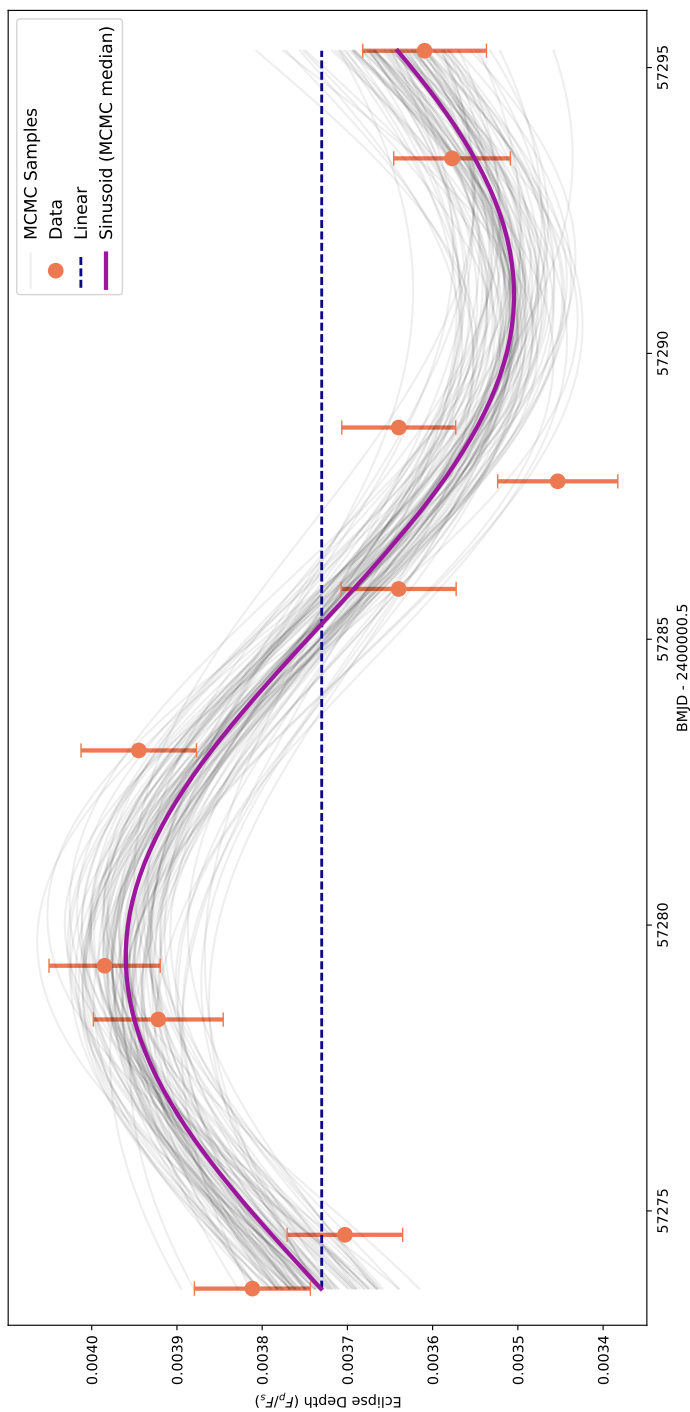


Fig. 4.2: Measured eclipse depths of WASP-18b over time in orange, for the ten semi-consecutive eclipses. Purple solid line shows the median result from the MCMC fit, 100 random samples from the posterior distributions are shown in gray, blue line shows the best fitting straight line.

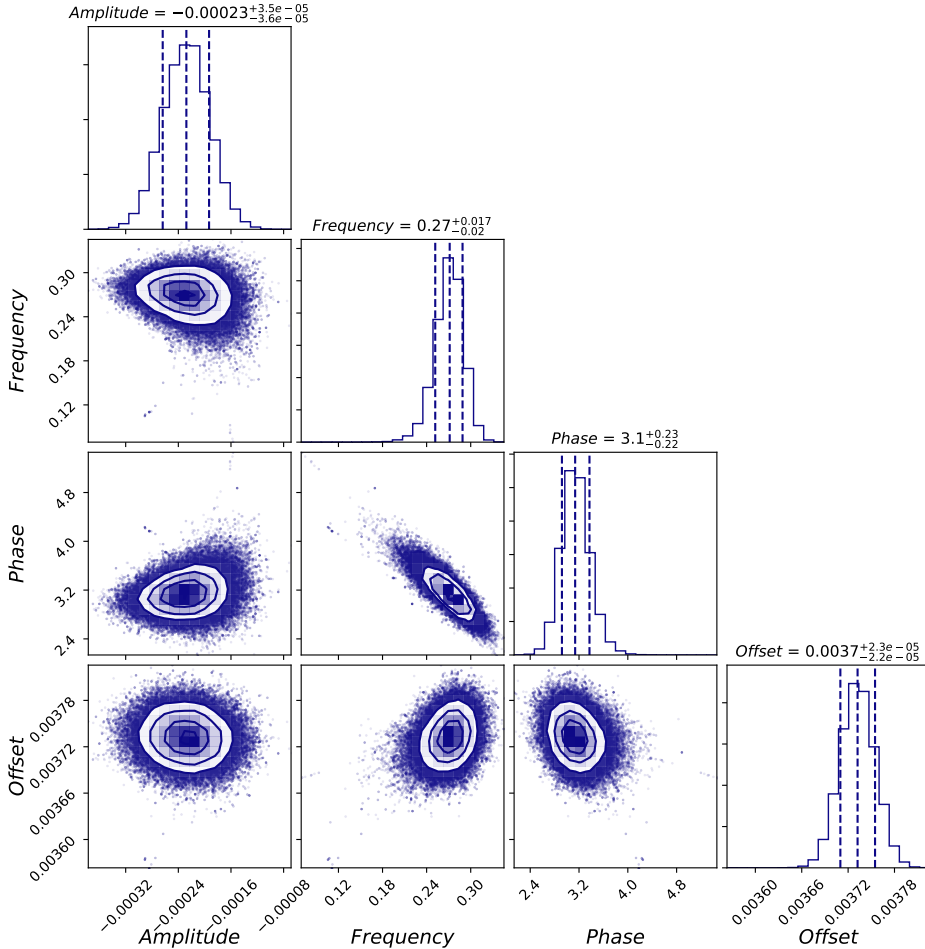


Fig. 4.3: Posterior probability distributions of the free parameters from a periodic sinusoidal MCMC fit to the brightness variability in time of WASP-18b at 4.5 μm . In the marginalized confidence intervals the inner dashed line is the median and the outer dashed lines are the 1σ confidence level.

secondary eclipses to be 1520 ± 29 ppm. This is in remarkable agreement with Ingalls et al. (2016) and we conclude that our pipeline produces consistent results.

For XO-3b we measure the mean uncertainty over the ten eclipses to be 84 ppm, which is in agreement with the average precision achieved over the seven different techniques in Ingalls et al. (2016), which was 102 ppm (ranging from 48 ppm to 152 ppm). We also find that the standard deviation of the ten eclipse depths to be 86 ppm. The fact that the mean uncertainty and the standard deviation are the same indicates that the eclipse depths are drawn from a random distribution, and there is no evidence for variability in the eclipses of XO-3b.

On the other hand, for WASP-18b, the mean uncertainty of the ten eclipse depths is 69 ppm, yet the standard deviation is 173 ppm. This indicates that there is variability measured at a significant level in the secondary eclipse measurements of WASP-18b.

4.4.4 Variability of WASP-18b at various wavelengths

WASP-18b was also observed at 3.6 μm with Spitzer/IRAC on two occasions: an eclipse was observed in December 2008, $F_p/F_s=3040\pm170$ ppm (Nymeyer et al. 2011), and a phase curve was observed in January 2010, $F_p/F_s=3000\pm200$ ppm (Maxted et al. 2013). These two eclipse depths are consistent to within 1σ and so cannot rule out or confirm variability at 3.6 μm .

Shporer et al. (2019) measure the eclipse depth of WASP-18b with 40 TESS eclipses to be 341^{+17}_{-18} ppm. A $\sim 12\%$ variability in TESS would result in a 21 ppm variability semi-amplitude. The precision on one eclipse measured with TESS would be $18 \times \sqrt{N}$, where N is the number of measurements, resulting in a precision of 113 ppm on each eclipse. Using this precision, we simulate the 40 individual eclipses from Sectors 2 and 3 in Shporer et al. (2019) and the 58 additional unpublished eclipses from Sectors 29 and 30. We then add a 21 ppm sinusoidal variability signal and try to retrieve it using MCMC. We find that TESS does not have the precision to detect the 21 ppm variability to greater than 1σ with the 98 simulated eclipses.

Furthermore, Arcangeli et al. (2018) publish 5 secondary eclipses of WASP-18b with HST/WFC3. Their combined spectrum is measured to ~ 20 ppm precision per bin. Using this, we calculated the precision on the combined white lightcurve to be 38 ppm. This means that the precision on one eclipse is 45 ppm per bin and 86 ppm on the white lightcurve. A $\sim 12\%$ peak-to-trough variability would result in 46–72 ppm semi-amplitudes over the spectral range. Using the same method as above, we found that HST/WFC3 does not have the precision to detect this variability across 5 eclipses in either the white light curve or the individual bins.

4.5 Discussion & Conclusion

We explore the possible origins of the variability in the dayside of an ultra-hot Jupiter atmosphere, these are: changes in disk-integrated temperature, compositional changes, the presence of inhomogeneous clouds, magnetic field interactions or stellar variability.

We first consider whether the periodic change in eclipse depths measured at 4.5 μm could be due to variability of the atmosphere of the planet itself. Variability in the eclipse depths relates directly to variability in the disc averaged brightness temperatures (see Table 4.1). The peak-to-trough change in the brightness temperature of our sinusoidal fit is ~ 250 K. GCMs of WASP-18b show that the temperature pressure profiles on the dayside change significantly from the coolest western terminator to the hottest substellar point Helling et al. (2019). At the millibar level, which corresponds to the pressures probed by Spitzer, these temperatures change by almost 1000 K. 250 K variability in the disc averaged temperature could lead to

compositional variability in the atmosphere in time. However, the dominating opacity at the $4.5\text{ }\mu\text{m}$ band of Spitzer/IRAC is carbon monoxide and the abundance weighted opacity is relatively constant, even over the 1000 K temperature gradient spanned by the hot spot to the western terminator (e.g., Moses et al. 2013). It is therefore unlikely that we are detecting changes in the volume mixing ratio of CO at $4.5\text{ }\mu\text{m}$.

However, high levels of H₂ dissociation are expected in the atmospheres of UHJs, atomic hydrogen can be transported to the nightside via eastward winds where it recombines and deposits a large amount of heat (Komacek 2018; Bell & Cowan 2018). Given a fixed wind speed, this will increase the global efficiency of heat redistribution. However, if the wind speeds are variable, the heat re-circulation from H₂ dissociation/recombination will also vary, and so might the measured brightness.

A second possible cause of variability in the atmosphere of WASP-18b is the presence of clouds. A previous theoretical study has examined cloud formation on WASP-18b using GCMs (Helling et al. 2019). They extract 1D profiles to use as inputs in their kinetic cloud formation modeling. They find that, due to high temperatures, the dayside of WASP-18b has no seed formation and is almost completely cloud-free, with the exception of the coolest mid-latitude western terminator region. However, the seed formation occurs much deeper than the observable pressures. We therefore do not think that in-situ cloud formation is causing the $\sim 12\%$ variability. It is also possible that small cloud particles could be transferred from the nightside to the dayside and act as condensation seeds, however, the dayside temperature is too hot for sufficient supersaturation of the gas phase required for condensation (Helling et al. 2019), thus it is unlikely that the $\sim 12\%$ peak-to-trough brightness variability is due to clouds.

The temperature of WASP-18b dayside is so hot that it is expected that many of the atoms are in their second ionization state (Helling et al. 2019). The predicted degree of ionization ($f_e > 10^{-7}$) is sufficiently high for the atmosphere to couple the planetary magnetic field. This results in electromagnetic hydrodynamic waves called Alfvén waves (Alfvén 1942). MHD GCMs of HAT-P-7b with a 10G magnetic field show zonal wind oscillations on a timescale of $\sim 10^6$ seconds (11.5 days), which is consistent with the Alfvén time ($\tau_A = \sqrt{4\pi\rho\lambda/B}$) (Rogers 2017). Scaling this Alfvén time to the mass and size of WASP-18b, and maintaining a 10G field, leads to a scaling factor of 2.5. This results in ~ 28 day oscillations, which is in good agreement with our measured infrared variability period. The 23 day period of WASP-18b's variability can be matched with a 12G magnetic field injected in this equation. Meaning that our observations can be explained with a relatively small magnetic field. Simulations specific to WASP-18b would be necessary to constrain the magnetic field further.

Stellar variability can alter the interpretation of transiting planets (e.g., Pont et al. 2008; Oshagh et al. 2014; Désert et al. 2011a), however, stellar variability affects transits more than secondary eclipses (Zellem et al. 2017). WASP-18 has been shown to have suppressed stellar activity, with a low $\log(R'_{HK})$ of -5.15 (Lanza 2014) and a far UV spectrum representing that of an old ($>5\text{Gyr}$) inactive star (Fossati et al. 2018). We therefore do not think the brightness variability of WASP-18b is caused by stellar variability. Our finding is similar to HD189733, which is known to be more active than WASP-18. Kilpatrick et al. (2020) measured the

stellar variability amplitudes of HD189733 and find no statistically significant effect on the measured eclipse depths, even though the eclipses have 2x higher precision than WASP-18b.

Multiple epoch observations at different wavelengths would also be necessary to further disentangle the story behind WASP-18b’s variability. However, WASP-18b is the fourth ultra-hot Jupiter to exhibit variability and the first to exhibit periodic infrared brightness variability in time. It is thus clear that planetary variability cannot be ignored going forward with JWST observations of ultra-hot Jupiters. JWST will be able to measure phase curves of ultra-hot Jupiters to unprecedented precision. This will help determine longitudinal changes in chemical composition and measure the brightness phase variations and hot-spot offsets. This, when coupled with MHD atmospheric models, could help constrain the planetary magnetic field strength.

4.A Supplementary plots

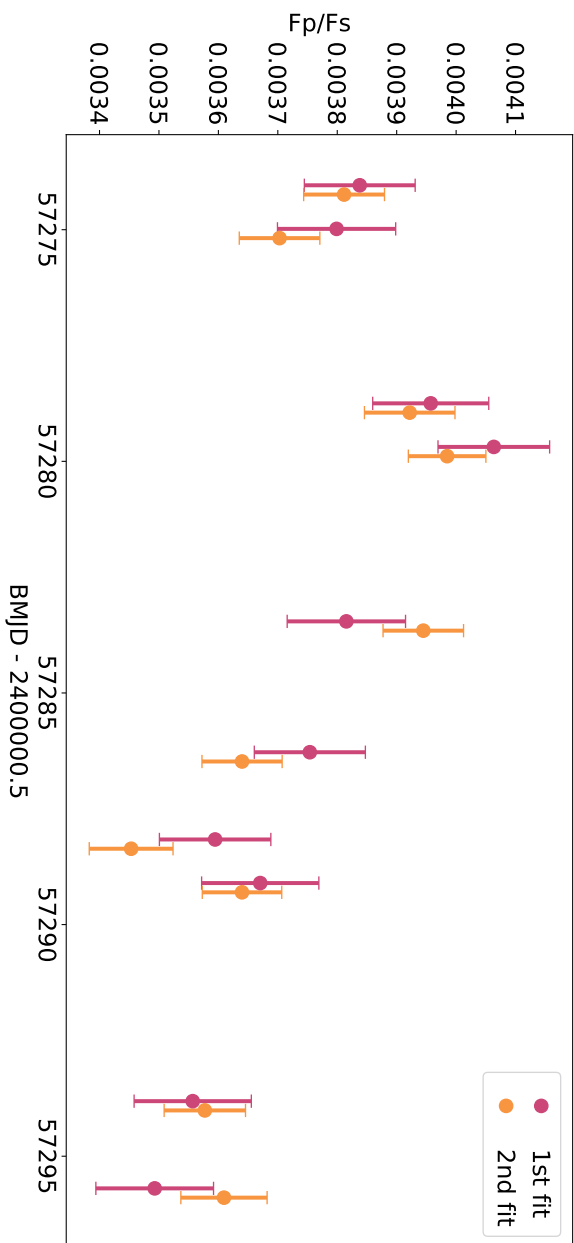


Fig. 4.4: Measured eclipse depths of WASP-18b over time in orange, for the ten semi-consecutive eclipses. Pink shows the eclipse depths from the first fit, where all parameters are free. Orange show the eclipse depths from the second fit, where the orbital distance, inclination and 2 order quadratic term are fixed to the weighted mean from the first fit.

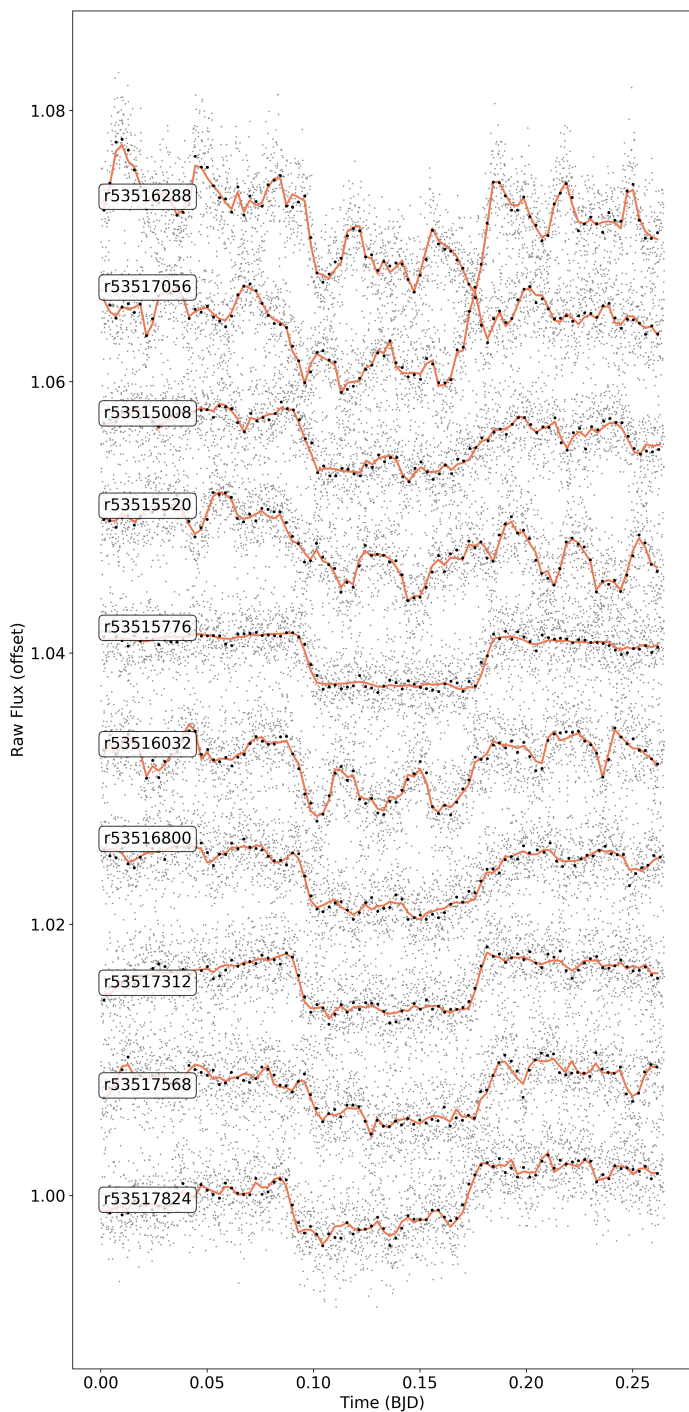


Fig. 4.5: Raw eclipse lightcurves of WASP-18b with best fit systematic and eclipse model in orange.

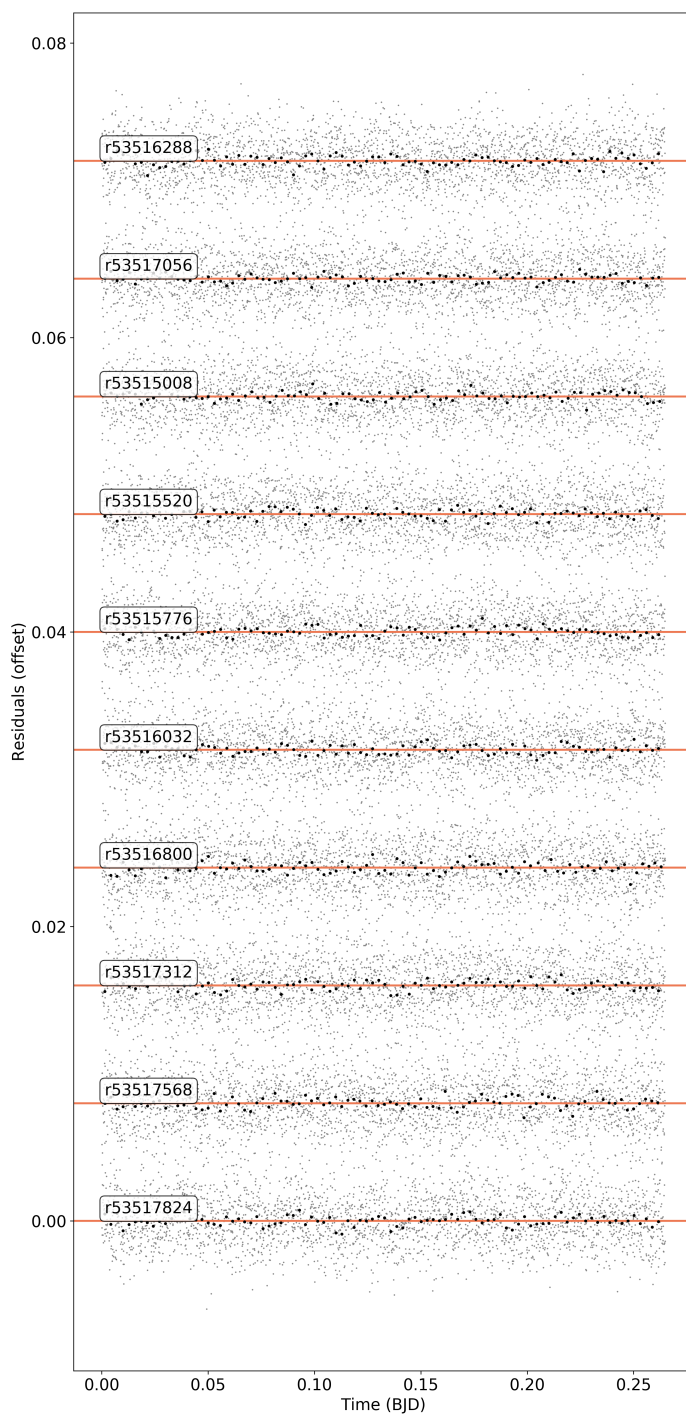


Fig. 4.6: Residuals of WASP-18b eclipses with best fit systematic and eclipse model subtracted.

BIBLIOGRAPHY

- Agol, E., Cowan, N. B., Knutson, H. A., et al. 2010, *ApJ*, 721, 1861
Agúndez, M., Venot, O., Iro, N., et al. 2012, *A&A*, 548, A73
Agúndez, M., Venot, O., Selsis, F., et al. 2014, *ApJ*, 781, 68
Akritas, M. G., & Bershadsky, M. A. 1996, *ApJ*, 470, 706
Alfvén, H. 1942, *Nature*, 150, 405
Allard, F., & Hauschildt, P. H. 1995, *ApJ*, 445, 433
Allard, F., Homeier, D., & Freytag, B. 2011, in Astronomical Society of the Pacific Conference Series, Vol. 448, 16th Cambridge Workshop on Cool Stars, Stellar Systems, and the Sun, ed. C. Johns-Krull, M. K. Browning, & A. A. West, 91
Amundsen, D. S., Tremblin, P., Manners, J., et al. 2017, *A&A*, 598, A97
Anderson, D. R., Smith, A. M. S., Lanotte, A. A., et al. 2011a, *MNRAS*, 416, 2108
Anderson, D. R., Collier Cameron, A., Hellier, C., et al. 2011b, *A&A*, 531, A60
Anderson, D. R., Smith, A. M. S., Madhusudhan, N., et al. 2013, *MNRAS*, 430, 3422
Anderson, D. R., Collier Cameron, A., Delrez, L., et al. 2014, *MNRAS*, 445, 1114
Antuñano, A., Fletcher, L. N., Orton, G. S., et al. 2019, *AJ*, 158, 130
Apai, D., Kasper, M., Skemer, A., et al. 2016, *ApJ*, 820, 40
Arcangeli, J., Désert, J.-M., Line, M. R., et al. 2018, *ApJ*, 855, L30
Arcangeli, J., Désert, J.-M., Parmentier, V., et al. 2019, *A&A*, 625, A136
Armstrong, D. J., de Mooij, E., Barstow, J., et al. 2016, *Nature Astronomy*, 1, 0004
Astropy Collaboration, Price-Whelan, A. M., Sipőcz, B. M., et al. 2018, *AJ*, 156, 123
Bailer-Jones, C. A. L., Rybizki, J., Fouesneau, M., et al. 2018, *AJ*, 156, 58
Bakos, G. Á., Penev, K., Bayliss, D., et al. 2015, *ApJ*, 813, 111
Ballard, S., Charbonneau, D., Deming, D., et al. 2010, *PASP*, 122, 1341
Barros, S. C. C., Pollacco, D. L., Gibson, N. P., et al. 2012, *MNRAS*, 419, 1248
Barstow, J. K., Aigrain, S., Irwin, P. G. J., et al. 2017, *ApJ*, 834, 50
Baskin, N. J., Knutson, H. A., Burrows, A., et al. 2013, *ApJ*, 773, 124
Baxter, C., Désert, J.-M., Parmentier, V., et al. 2020, *A&A*, 639, A36
Beatty, T. G., Marley, M. S., Gaudi, B. S., et al. 2019, *AJ*, 158, 166
Beatty, T. G., Collins, K. A., Fortney, J., et al. 2014, *ApJ*, 783, 112
Beerer, I. M., Knutson, H. A., Burrows, A., et al. 2011, *ApJ*, 727, 23
Bell, T. J., & Cowan, N. B. 2018, *ApJ*, 857, L20
Bell, T. J., Nikolov, N., Cowan, N. B., et al. 2017, *ApJ*, 847, L2

BIBLIOGRAPHY

- Bell, T. J., Zhang, M., Cubillos, P. E., et al. 2019, MNRAS, 489, 1995
- Benneke, B., Knutson, H. A., Lothringer, J., et al. 2019, Nature Astronomy, 3, 813
- Berta, Z. K., Charbonneau, D., Désert, J.-M., et al. 2012, ApJ, 747, 35
- Biddle, L. I., Pearson, K. A., Crossfield, I. J. M., et al. 2014, MNRAS, 443, 1810
- Biller, B. A., Vos, J., Bonavita, M., et al. 2015, ApJ, 813, L23
- Blecic, J., Harrington, J., Madhusudhan, N., et al. 2013, ApJ, 779, 5
- Blecic, J., Harrington, J., Madhusudhan, N., et al. 2014, ApJ, 781, 116
- Bouchy, F., Hebb, L., Skillen, I., et al. 2010, A&A, 519, A98
- Brown, T. M. 2001, ApJ, 553, 1006
- Burke, C. J., McCullough, P. R., Valenti, J. A., et al. 2007, ApJ, 671, 2115
- Burke, C. J., McCullough, P. R., Bergeron, L. E., et al. 2010, ApJ, 719, 1796
- Burrows, A., Hubeny, I., Budaj, J., et al. 2007, ApJ, 661, 502
- Castelli, F., & Kurucz, R. L. 2003, in Modelling of Stellar Atmospheres, ed. N. Piskunov, W. W. Weiss, & D. F. Gray, Vol. 210, A20
- Chachan, Y., Knutson, H. A., Gao, P., et al. 2019, AJ, 158, 244
- Charbonneau, D., Knutson, H. A., Barman, T., et al. 2008, ApJ, 686, 1341
- Charbonneau, D., Allen, L. E., Megeath, S. T., et al. 2005, ApJ, 626, 523
- Christiansen, J. L., Ballard, S., Charbonneau, D., et al. 2010, ApJ, 710, 97
- Collier Cameron, A., Bouchy, F., Hébrard, G., et al. 2007, MNRAS, 375, 951
- Cowan, N. B., & Agol, E. 2011a, ApJ, 726, 82
- Cowan, N. B., & Agol, E. 2011b, ApJ, 729, 54
- Cowan, N. B., Agol, E., & Charbonneau, D. 2007, MNRAS, 379, 641
- Cowan, N. B., Machalek, P., Croll, B., et al. 2012, ApJ, 747, 82
- Crossfield, I. J. M. 2015, PASP, 127, 941
- Cubillos, P., Harrington, J., Madhusudhan, N., et al. 2013, ApJ, 768, 42
- Cutri, R. M., & et al. 2012, VizieR Online Data Catalog, II/311
- Delrez, L., Santerne, A., Almenara, J. M., et al. 2016, MNRAS, 458, 4025
- Deming, D., Seager, S., Richardson, L. J., et al. 2005, Nature, 434, 740
- Deming, D., Knutson, H., Agol, E., et al. 2011, ApJ, 726, 95
- Deming, D., Fraine, J. D., Sada, P. V., et al. 2012, ApJ, 754, 106
- Deming, D., Knutson, H., Kammer, J., et al. 2015, ApJ, 805, 132
- Deming, L. D., & Seager, S. 2017, Journal of Geophysical Research (Planets), 122, 53
- Désert, J.-M., Bean, J., Miller-Ricci Kempton, E., et al. 2011a, ApJ, 731, L40
- Désert, J.-M., Charbonneau, D., Fortney, J. J., et al. 2011b, ApJS, 197, 11
- Désert, J.-M., Charbonneau, D., Demory, B.-O., et al. 2011c, ApJS, 197, 14
- Désert, J. M., Sing, D., Vidal-Madjar, A., et al. 2011d, A&A, 526, A12
- Diamond-Lowe, H., Stevenson, K. B., Bean, J. L., et al. 2014, ApJ, 796, 66
- Doyle, L. R., Carter, J. A., Fabrycky, D. C., et al. 2011, Science, 333, 1602
- Dransfield, G., & Triaud, A. H. M. J. 2020, MNRAS, 499, 505
- Drummond, B., Tremblin, P., Baraffe, I., et al. 2016, A&A, 594, A69
- Dupuy, T. J., & Liu, M. C. 2012, ApJS, 201, 19

- Espinoza, N., Fortney, J. J., Miguel, Y., et al. 2017, *ApJ*, 838, L9
- Esteves, L. J., De Mooij, E. J. W., & Jayawardhana, R. 2015, *ApJ*, 804, 150
- Evans, T. M., Sing, D. K., Kataria, T., et al. 2017, *Nature*, 548, 58
- Faedi, F., Barros, S. C. C., Anderson, D. R., et al. 2011, *A&A*, 531, A40
- Fazio, G. G., Hora, J. L., Allen, L. E., et al. 2004, *ApJS*, 154, 10
- Foreman-Mackey, D., Hogg, D. W., Lang, D., et al. 2013, *PASP*, 125, 306
- Fortney, J. J. 2005, *MNRAS*, 364, 649
- Fortney, J. J., Lodders, K., Marley, M. S., et al. 2008, *ApJ*, 678, 1419
- Fortney, J. J., Mordasini, C., Nettelmann, N., et al. 2013, *ApJ*, 775, 80
- Fortney, J. J., Saumon, D., Marley, M. S., et al. 2006, *ApJ*, 642, 495
- Fortney, J. J., Shabram, M., Showman, A. P., et al. 2010, *ApJ*, 709, 1396
- Fortney, J. J., Visscher, C., Marley, M. S., et al. 2020, *AJ*, 160, 288
- Fortney, J. J., Demory, B.-O., Désert, J.-M., et al. 2011, *ApJS*, 197, 9
- Fossati, L., Koskinen, T., France, K., et al. 2018, *AJ*, 155, 113
- Fraine, J. D., Deming, D., Gillon, M., et al. 2013, *ApJ*, 765, 127
- France, K., Loyd, R. O. P., Youngblood, A., et al. 2016, *ApJ*, 820, 89
- Freedman, R. S., Lustig-Yaeger, J., Fortney, J. J., et al. 2014, *ApJS*, 214, 25
- Freedman, R. S., Marley, M. S., & Lodders, K. 2008, *ApJS*, 174, 504
- Fressin, F., Knutson, H. A., Charbonneau, D., et al. 2010, *ApJ*, 711, 374
- Fu, G., Deming, D., Knutson, H., et al. 2017, *ApJ*, 847, L22
- Gaia Collaboration, Brown, A. G. A., Vallenari, A., et al. 2018, *A&A*, 616, A1
- Gandhi, S., & Madhusudhan, N. 2019, *MNRAS*, 485, 5817
- Gao, P., Thorngren, D. P., Lee, G. K. H., et al. 2020, *Nature Astronomy*, 4, 951
- Garhart, E., Deming, D., Mandell, A., et al. 2020, *AJ*, 159, 137
- Gaudi, B. S., Stassun, K. G., Collins, K. A., et al. 2017, *Nature*, 546, 514
- Gelman, A., & Rubin, D. B. 1992, *Statistical Science*, 7, 457
- Gibson, N. P., Aigrain, S., Roberts, S., et al. 2012, *MNRAS*, 419, 2683
- Guillot, T. 2010, *A&A*, 520, A27
- Guilluy, G., Sozzetti, A., Brogi, M., et al. 2019, *A&A*, 625, A107
- Guo, X., Crossfield, I. J. M., Dragomir, D., et al. 2020, *AJ*, 159, 239
- Han, E., Wang, S. X., Wright, J. T., et al. 2014, *PASP*, 126, 827
- Hansen, B. M. S. 2008, *ApJS*, 179, 484
- Hartman, J. D., Bakos, G. Á., Torres, G., et al. 2009, *ApJ*, 706, 785
- Hartman, J. D., Bakos, G. Á., Sato, B., et al. 2011a, *ApJ*, 726, 52
- Hartman, J. D., Bakos, G. Á., Kipping, D. M., et al. 2011b, *ApJ*, 728, 138
- Hartman, J. D., Bakos, G. Á., Torres, G., et al. 2011c, *ApJ*, 742, 59
- Haynes, K., Mandell, A. M., Madhusudhan, N., et al. 2015, *ApJ*, 806, 146
- Hellier, C., Anderson, D. R., Collier Cameron, A., et al. 2010, *ApJ*, 723, L60
- Hellier, C., Anderson, D. R., Collier Cameron, A., et al. 2012, *MNRAS*, 426, 739
- Hellier, C., Anderson, D. R., Collier Cameron, A., et al. 2017, *MNRAS*, 465, 3693
- Helling, C., Lee, G., Dobbs-Dixon, I., et al. 2016, *MNRAS*, 460, 855

BIBLIOGRAPHY

- Helling, C., Iro, N., Corrales, L., et al. 2019, A&A, 631, A79
- Heng, K., Mendonça, J. M., & Lee, J.-M. 2014, ApJS, 215, 4
- Henry, G. W., & Winn, J. N. 2008, AJ, 135, 68
- Herrero, E., Morales, J. C., Ribas, I., et al. 2011, A&A, 526, L10
- Hoeijmakers, H. J., Ehrenreich, D., Heng, K., et al. 2018, Nature, 560, 453
- Hoeijmakers, H. J., Ehrenreich, D., Kitzmann, D., et al. 2019, A&A, 627, A165
- Hogg, D. W., Bovy, J., & Lang, D. 2010, arXiv e-prints, arXiv:1008.4686
- Holman, M. J., Fabrycky, D. C., Ragozzine, D., et al. 2010, Science, 330, 51
- Hoyer, S., López-Morales, M., Rojo, P., et al. 2013, MNRAS, 434, 46
- Hu, R., Seager, S., & Yung, Y. L. 2015, ApJ, 807, 8
- Hubeny, I. 2017, MNRAS, 469, 841
- Hubeny, I., Burrows, A., & Sudarsky, D. 2003, ApJ, 594, 1011
- Husser, T. O., Wende-von Berg, S., Dreizler, S., et al. 2013, A&A, 553, A6
- Ingalls, J. G., Krick, J. E., Carey, S. J., et al. 2016, AJ, 152, 44
- Jackson, B., Adams, E., Sandidge, W., et al. 2019, AJ, 157, 239
- Johnson, J. A., Gazak, J. Z., Apps, K., et al. 2012, AJ, 143, 111
- Kammer, J. A., Knutson, H. A., Line, M. R., et al. 2015, ApJ, 810, 118
- Kawashima, Y., & Ikoma, M. 2019, ApJ, 877, 109
- Keating, D., Cowan, N. B., & Dang, L. 2019, Nature Astronomy, 3, 1092
- Kelly, B. C. 2007, ApJ, 665, 1489
- Kempton, E. M. R., Bean, J. L., & Parmentier, V. 2017, ApJ, 845, L20
- Kilpatrick, B. M., Kataria, T., Lewis, N. K., et al. 2020, AJ, 159, 51
- Kirkpatrick, J. D., Cushing, M. C., Gelino, C. R., et al. 2011, ApJS, 197, 19
- Kitzmann, D., Heng, K., Rimmer, P. B., et al. 2018, ApJ, 863, 183
- Knutson, H. A., Charbonneau, D., Allen, L. E., et al. 2008, ApJ, 673, 526
- Knutson, H. A., Howard, A. W., & Isaacson, H. 2010, ApJ, 720, 1569
- Knutson, H. A., Charbonneau, D., Allen, L. E., et al. 2007, Nature, 447, 183
- Knutson, H. A., Charbonneau, D., Cowan, N. B., et al. 2009, ApJ, 690, 822
- Knutson, H. A., Madhusudhan, N., Cowan, N. B., et al. 2011, ApJ, 735, 27
- Komacek, T. D. 2018, PhD thesis, The University of Arizona
- Komacek, T. D., Showman, A. P., & Parmentier, V. 2019, ApJ, 881, 152
- Kreidberg, L. 2015, PASP, 127, 1161
- Kreidberg, L., Line, M. R., Thorngren, D., et al. 2018a, ApJ, 858, L6
- Kreidberg, L., Line, M. R., Parmentier, V., et al. 2018b, AJ, 156, 17
- Kurucz, R. L. 1979, ApJS, 40, 1
- Kurucz, R. L., & Bell, B. 1995, Atomic line list
- Lacis, A. A., & Oinas, V. 1991, J. Geophys. Res., 96, 9027
- Lanotte, A. A., Gillon, M., Demory, B. O., et al. 2014, A&A, 572, A73
- Lanza, A. F. 2014, A&A, 572, L6
- Lee, J. M., Fletcher, L. N., & Irwin, P. G. J. 2012, MNRAS, 420, 170
- Leggett, S. K., Tremblin, P., Esplin, T. L., et al. 2017, ApJ, 842, 118

- Lewis, N. K., Knutson, H. A., Showman, A. P., et al. 2013, *ApJ*, 766, 95
- Line, M. R., & Parmentier, V. 2016, *ApJ*, 820, 78
- Line, M. R., Vasish, G., Chen, P., et al. 2011, *ApJ*, 738, 32
- Line, M. R., Wolf, A. S., Zhang, X., et al. 2013, *ApJ*, 775, 137
- Lodders, K., Palme, H., & Gail, H. P. 2009, *Landolt Börnstein*, 4B, 712
- Lothringer, J., & Barman, T. 2019, in American Astronomical Society Meeting Abstracts, Vol. 233, American Astronomical Society Meeting Abstracts #233, 404.05
- Lothringer, J. D., Barman, T., & Koskinen, T. 2018, *ApJ*, 866, 27
- Lyons, L. 1992, *Journal of Physics A Mathematical General*, 25, 1967
- Machalek, P., Greene, T., McCullough, P. R., et al. 2010, *ApJ*, 711, 111
- Machalek, P., McCullough, P. R., Burke, C. J., et al. 2008, *ApJ*, 684, 1427
- Machalek, P., McCullough, P. R., Burrows, A., et al. 2009, *ApJ*, 701, 514
- Maciejewski, G., Ohlert, J., Dimitrov, D., et al. 2014, *Acta Astron.*, 64, 11
- Maciejewski, G., Dimitrov, D., Mancini, L., et al. 2016, *Acta Astron.*, 66, 55
- Madhusudhan, N. 2012, *ApJ*, 758, 36
- Mancini, L., Kemmer, J., Southworth, J., et al. 2016, *MNRAS*, 459, 1393
- Mansfield, M., Bean, J. L., Line, M. R., et al. 2018, *AJ*, 156, 10
- Mansfield, M., Bean, J. L., Stevenson, K. B., et al. 2020, *ApJ*, 888, L15
- Maxted, P. F. L., Anderson, D. R., Doyle, A. P., et al. 2013, *MNRAS*, 428, 2645
- McKay, C. P., Pollack, J. B., & Courtin, R. 1989, *Icarus*, 80, 23
- Melville, G., Kedziora-Chudczer, L., & Bailey, J. 2020, *MNRAS*, 494, 4939
- Metchev, S. A., Heinze, A., Apai, D., et al. 2015, *ApJ*, 799, 154
- Miles, B. E., Skemer, A. J. I., Morley, C. V., et al. 2020, *AJ*, 160, 63
- Molaverdikhani, K., Henning, T., & Molli  re, P. 2019, *ApJ*, 873, 32
- Molaverdikhani, K., Henning, T., & Molli  re, P. 2020, *ApJ*, 899, 53
- Molli  re, P., van Boekel, R., Dullemond, C., et al. 2015, *ApJ*, 813, 47
- Morello, G., Waldmann, I. P., Tinetti, G., et al. 2015, *ApJ*, 802, 117
- Morley, C. V., Fortney, J. J., Marley, M. S., et al. 2015, *ApJ*, 815, 110
- Morley, C. V., Knutson, H., Line, M., et al. 2017, *AJ*, 153, 86
- Moses, J. I., Madhusudhan, N., Visscher, C., et al. 2013, *ApJ*, 763, 25
- Moses, J. I., Visscher, C., Fortney, J. J., et al. 2011, *ApJ*, 737, 15
- Mo  nik, T., Hellier, C., Anderson, D. R., et al. 2017, *MNRAS*, 469, 1622
- Nemmen, R. S., Georganopoulos, M., Guiriec, S., et al. 2012, *Science*, 338, 1445
- Neveu-VanMalle, M., Queloz, D., Anderson, D. R., et al. 2014, *A&A*, 572, A49
- Nikolov, N., Sing, D. K., Pont, F., et al. 2014, *MNRAS*, 437, 46
- Nikolov, N., Sing, D. K., Goyal, J., et al. 2018, *MNRAS*, 474, 1705
- Nymeyer, S., Harrington, J., Hardy, R. A., et al. 2011, *ApJ*, 742, 35
- O'Donovan, F. T., Charbonneau, D., Harrington, J., et al. 2010, *ApJ*, 710, 1551
- O'Rourke, J. G., Knutson, H. A., Zhao, M., et al. 2014, *ApJ*, 781, 109
- Oshagh, M., Santos, N. C., Ehrenreich, D., et al. 2014, *A&A*, 568, A99
- Parmentier, V., & Crossfield, I. J. M. 2018, *Exoplanet Phase Curves: Observations and The-*

BIBLIOGRAPHY

- ory, ed. H. J. Deeg & J. A. Belmonte, 116
- Parmentier, V., Fortney, J. J., Showman, A. P., et al. 2016, *ApJ*, 828, 22
- Parmentier, V., & Guillot, T. 2014, *A&A*, 562, A133
- Parmentier, V., Showman, A. P., & Fortney, J. J. 2021, *MNRAS*, 501, 78
- Parmentier, V., Showman, A. P., & Lian, Y. 2013, *A&A*, 558, A91
- Pearson, K. A. 2019, *AJ*, 158, 243
- Petrucci, R., Jofré, E., Schwartz, M., et al. 2013, *ApJ*, 779, L23
- Pino, L., Désert, J.-M., Brogi, M., et al. 2020, *ApJ*, 894, L27
- Piskorz, D., Buzard, C., Line, M. R., et al. 2018, *AJ*, 156, 133
- Pont, F., Knutson, H., Gilliland, R. L., et al. 2008, *MNRAS*, 385, 109
- Pont, F., Sing, D. K., Gibson, N. P., et al. 2013, *MNRAS*, 432, 2917
- Quijada, M. A., Marx, C. T., Arendt, R. G., et al. 2004, in Society of Photo-Optical Instrumentation Engineers (SPIE) Conference Series, Vol. 5487, Optical, Infrared, and Millimeter Space Telescopes, ed. J. C. Mather, 244
- Reach, W. T., Megeath, S. T., Cohen, M., et al. 2005, *PASP*, 117, 978
- Rogers, T. M. 2017, *Nature Astronomy*, 1, 0131
- Rugheimer, S., Kaltenegger, L., Zsom, A., et al. 2013, *Astrobiology*, 13, 251
- Sainsbury-Martinez, F., Wang, P., Fromang, S., et al. 2019, *A&A*, 632, A114
- Schneider, J., Dedieu, C., Le Sidaner, P., et al. 2011, *A&A*, 532, A79
- Schwartz, J. C., & Cowan, N. B. 2015, *MNRAS*, 449, 4192
- Schwartz, J. C., Kashner, Z., Jovmir, D., et al. 2017, *ApJ*, 850, 154
- Seager, S., & Deming, D. 2010, *ARA&A*, 48, 631
- Seager, S., & Sasselov, D. D. 2000, *ApJ*, 537, 916
- Seeliger, M., Kitze, M., Errmann, R., et al. 2015, *MNRAS*, 451, 4060
- Showman, A. P., & Guillot, T. 2002, *A&A*, 385, 166
- Showman, A. P., & Polvani, L. M. 2011, *ApJ*, 738, 71
- Shporer, A., & Hu, R. 2015, *AJ*, 150, 112
- Shporer, A., O'Rourke, J. G., Knutson, H. A., et al. 2014, *ApJ*, 788, 92
- Shporer, A., Wong, I., Huang, C. X., et al. 2019, *AJ*, 157, 178
- Sing, D. K. 2010, *A&A*, 510, A21
- Sing, D. K., Désert, J. M., Fortney, J. J., et al. 2011, *A&A*, 527, A73
- Sing, D. K., Fortney, J. J., Nikolov, N., et al. 2016, *Nature*, 529, 59
- Skillen, I., Pollacco, D., Collier Cameron, A., et al. 2009, *A&A*, 502, 391
- Smith, A. M. S., Anderson, D. R., Madhusudhan, N., et al. 2012, *A&A*, 545, A93
- Southworth, J. 2008, *MNRAS*, 386, 1644
- Sozzetti, A., Torres, G., Charbonneau, D., et al. 2007, *ApJ*, 664, 1190
- Spake, J. J., Sing, D. K., Evans, T. M., et al. 2018, *Nature*, 557, 68
- Stassun, K. G., Collins, K. A., & Gaudi, B. S. 2017, *AJ*, 153, 136
- Stassun, K. G., Corsaro, E., Pepper, J. A., et al. 2018, *AJ*, 155, 22
- Stassun, K. G., Oelkers, R. J., Paegert, M., et al. 2019, *AJ*, 158, 138
- Steinrueck, M. E., Parmentier, V., Showman, A. P., et al. 2019, *ApJ*, 880, 14

- Stevenson, K., Harrington, J., Nymeyer, S., et al. 2010, in AAS/Division for Planetary Sciences Meeting Abstracts, Vol. 42, AAS/Division for Planetary Sciences Meeting Abstracts #42, 27.13
- Stevenson, K. B., Bean, J. L., Madhusudhan, N., et al. 2014a, *ApJ*, 791, 36
- Stevenson, K. B., Bean, J. L., Seifahrt, A., et al. 2014b, *AJ*, 147, 161
- Stevenson, K. B., Harrington, J., Fortney, J. J., et al. 2012, *ApJ*, 754, 136
- Stevenson, K. B., Désert, J.-M., Line, M. R., et al. 2014c, *Science*, 346, 838
- Swain, M. R., Vasish, G., & Tinetti, G. 2008, *Nature*, 452, 329
- Thao, P. C., Mann, A. W., Johnson, M. C., et al. 2020, *AJ*, 159, 32
- Thorngren, D., Gao, P., & Fortney, J. J. 2019, *ApJ*, 884, L6
- Thorngren, D., Gao, P., & Fortney, J. J. 2020, *ApJ*, 889, L39
- Thorngren, D. P., & Fortney, J. J. 2018, *AJ*, 155, 214
- Thorngren, D. P., Fortney, J. J., Murray-Clay, R. A., et al. 2016, *ApJ*, 831, 64
- Tinetti, G., Deroo, P., Swain, M. R., et al. 2010, *ApJ*, 712, L139
- Todorov, K., Deming, D., Harrington, J., et al. 2010, *ApJ*, 708, 498
- Todorov, K. O., Deming, D., Knutson, H. A., et al. 2012, *ApJ*, 746, 111
- Todorov, K. O., Deming, D., Knutson, H. A., et al. 2013, *ApJ*, 770, 102
- Toon, O. B., McKay, C. P., Ackerman, T. P., et al. 1989, *J. Geophys. Res.*, 94, 16287
- Torres, G., Fressin, F., Batalha, N. M., et al. 2011, *ApJ*, 727, 24
- Tremblin, P., Chabrier, G., Mayne, N. J., et al. 2017, *ApJ*, 841, 30
- Triaud, A. H. M. J. 2014, in American Astronomical Society Meeting Abstracts, Vol. 224, American Astronomical Society Meeting Abstracts #224, 416.02
- Triaud, A. H. M. J., Gillon, M., Ehrenreich, D., et al. 2015, *MNRAS*, 450, 2279
- Tsai, S.-M., Kitzmann, D., Lyons, J. R., et al. 2018, *ApJ*, 862, 31
- Tsai, S.-M., Lyons, J. R., Grosheintz, L., et al. 2017, *ApJS*, 228, 20
- Tsiaras, A., Waldmann, I. P., Zingales, T., et al. 2018, *AJ*, 155, 156
- Venot, O., Agúndez, M., Selsis, F., et al. 2014, *A&A*, 562, A51
- Visscher, C. 2012, *ApJ*, 757, 5
- Visscher, C., Lodders, K., & Fegley, Bruce, J. 2010, *ApJ*, 716, 1060
- Visscher, C., & Moses, J. I. 2011, *ApJ*, 738, 72
- von Essen, C., Mallonn, M., Albrecht, S., et al. 2015, *A&A*, 584, A75
- Wakeford, H. R., Wilson, T. J., Stevenson, K. B., et al. 2019, Research Notes of the American Astronomical Society, 3, 7
- Wakeford, H. R., Sing, D. K., Kataria, T., et al. 2017, *Science*, 356, 628
- Wakeford, H. R., Sing, D. K., Deming, D., et al. 2018, *AJ*, 155, 29
- Wallack, N. L., Knutson, H. A., Morley, C. V., et al. 2019, *AJ*, 158, 217
- Welbanks, L., Madhusudhan, N., Allard, N. F., et al. 2019, *ApJ*, 887, L20
- Werner, M. W., Roellig, T. L., Low, F. J., et al. 2004, *ApJS*, 154, 1
- Wheatley, P. J., Collier Cameron, A., Harrington, J., et al. 2010, arXiv e-prints, arXiv:1004.0836
- Wong, I., Knutson, H. A., Cowan, N. B., et al. 2014, *ApJ*, 794, 134

BIBLIOGRAPHY

- Wong, I., Knutson, H. A., Lewis, N. K., et al. 2015, *ApJ*, 811, 122
Wong, I., Knutson, H. A., Kataria, T., et al. 2016, *ApJ*, 823, 122
Wright, J. T., Fakhouri, O., Marcy, G. W., et al. 2011, *PASP*, 123, 412
Zahnle, K. J., & Marley, M. S. 2014, *ApJ*, 797, 41
Zellem, R. T., Swain, M. R., Roudier, G., et al. 2017, *ApJ*, 844, 27
Zhang, M., Chachan, Y., Kempton, E. M. R., et al. 2019, *PASP*, 131, 034501
Zhang, M., Knutson, H. A., Kataria, T., et al. 2018, *AJ*, 155, 83
Zhang, X., & Showman, A. P. 2018, *ApJ*, 866, 1
Zhao, M., O'Rourke, J. G., Wright, J. T., et al. 2014, *ApJ*, 796, 115
Zilinskas, M., Miguel, Y., Mollière, P., et al. 2020, *MNRAS*, 494, 1490

CONTRIBUTION FROM CO-AUTHORS

Chapter 2: Paper 1

you, your co-authors

Astronomy & Astrophysics, 20XX, YY, ZZZ

(Also referred to as)

OTHER PUBLICATIONS

1. my other publications

NEDERLANDSE SAMENVATTING

Suspendisse vel felis. Ut lorem lorem, interdum eu, tincidunt sit amet, laoreet vitae, arcu. Aenean faucibus pede eu ante. Praesent enim elit, rutrum at, molestie non, nonummy vel, nisl. Ut lectus eros, malesuada sit amet, fermentum eu, sodales cursus, magna. Donec eu purus. Quisque vehicula, urna sed ultricies auctor, pede lorem egestas dui, et convallis elit erat sed nulla. Donec luctus. Curabitur et nunc. Aliquam dolor odio, commodo pretium, ultricies non, pharetra in, velit. Integer arcu est, nonummy in, fermentum faucibus, egestas vel, odio.

ACKNOWLEDGEMENTS

Your Name,
Date

Ph.D. thesis, Anton Pannekoek Institute, Universiteit van Amsterdam
Your Name, Year

ISBN: ■ [TODO: N] ■

Cover design by .

Credits:

afterquote.

Someone

